RESEARCH REPORT

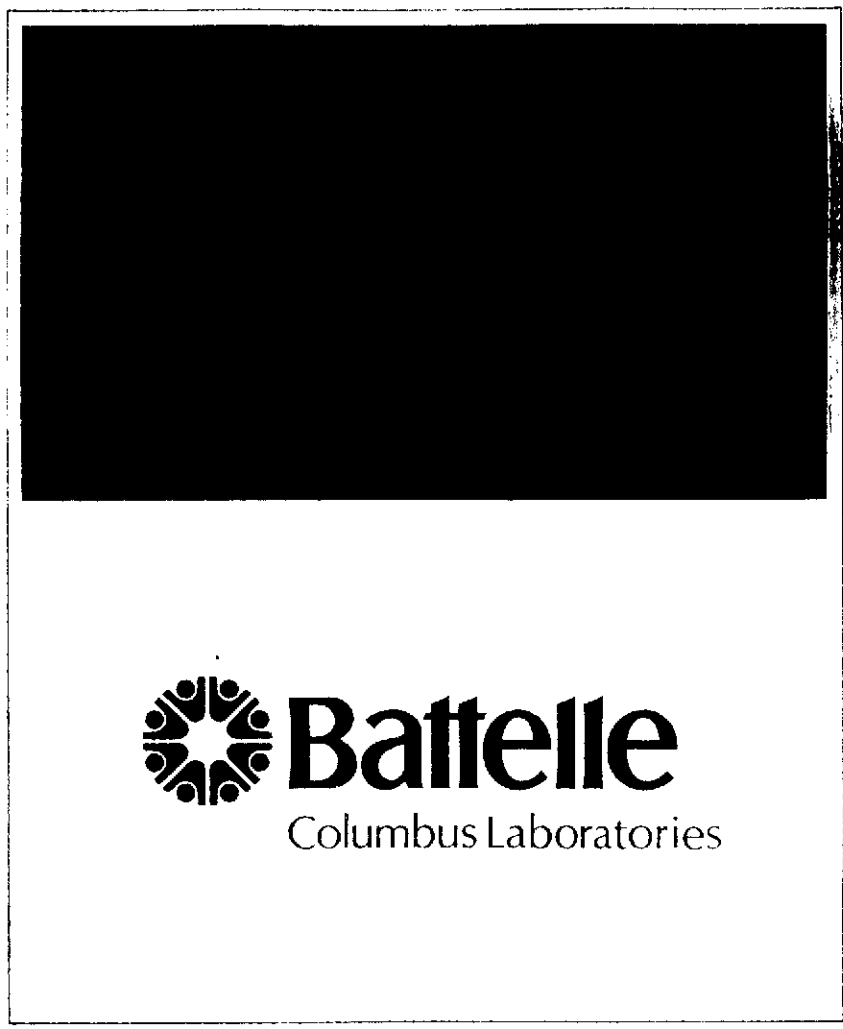

Battelle
Columbus Laboratories

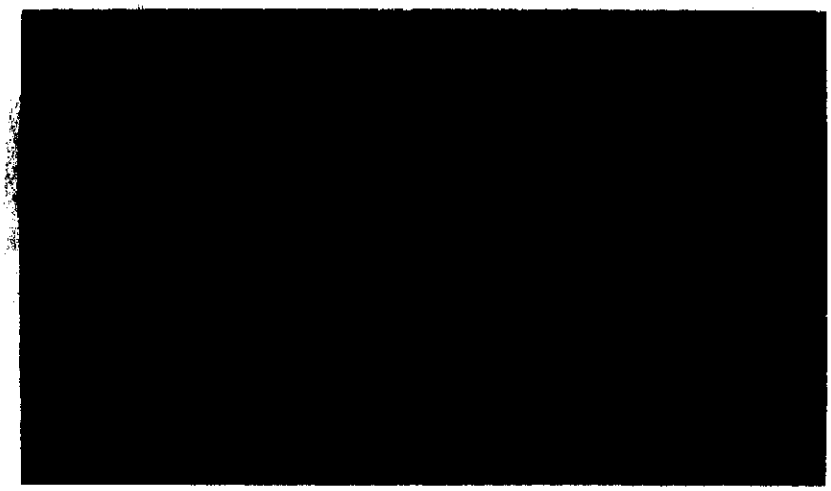

BATTELLE'S COLUMBUS LABORATORIES comprises the original research center of an international organization devoted to research and development.

Battelle is frequently described as a "bridge" between science and industry — a role it has performed in more than 90 countries. It conducts research encompassing virtually all facets of science and its application. It also undertakes programs in fundamental research and education.

Battelle-Columbus — with its staff of 2500 — serves industry and government through contract research. It pursues:

- research embracing the physical and life sciences, engineering, and selected social sciences
- design and development of materials, products, processes, and systems
- information analysis, socioeconomic and technical economic studies, and management planning research.

505 KING AVENUE • COLUMBUS, OHIO 43201

TECHNICAL REPORT

on

BISTATIC RADAR SEA STATE MONITORING

June, 1972

by

George T. Ruck, Donald E. Barrick, and Thaddeus Kaliszewski

The research reported in this document was sponsored by National Aeronautics and Space Administration, Wallops Station, Wallops Island, Virginia, under Contract Number NAS6-2006.

BATTELLE
Columbus Laboratories
505 King Avenue
Columbus, Ohio 43201

FOREWORD

This report covers activities performed by Battelle's Columbus Laboratories (BCL) on behalf of the National Aeronautics and Space Administration, Wallops Station, under Contract No. NAS6-2006, "Services for Oceanography, Geodesy, and Related Areas Task Support". The NASA project monitor was Mr. H. R. Stanley. The Battelle program manager was Mr. A. G. Mourad.

The investigation reported here was one of several tasks under the above mentioned contract and represents the initial phase of a program for developing a sea state monitoring system utilizing a bistatic radar technique.

ABSTRACT

Recent advances in understanding the physical phenomena controlling the interaction of electromagnetic energy with the ocean surface have revealed the possibility of remote measurement of the two-dimensional surface wave height spectrum of the ocean by the use of bistatic radar techniques. Two such techniques have been examined in this study. One operates at HF (3-30 MHz) and the other at UHF ($\approx$ 1 GHz).

Only a preliminary theoretical examination of the UHF technique has been performed and additional work remains before its feasibility can be assessed. The principle underlying the HF technique has been demonstrated experimentally, however, and this study indicates that an HF bistatic system using a surface transmitter (buoy or ship mounted) and an orbital receiver would be capable of measuring the two-dimensional wave height spectrum in the vicinity of the transmitter. In addition such an HF bistatic system could also be used with an airborne receiver for ground truth ocean wave spectrum measurements.

During this study, ionospheric effects on the performance of an orbital HF bistatic sea state sensor were examined and found to limit only the ability of the sensor to measure the higher sea states without significantly reducing its utility.

The use of the Doppler shift imposed on the scattered signal by the satellite motion to obtain the directional properties of the wave height spectrum was also examined and found in general to be feasible.

Preliminary system requirements and hardware configurations are discussed for both an orbital system and an aircraft verification experiment. It appears that the use of a pulse-Doppler system with approximately 10 watts of average power output and range and Doppler resolutions of 3-6 km and 1 Hz, respectively, will be required for an orbital system.

TABLE OF CONTENTS

TABLE OF CONTENTS
(Continued)

LIST OF TABLES

LIST OF FIGURES

LIST OF FIGURES
(Continued)

TECHNICAL REPORT

on

BISTATIC RADAR SEA STATE MONITORING

to

NATIONAL AERONAUTICS AND SPACE ADMINISTRATION
WALLOPS ISLAND, VIRGINIA

from

BATTELLE
Columbus Laboratories

by

George T. Ruck, Donald E. Barrick, and Thaddeus Kaliszewski

June, 1972

I INTRODUCTION

For over a decade the possible use of satellites to measure sea state has been a subject of considerable interest. The measurement of ocean wave heights and direction of travel at several points on the earth can provide valuable data on winds and weather, complementing direct optical and infrared satellite observations.

Various oceanographic techniques are available for measuring the ocean wave height/directional spectrum in a local area, but none are really adaptable to satellite remote sensing. For example, wave spars and buoy-mounted accelerometer/inclinometer measurements can provide crude estimates of directional spectra, but they are expensive and need maintenance; hence, they are generally unsuited to remote sensing in inaccessible ocean areas. Laser profilometers in aircraft have proved successful if several azimuthal paths across an area can be made, but effective measurement of sea state is precluded when they are used in unmanned satellites confined to a single general orbital plane.

Glitter-point aerial photography of the sea surface has proved somewhat successful, but the magnification required to count glitter-points, which are only a few inches apart, from a satellite, and the extremely short exposure time demanded by the satellite velocity, rule it out for orbital applications. Optical signal processing of aerial photographs of the sea, as developed recently by Stillwell, involves the same difficulties as glitter-point photography for orbital

sensing. In addition, the need for high-resolution film for the satellite sensor presents a serious practical objection. Finally, optical techniques for satellite sensing are "fair-weather" techniques; observations can be made only when they are meteorologically least important.

Attention has also been directed toward an orbiting microwave scatterometer/radiometer for sea-state determination. The effectiveness of this device for sea-state monitoring is a subject of considerable question on the basis of both measured data and theoretical analyses. Only by employing quite large antennas and/or complicated synthetic-aperture signal-processing techniques can it be expected that reliable sea-state information could be obtained. Even then, only isotropic surface roughness information can be obtained, with no hope of ascertaining ocean wave direction. Hence, a need exists for development of a technique based on a completely different principle which does not depend upon absolute measurement of the signal level at the receiver.

This suggests the use of radio waves having a length parameter of the same order as the longer ocean waves contributing dominantly to the state of the sea, so as to produce a strong interaction. It has long been known that HF radio waves interact strongly with ocean waves. Significantly, the scatter is due to the Bragg effect, and its intensity depends directly on the heights of the ocean waves responsible for the scatter. By exploiting polarization, motion of the ocean waves, and motion of the satellite, a relative measure of the heights and direction of the dominant ocean waves can be obtained.

A second possible method of sensing the longer ocean waves is the use of two frequencies which are much higher than HF but which are separated by an amount Δf, where Δf lies in the HF region. The cross-correlation function between these two frequencies is dependent upon the slope spectrum of the longer ocean waves evaluated at the Bragg wave number.

The bistatic techniques examined were the use of a direct Bragg scatter mechanism at HF, and a two frequency indirect Bragg scatter mechanism at UHF.

The basic bistatic configuration examined is shown in Figure 1. A low-cost surface-based transmitter located on a buoy or ship is activated by command from a satellite. Radiation transmitted by it illuminates the nearby sea surface and is scattered toward the satellite. Both the direct and the sea-scattered signals are received at the satellite. They are recorded at a convenient IF rate for relay to the ground and subsequent processing.

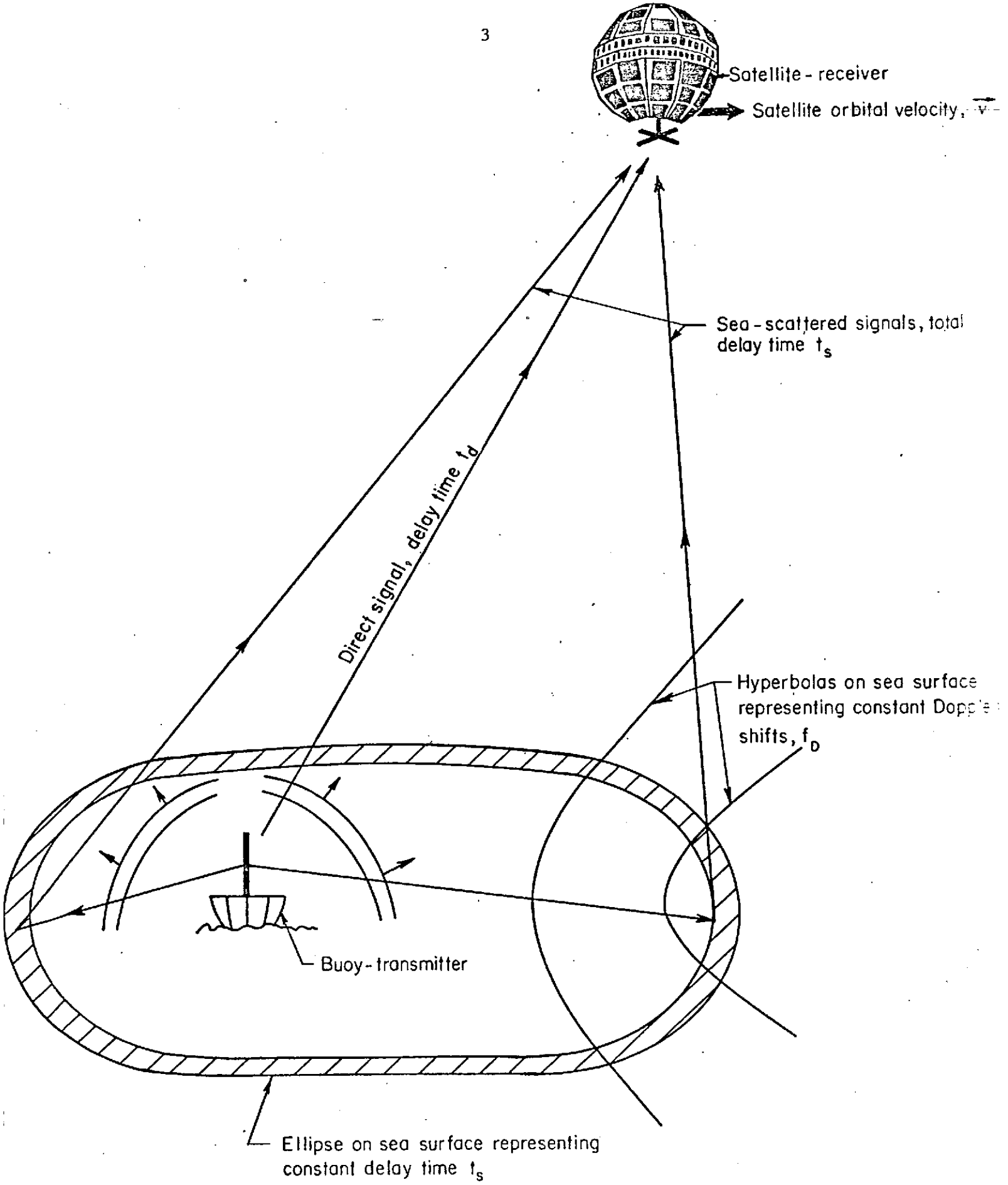

FIGURE 1. BISTATIC SEA STATE MEASUREMENTS

The same basic bistatic configuration would also be suitable for ground truth sea state measurements with the receiver carried on an aircraft rather than a satellite.

The specific approach followed during the course of this study consisted of the following steps:

(1) Analysis of the HF Bragg scatter technique

(2) Examination of techniques for the determination of the directional surface height spectrum using the HF method

(3) Analysis of the UHF Bragg scatter technique

(4) Selection of a specific technique and the determination of preliminary system parameters.

During the course of the examination of the two bistatic approaches discussed above, it became apparent that the HF technique was much closer to fruition. Both theoretical and experimental evidence of the validity of the basic mechanism are available and only the examination of potential problems and hardware limitations need be considered in assessing its feasibility. The two frequency techniques have been assessed only theoretically and no experimental verification of the theory is available as yet. In view of this, the investigation concentrated largely on the HF approach.

During the course of this study, the various radar observables for the HF technique such as signal strengths, signal polarization, signal Doppler spectrum, time delay, etc, have been examined and related to the ocean surface spectrum and the radiated waveform. In addition, various potential problems associated largely with the penetration of HF energy through the ionosphere as required for satellite use of the HF technique have also been examined.

The main results of the study are summarized and recommendations for future work are presented in Section II. In Section III, the theoretical principles of both the HF and UHF approaches are presented. This is followed in Section IV by an analysis of ionospheric effects on a satellite HF bistatic sea state sensor. Section V discusses various systems considerations and parameters associated with the HF technique.

As an outgrowth of our examinations of the interaction between the ocean surface roughness and electromagnetic radiation, the Appendix presents a simplified technique for deriving mean square wave heights from satellite altimetry waveforms.

II SUMMARY OF RESULTS AND RECOMMENDATIONS

Program Summary

The objective of this study has been to examine the application of bistatic Bragg scattering concepts to an ocean wave monitoring system employing simple sea-based transmitters and a satellite receiver. Such a system can be used to measure the directional spatial ocean wave height spectrum near the transmitter. This spectrum is a measure of the heights of the significant ocean waves and the directions in which they are moving. From a knowledge of the wind-wave directional spectrum, the surface wind pattern above the sea can be fairly accurately constructed.

Two specific techniques for measuring the surface height directional spectrum have been examined. One of these operates at HF frequencies (3-30 MHz) and one at UHF ($\approx$ 1 GHz). The study concentrated on the HF technique since it is the most advanced and the underlying physical phenomena have been demonstrated experimentally.

With respect to the HF technique, several problems that may limit its utility have been examined as well as methods for obtaining the directional component of the surface height spectrum. In addition, the hardware requirements have been examined and preliminary configurations identified.

Results

The significant portion of the ocean wave height spectrum is at the lower end which is measured by the lower HF frequencies. These frequencies are those most affected by the ionosphere.

The examination of ionospheric effects on the performance of an HF orbital bistatic sea-state sensor revealed the following:

(1) The operating frequency of the sensor must be confined to the range from 3.5 MHz to 30 MHz.

(2) Propagation conditions favorable to the operation of the system exist generally at night between 0 and 6 hours local time. At such times the minimum ionospheric penetration frequency ranges from 3.5 MHz to 5 MHz depending upon the season and sunspot number.

(4) During normal ionospheric conditions, the absorption loss due to passage through the ionosphere will be less than approximately 15 dB provided the operating frequency exceeds the minimum penetration frequency by at least .5 MHz.

(5) The noise environment encountered by the satellite receiver will be that due to cosmic noise with a maximum effective noise temperature of about $4 * 10^6$ °K at 3 MHz

(6) Ionospherically imposed Doppler shifts can represent a significant error source in determining the directional surface spectrum unless the direct signal component is used as a reference.

(7) Ionospheric induced Faraday rotation will prevent the use of received signal polarization for determining the directional surface height spectrum for an orbital system.

In general, the analysis of ionospheric effects on an HF orbital system indicates that operation at the lower frequencies must be carried out at night. At 3 MHz waves of the order of 100 meters in length are being measured. Waves of this length have build-up time constants of the order of 24 hours, so that measurements at the lower frequencies once a day should be adequate.

Other than the propagation limitations imposed by the ionosphere discussed above, no additional technical problems or limitations on the system have been discovered. Under the assumption that the noise environment encountered by the satellite receiver is due to cosmic noise (discussed in detail in Section IV) adequate signal-to-noise ratios are obtained with average transmitter power output levels of the order of 10 watts for a satellite in a 400 Km orbit.

The directional surface height spectrum can be obtained by the use of coherent Doppler processing and range resolution at the receiver. For a single range cell, Doppler processing results in an angular ambiguity in the directional spectrum. This can be resolved, however, by the use of either several range gates or deconvolution after measurement from several orbital locations on a specific satellite pass. This is discussed in detail in Section V.

The hardware requirements appear to be relatively modest with the most straightforward approach being the use of a pulse Doppler type transmitter-receiver combination using 10-20 μsec pulse widths and approximately a 1 sec coherent integration time. More sophisticated approaches might be the use of phase-coded or FMCW waveforms to achieve both range and Doppler resolution. The antennas can be simple, such as a vertical whip for transmitting, or if desired the use of a transmitting antenna with some directivity would aid in resolving the directional ambiguities.

Recommendations

In view of the favorable results of the present study it is recommended that a Phase II effort be undertaken. During Phase II the following specific activities should be carried out:

(1) A field test experiment of the HF technique using an aircraft as a receiving platform should be designed.

(2) The hardware configuration for the field experiment should be determined and the necessary hardware procured and modified as required.

Design specifications for the experimental hardware should be drawn up during this phase, the test hardware assembled, and procedures for a field experiment developed. For the subsequent experiment it is anticipated that the receiver will be flown in an aircraft with the transmitter on a ship. Independent sea-state measurements in the area of interest will be required using wave spars or a laser profilometer, etc. for verification of the bistatic measurements.

The hardware configuration used for the field test experiment should be as close as practicable to that required for a satellite system. For example, Doppler processing to obtain the surface spectrum directionality should be tested if possible.

The second phase should be followed by a third phase in which the aircraft field experiment is carried out, the experimental data reduced and analyzed, and recommendations made for both satellite hardware design and design of the hardware for an airborne ground truth measurement system.

In addition, a low level of effort continuation of the analysis of the UHF approach should be carried out if possible. Even though this approach has been examined only theoretically to date it could be quite valuable if it should prove to be feasible.

III THEORETICAL PRINCIPLES

HF Scattering from the Ocean Surface

At the radio wavelengths characteristic of the HF region (10 to 100 meters) the ocean surface corresponds to slightly rough surface, and the boundary perturbation technique of Rice[1]* can be used to determine the incoherent energy scattered from an HF ground wave propagating across this surface. The results of applying Rice's technique to a slightly rough dielectric surface are presented by Barrick and Peake[2]. These results are for plane wave incidence with arbitrary polarization and arbitrary angles of incidence and scattering. The scattering geometry being considered here is illustrated in Figure 2. It is assumed for the present discussion that the incident field is propagating parallel to the average direction in which the winds are blowing over the surface area of interest. For a plane wave incident at a polar angle θ_i with radian frequency ω_o and wave number k_o, the scattering cross section per unit surface area is

$$\sigma^o_{ij}(\theta_s,\varphi_s,\theta_i) = 4\pi k_o^4 \cos^2\theta_i \cos^2\theta_s |\alpha_{ij}|^2 \{w^- \delta(\omega - \omega_o + \omega_g) + w^+ \delta(\omega - \omega_o - \omega_g)\} \quad , \quad (1)$$

with

$$w^- = w[k_o(\sin\theta_s \cos\varphi_s - \sin\theta_i),\ k_o(\sin\theta_s \sin\varphi_s)]$$

$$w^+ = w[-k_o(\sin\theta_s \cos\varphi_s - \sin\theta_i),\ -k_o(\sin\theta_s \sin\varphi_s)]$$

$$\omega_g = \sqrt{gk_o}[(\sin\theta_s \cos\varphi_s - \sin\theta_i)^2 + (\sin\theta_s \sin\varphi_s)^2]^{1/4} \quad (2)$$

In this equation the parameters α_{ij} are complex scattering matrix elements which are functions of the incident and scattering angles, the incident and scattered field polarizations, and the surface dielectric properties. The function $w(k_x,k_y)$ is the two dimensional surface energy or wave height spectrum and will be discussed in more detail later. The parameter g is the acceleration due to gravity, nominally 9.81 meters/s^2. For the incident and scattered fields either vertically or horizontally polarized, the scattering matrix elements α_{ij} for the ocean surface become

---

* References are given on page 95.

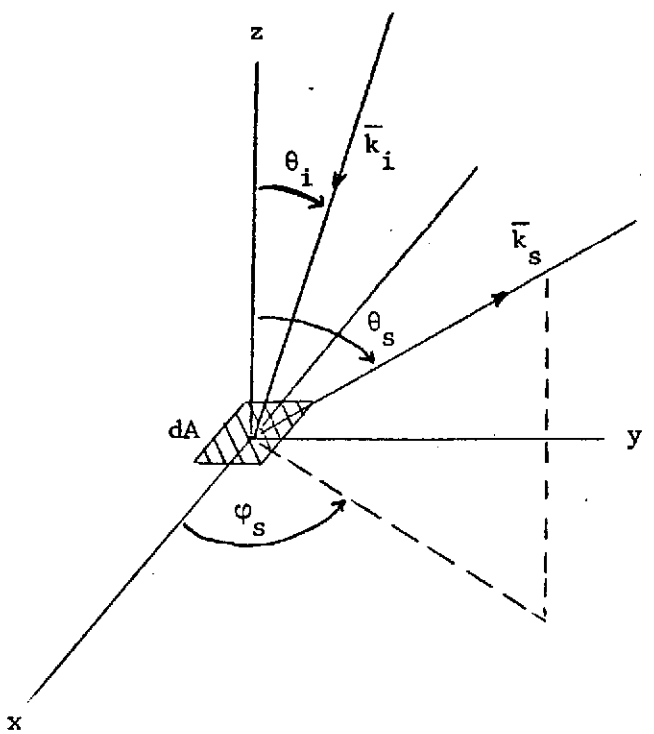

FIGURE 2. SCATTERING GEOMETRY

$$\alpha_{hh} = \frac{(\epsilon_r - 1)\cos\varphi_s}{(\cos\varphi_i + \sqrt{\epsilon_r - \sin^2\theta_i})(\cos\theta_s + \sqrt{\epsilon_r - \sin^2\theta_s})}$$

$$\alpha_{hv} = \frac{(\epsilon_r - 1)\sin\varphi_s \sqrt{\epsilon_r - \sin^2\theta_s}}{(\epsilon_r \cos\theta_i + \sqrt{\epsilon_r - \sin^2\theta_i})(\cos\theta_s + \sqrt{\epsilon_r - \sin^2\theta_s})}$$

$$\alpha_{vh} = \frac{-\sin\varphi_s(\epsilon_r - 1)\sqrt{\epsilon_r - \sin^2\theta_s}}{(\cos\theta_i + \sqrt{\epsilon_r - \sin^2\theta_i})(\epsilon_r \cos\theta_s + \sqrt{\epsilon_r - \sin^2\theta_s})}$$

$$\alpha_{vv} = \frac{(\epsilon_r - 1)(\epsilon_r \sin\theta_i \sin\theta_s - \cos\varphi_s \sqrt{\epsilon_r - \sin^2\theta_i}\sqrt{\epsilon_r - \sin^2\theta_s})}{(\epsilon_r \cos\theta_i + \sqrt{\epsilon_r - \sin^2\theta_i})(\epsilon_r \cos\theta_s + \sqrt{\epsilon_r - \sin^2\theta_s})} \quad . \tag{3}$$

In these expressions ϵ_r is the relative dielectric constant of sea water at HF frequencies. This is approximately 80 + i 7200 at 10 MHz and is given in general by

$$\epsilon_r \approx 80 + i\,\frac{\sigma}{\epsilon_o \omega_o} \quad , \tag{4}$$

with σ the electrical conductivity of sea water, ϵ_o the permittivity of free space ($10^{-9}/36\pi$ in MKS units), and ω_o the incident radian frequency.

The subscript notation used for the scattering matrix element has the following interpretation: the first subscript denotes the polarization of the scattered field with v corresponding to the electric field polarized along $\hat{\theta}_s$ and h corresponding to the electric field polarized along $\hat{\varphi}_s$; the second subscript describes the incident field polarization and v corresponds to the electric field vector lying in the $\hat{\theta}_i$ direction with h denoting the electric field lying in the $\hat{\varphi}_i$ direction. For the coordinates of Figure 2, the $\hat{\varphi}_i$ direction is along -y.

It is of interest to examine the form the scattering matrix elements take for a perfectly conducting surface. These can be obtained from Equations 3 by taking the limiting case of $\epsilon_r \to \infty$. If this is done, then

$$\alpha_{hh}\Big|_{p.c.} = -\cos\varphi_s \quad ,$$

$$\alpha_{hv}\Big|_{p.c.} = \frac{\sin \varphi_s}{\cos \theta_i} \quad ,$$

$$\alpha_{vh}\Big|_{p.c.} = -\frac{\sin \varphi_s}{\cos \theta_s} \quad ,$$

$$\alpha_{vv}\Big|_{p.c.} = \frac{\sin \theta_i \sin \theta_s - \cos \varphi_s}{\cos \theta_i \cos \theta_s} \quad . \tag{5}$$

These are obviously much simpler than the previous equations and are very useful in understanding the physical basis of electromagnetic scattering from the ocean surface.

Returning to Equation (1), we note that although the incident field has a frequency ω_o, the scattered field contains two frequency components one at $\omega_o + \omega_g$ and one at $\omega_o - \omega_g$ with the amplitude of these given by w^+ and w^- respectively. Relating these to the surface structure is somewhat easier if the two dimensional surface spectrum $w(k_x,k_y)$ is transformed slightly. A definition of $w(k_x,k_y)$ which is adequate for the present discussion is given by

$$\overline{\zeta}^2 = \int_{-\infty}^{\infty}\int_{-\infty}^{\infty} w(k_x,k_y)dk_x dk_y \tag{6}$$

with $\overline{\zeta}^2$ the mean-square ocean wave height. If a coordinate transformation from k_x, k_y to the polar coordinates k,ψ is applied with

$$k_x = k \cos \psi \quad , \quad \text{and} \quad k_y = k \sin \psi \tag{7}$$

then

$$\overline{\zeta}^2 = \int_0^{\infty}\int_0^{2\pi} w(k,\psi)kdkd\psi \quad . \tag{8}$$

An expression identical to Equation (1) for the scattering cross section per unit area can be written utilizing $w(k,\psi)$. It must be kept in mind however that the total scattered power from a finite surface area is the integral of $\sigma^o dA$ and dA in this case is expressed in polar coordinates. The parameter k is given by

$$k = \sqrt{k_x^2 + k_y^2} = k_o(\sin^2 \theta_s + \sin^2 \theta_i - 2 \sin \theta_i \sin \theta_s \cos \varphi_s)^{1/2} \quad (9)$$

with

$$\psi = \tan^{-1}\left(\frac{\sin \theta_s \sin \varphi_s}{\sin \theta_s \cos \varphi_s - \sin \theta_i}\right) \quad . \quad (10)$$

To simplify the discussion, we will assume grazing incidence and scattering, thus setting θ_i, θ_s to $\pi/2$ and

$$k = k_o(2 - 2 \cos \varphi_s)^{1/2} \quad , \quad (11)$$

$$\psi = \tan^{-1}\left(\frac{\sin \varphi_s}{\cos \varphi_s - 1}\right) \quad . \quad (12)$$

Examining these we see that the scattered field intensity is proportional to the wave spectral strength at the wavenumber k. For scattering in the forward direction $k = 0$ and the cross section is proportional to the DC component of the spectrum which as discussed later is zero. For bistatic scatter with $\varphi_s = \pm \pi/2$, the cross section is proportional to the surface spectral components with wavenumber equal to $\sqrt{2}/k_o$ which are propagating with crests oriented at an angle of 45° with respect to the x-axis. For backscatter, only those ocean waves with spatial wavelength equal to one-half the incident wavelength and whose crests are oriented perpendicular to the incident field direction contribute to the scattering. Thus, depending upon the angular orientation of the incident and scattered fields only those components of the ocean wave structure having wavelengths greater than the incident wavelength can contribute to the scattered power.

Physically, to first order in the perturbation analysis, the interaction between an incident electromagnetic field and the ocean surface structure is such that the ocean surface acts like a diffraction grating with only those wave components having a spatial periodicity and orientation corresponding to the so-called Bragg scattering conditions contributing to the scattered field.

In addition to the scattered intensity being proportional to the spectral density of ocean waves of a specific wavelength, the frequency shifts imposed on the scattered field are Doppler shifts corresponding to the propagation velocity of gravity waves of this wavelength.

Thus, if one were to illuminate the ocean surface near grazing incidence and observe the backscattered power, only those waves having wavelengths of one-half the incident wavelength would contribute to scattering, and two spectral components separated from the carrier by frequencies of $\pm(1/\pi)\sqrt{gk_o/2}$ would be observed. The relative strengths of these two components would be determined by the relative spectral densities of ocean waves of 1/2 the incident wavelength moving away from the transmitter and toward the transmitter.

If the scattering matrix elements given by Equation (3) are examined in conjunction with Equation (1), it appears that for a dielectric surface such as the ocean, the $\cos^2 \theta_i$ factor in Equation (1) results in the scattering cross section going to zero at grazing incidence for both horizontal and vertical polarization. This appears to be contrary to experimental evidence where the horizontal polarization cross section appears to approach zero as the incident angle goes to grazing; however, the vertical polarization cross section appears to be nearly constant for angles near grazing and equals the values predicted for a perfectly conducting surface. Thus, experimental measurements indicate that at HF for grazing and near grazing angles, the ocean scatters as if it were a perfectly conducting rough surface.

The deviation between the experimentally observed cross sections and those predicted by Equation (1) is due to the use of an assumed plane wave incident field in the derivation of Equation (1). For an HF transmitting antenna located on the earth's surface, the field on the surface at a short distance from the antenna is not a plane wave but a type of surface wave commonly called the ground wave. The ground wave field is not vertically polarized but propagates with a slight tilt into the earth's surface. The effect of this wave tilt is equivalent to a plane wave incident at an angle slightly above grazing, thus the scattered field is not zero for an incident ground wave. At frequencies of 3-30 MHz over sea water the wave tilt is of the order of .25 to .5°. At angles of this order above grazing, the vertically polarized scattering cross sections of the actual ocean surface differ insignificantly from those for a perfectly conducting surface with the same geometrical properties.

Thus, the perfectly conducting scattering matrix parameters given in Equation (5) are applicable for the ocean surface for an incident ground wave with $\theta_i = \pi/2$. This allows the polarization dependence of the scattering to be easily examined. For a vertically polarized ground wave only α_{vv} and α_{hv} are of

interest. Using these gives the following scattering cross sections

$$\sigma_{vv}(\theta_s,\varphi_s, \tfrac{\pi}{2}) = 2\pi k_o^4(\sin\theta_s - \cos\varphi_s)^2\{w^-\delta(-) + w^+\delta(+)\} \quad , \tag{13}$$

and

$$\sigma_{hv}(\theta_s,\varphi_s, \tfrac{\pi}{2}) = 2\pi k_o^4 \cos^2\theta_s \sin^2\varphi_s\{w^-\delta(-) + w^+\delta(+)\} \quad . \tag{14}$$

Examining these for θ_s near zero which is the bistatic geometry of interest for an orbital or airborne sensor, it is apparent that σ_{vv} is maximum for $\varphi_s = 0,\pi$ and small for $\varphi_s = \pm\pi/2$. Thus the scattered field polarization is nearly horizontal and parallel to the incident field direction. Similarly σ_{hv} is maximum for $\varphi_s = \pm\pi/2$ and zero for $\varphi_s = 0,\pi$, however in both cases the field is polarized dominantly in the horizontal plane.

The Ocean Surface Spectrum

The most useful existing model of the sea surface and the one providing the most agreement with the available experimental evidence is the representation of the surface height as a function of position and time as a random process in which the surface height is given by

$$\zeta(x,y,t) = \sum_{n=0}^{\infty} c_n \cos(u_n x + v_n y + \sigma_n t + \epsilon_n) \quad , \tag{15}$$

where the wave numbers (u_n,v_n) are densely distributed throughout the u,v plane. The frequency parameter σ_n is in general a function of u_n, v_n. The amplitudes c_n are random variables and in any element dudv

$$\sum_n \frac{1}{2} c_n^2 = w(u,v)\ dudv \quad . \tag{16}$$

The phases ϵ_n are distributed randomly and with equal probability in the interval $(0,2\pi)$. The mean-square value of ζ per unit area of surface per unit time is

$$\overline{\zeta^2} = \lim_{x,y,t \to \infty} \frac{1}{8xyt} \int_{-x}^{x} \int_{-y}^{y} \int_{-t}^{t} \zeta^2 \, dxdydt = \sum_n \frac{1}{2} c_n^2 = \int_{-\infty}^{\infty} \int_{-\infty}^{\infty} w(u,v) dudv \quad . \quad (17)$$

The function w(u,v) is called the energy spectrum of ζ and the contribution to the mean energy from an element dudv is proportional to wdudv.

A knowledge of w(u,v) is in general all that is required in order to determine the average properties of the surface, i.e., mean-square height, average surface slopes, etc. For our purposes is also necessary to know the dispersion relation for the surface, that is, the relation between the phase velocity of a particular wave and its wave number. Designating the wave number by k as usual, where $k = 2\pi/\lambda$ the phase velocity for small amplitude gravity waves is given by

$$v^2 = \left(\frac{g}{k}\right) \tanh kh \quad (18)$$

with h the water depth. For deep water tanh kh approaches one, thus $v^2 = g/k$. This has been used in the derivation of the Doppler shift of the scattered field due to the ocean wave motion as given by ω_g of Equation (2).

Very little specific information is available with respect to the full two-dimensional surface energy spectrum of the ocean and its relationship to the wind velocity, duration, and fetch. A number of models have been developed for the non-directional spectrum. The non-directional spectrum can be obtained by integrating w(u,v) over all directions and this is most easily carried out in polar coordinates. If a coordinate transformation from the u,v plane to the k,ψ plane is made then

$$\overline{\zeta^2} = \int_0^{\infty} \int_0^{2\pi} w(k,\psi) \, kdkd\psi \quad . \quad (19)$$

If s(k) is defined as the non-directional spectrum, then

$$s(k) = \int_0^{2\pi} w(k,\psi) \, d\psi \quad , \quad (20)$$

and

$$\overline{\zeta^2} = \int_0^{\infty} s(k) \, kdk \quad . \quad (21)$$

The non-directional spectrum s(k) can be estimated from measurements taken with wave staffs or other instrumentation. In addition, theoretical models for s(k) have been developed. The first model to gain wide attention was that developed by Neumann where

$$s(k) \approx c\ k^{-9/2}\ \exp\left(\frac{-2g}{kV^2}\right) \tag{22}$$

with V the wind velocity, and c an empirically determined constant. Subsequently several workers[3] pointed out that for large wave numbers, theoretical considerations indicate that the spectrum must be proportional to k^{-4} rather than $k^{-9/2}$ as indicated by the Neumann spectrum. Phillips[4] indicates that in the equilibrium range where winds of sufficient duration and fetch are present the spectrum must have the form

$$s(k) = Ak^{-4} \quad . \tag{23}$$

In addition, his theory predicts that waves with wave numbers smaller than g/V^2 can not be present in a wind driven sea. Any wave structures with smaller wave numbers must have propagated into the region from other areas. This is generally classified as swell in contrast to the wind sea generated by local winds.

Since it is somewhat unrealistic to expect the surface spectrum to have an infinitely sharp cutoff at $k = g/V^2$, several spectrum models with exponential cutoff have been used. One of these combines the Phillips type of equilibrium behavior with Neumann's exponential cutoff. This spectrum, designated here as the Neumann-Pierson, is given by

$$s(k) = 2Ak^{-4}\ \exp\left(\frac{-2g}{kV^2}\right) \quad . \tag{24}$$

Another such spectrum, designated here as the Pierson-Moskowitz has a somewhat sharper exponential cutoff. This has the form

$$s(k) = .74Ak^{-4}\ \exp\left(\frac{-.74g^2}{k^2V^4}\right) \quad . \tag{25}$$

Returning to the two-dimensional spectrum $w(k,\psi)$, it is often assumed that this is isotropic. In this case

$$w(k,\psi) = \frac{s(k)}{2\pi} \quad . \tag{26}$$

Another assumption often used is that $w(k,\psi)$ is non-zero only in the sector $\pm 90°$ around the mean wind direction. Within this sector, it is usually assumed to be either isotropic or have a $\cos^2 \psi$ directionality. There is little theoretical or experimental support for any one of these assumptions however. If $w(k,\psi)$ is assumed isotropic from $-\pi/2$ to $\pi/2$ then

$$w(k,t) = \frac{s(k)}{\pi} \quad , \tag{27}$$

and if a $\cos^2$ directionality is assumed then

$$w(k,\psi) = \frac{2}{\pi} s(k) \quad . \tag{28}$$

Based on a number of measurements, an appropriate value of A appears to be of the order of .005. Although various values for the constant A appear in the literature, most are of the same order of magnitude and in fact Longuet-Higgins[5] has demonstrated from fundamental principles that A must be of the same order of magnitude as .005. It should be noted that as given by Equations (23), (24), and (25) the various spectrum models are normalized so that for a given wind velocity V, the same RMS surface heights are obtained from all three spectral models. The true relationship between the RMS surface height and the wind velocity has, of course, not been established as yet.

Surface Spectrum Measurements Using HF Scattering

The scattering cross section at HF as given by Equation (1) can be seen to depend directly upon the two-dimensional surface energy spectrum $w(u,v)$ or equivalently $w(k,\psi)$. To simplify the discussion, the case where $\theta_i = \pi/2$, $\theta_s = 0$ will be examined for vertical polarization and the perfectly conducting scattering matrix coefficient will be used. This is valid as discussed previously. Under these conditions

$$\sigma_{vv} \approx 4\pi k_0^4 \cos^2 \varphi \left\{ w^- \delta(-) + w^+ \delta(+) \right\} \quad , \tag{29}$$

and

$$w^- \approx w(-k_o,0) \quad , \quad w^+ \approx w(k_o,0) \quad . \tag{30}$$

Assuming for the moment that the spectrum is isotropic and using the Phillip's spectrum, then

$$w(k,\psi) = \frac{A}{2\pi} k^{-4} \tag{31}$$

using Equations (23) and (26). The corresponding value of w(u,v) is

$$w(u,v) = \frac{4A}{(u^2 + v^2)^2 \pi} \tag{32}$$

Using this, then $w^-(-k_o,0) = w^+(k_o,0) = (4A/\pi)\, k_o^{-4}$, and

$$\sigma_{vv} \approx 16A \cos^2 \varphi \tag{33}$$

for values of $k > g/V^2$. This relationship indicates that the bistatic cross section for $\varphi_s = 0,\pi$ is essentially constant for frequencies greater than $cg/2\pi V^2$ and responds only to the spectral strength of those waves moving parallel to the incident field direction.

Thus an obvious way to measure the surface spectrum is to illuminate the surface at a number of HF frequencies and determine the resulting scattering cross section. If this is done, then the observed scattering cross section will be a direct measure of the surface spectrum. The entire two-dimensional spectrum can be obtained if the surface is illuminated at various incidence angles relative to the mean wind direction. This is automatically accomplished if an omnidirectional transmitting antenna is used.

Considering then, an azimuthally omnidirectional transmitting antenna illuminating a region around the transmitter. At a particular near zenith observing location, the scattered energy received, corresponding to a specific transmitted frequency, is proportional to the spectral intensity of those ocean waves propagating in a radial direction between the transmitter and a particular scattering region and whose wavelength is equal to the transmitted wavelength. Thus if the directionality of the spectrum is to be measured some means for distinguishing the angular location of a scattering region relative to the direction of travel of the ocean waves is necessary.

The only received signal parameters which can be directly related to the scattering geometry and wave direction are the polarization and Doppler shift. For a satellite-borne receiver orbiting in or above the ionosphere (above approximately 200 km) the ionospheric Faraday rotation precludes the use of signal polarization at HF frequencies. This is discussed in more detail in Section IV.

Thus, the signal Doppler must be utilized to obtain the directional spectrum with a satellite system. In order to do this, some form of range resolution must also be provided in order that specific surface areas surrounding the transmitter can be delineated. The use of the received Doppler for determining the directional spectrum will be examined in detail in Section V.

Returning to the measure of the non-directional or integrated spectrum, Equation (29) indicates that the bistatic cross section is proportional to the surface spectrum multiplied by k_o^4 and $\cos^2 \varphi$. Considering a receiver located vertically or nearly vertically above the transmitter, the differential received signal strength per unit surface area is proportional to the scattering cross section multiplied by a factor which includes the antenna gains, ranges, transmitter power output, etc. as given below

$$dP_r = \left\{ \frac{P_t G_t G_r \lambda_o^2 L}{(4\pi)^3 \rho^2 r^2} \, dA \right\} \sigma^o = dK\sigma^o \quad . \tag{34}$$

In this equation G_r is the receiving antenna gain, G_t is the transmitting antenna gain, P_t the transmitter power output, ρ the distance from the transmitter to the scattering area dA on the surface, r the distance from the scattering area to the receiver, λ_o the transmitting wavelength, and L accounts for various loss factors such as ground wave attenuation, ionospheric attenuation, etc. This equation is for the CW case where both P_r and P_t are average powers. If the multiplying factor dK is known as a function of frequency, and this will be the case if the direct signal is available as a reference, then the received power normalized by dK is proportional to σ^o.

To illustrate the manner in which this varies with the surface properties, curves of σ^o versus transmitted frequency have been calculated for two different surface spectrum models and several wind velocities. The spectral models used are the Pierson-Moskowitz and the Neumann-Pierson. These curves are illustrated in Figures 3 through 10. The ordinate in these Figures is given in dB.

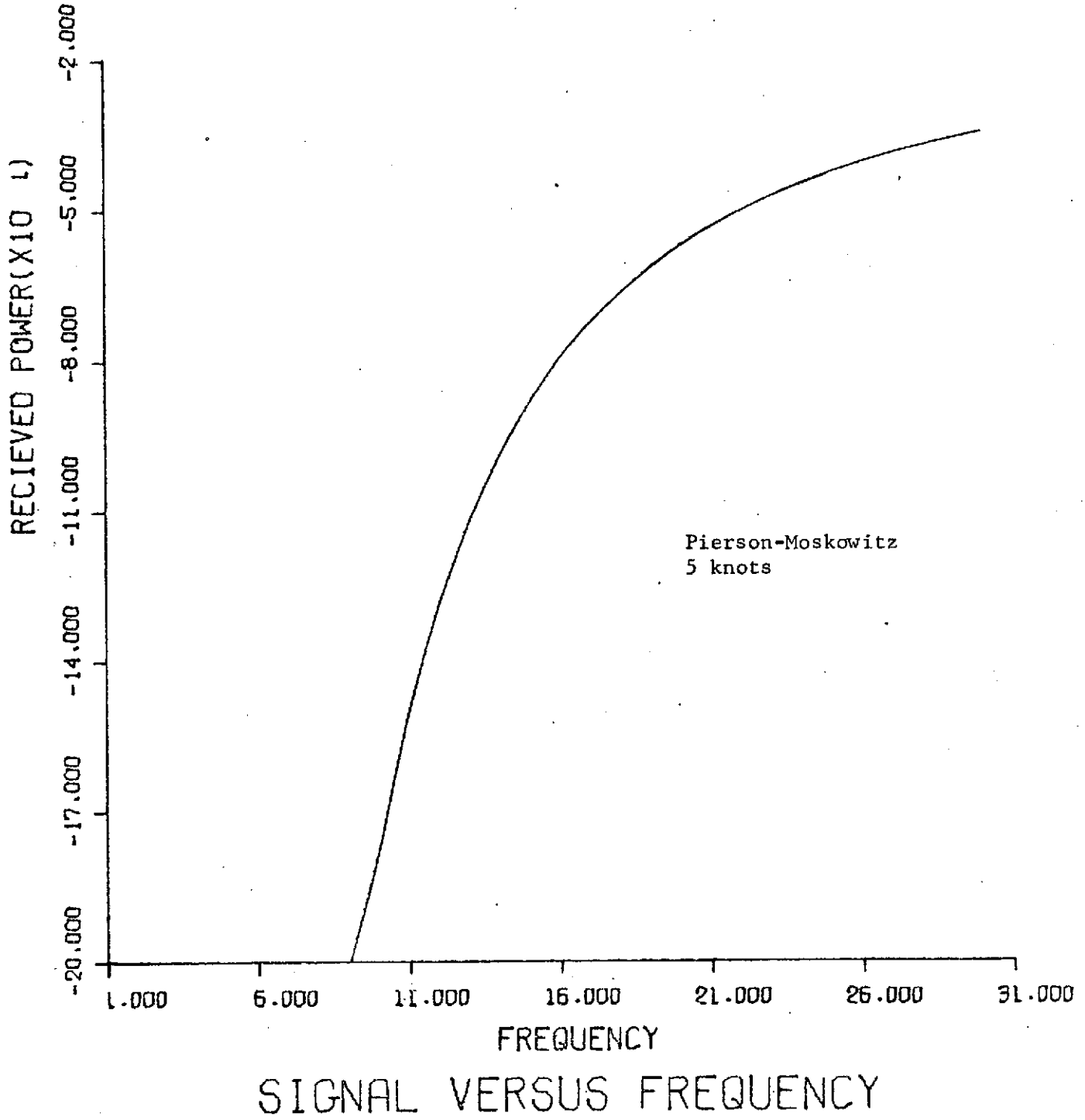

FIGURE 3. NORMALIZED RECEIVED POWER VERSUS FREQUENCY IN MHz FOR A 5 KNOT WIND VELOCITY, PIERSON-MOSKOWITZ SPECTRUM

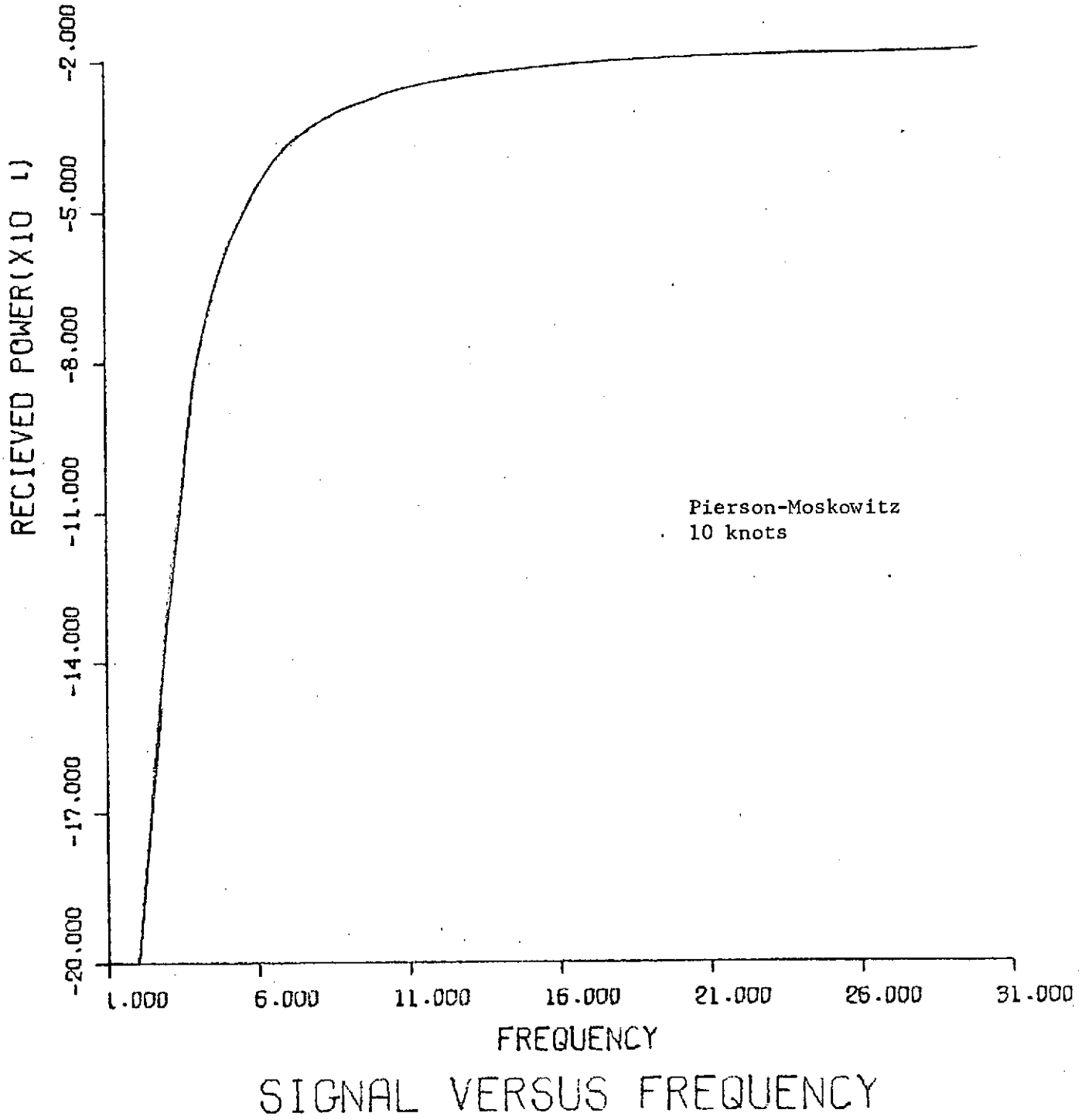

FIGURE 4. NORMALIZED RECEIVED POWER VERSUS FREQUENCY IN MHz FOR A 10 KNOT WIND VELOCITY, PIERSON-MOSKOWITZ SPECTRUM

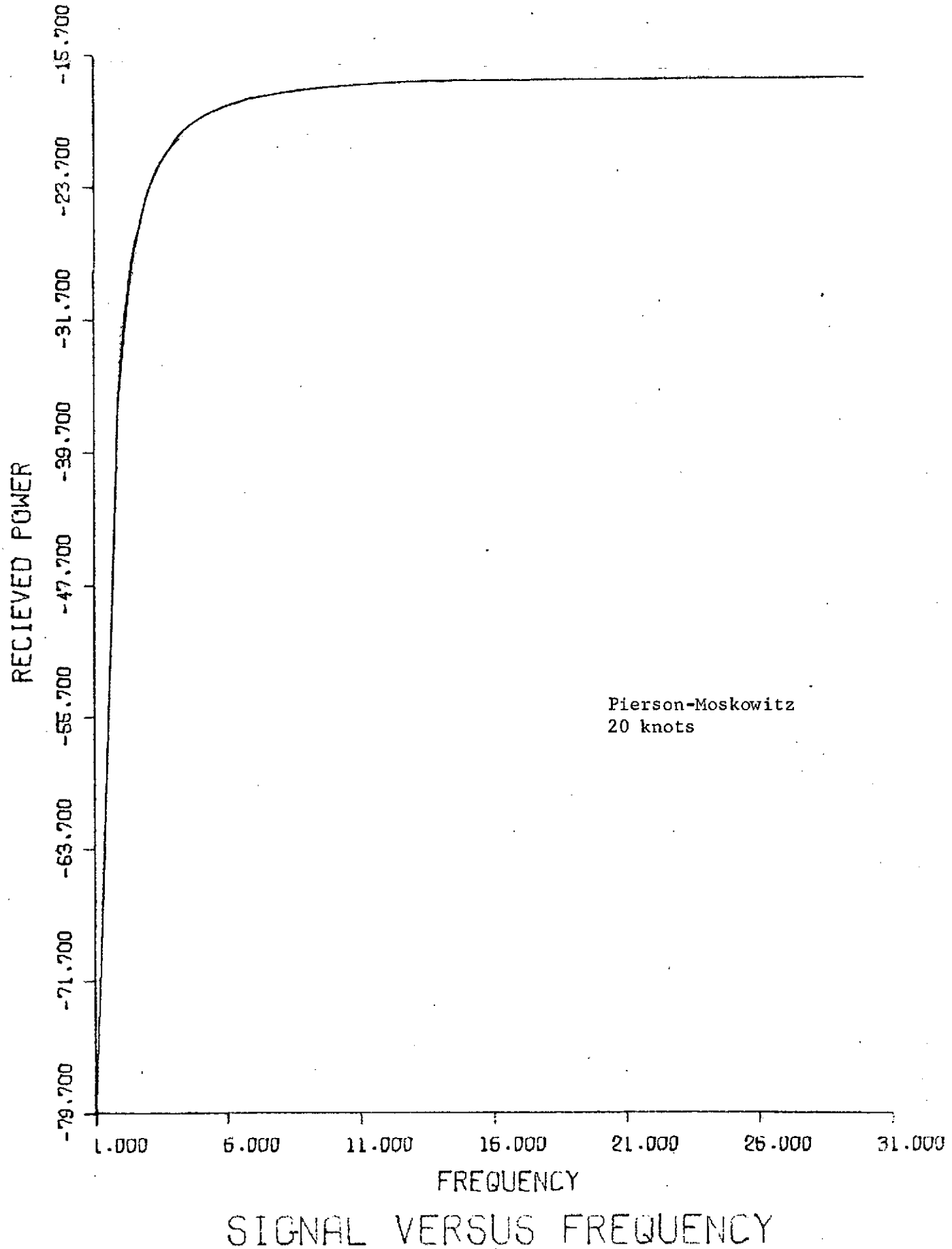

FIGURE 5. NORMALIZED RECEIVED POWER VERSUS FREQUENCY IN MHz FOR A 20 KNOT WIND VELOCITY, PIERSON-MOSKOWITZ SPECTRUM

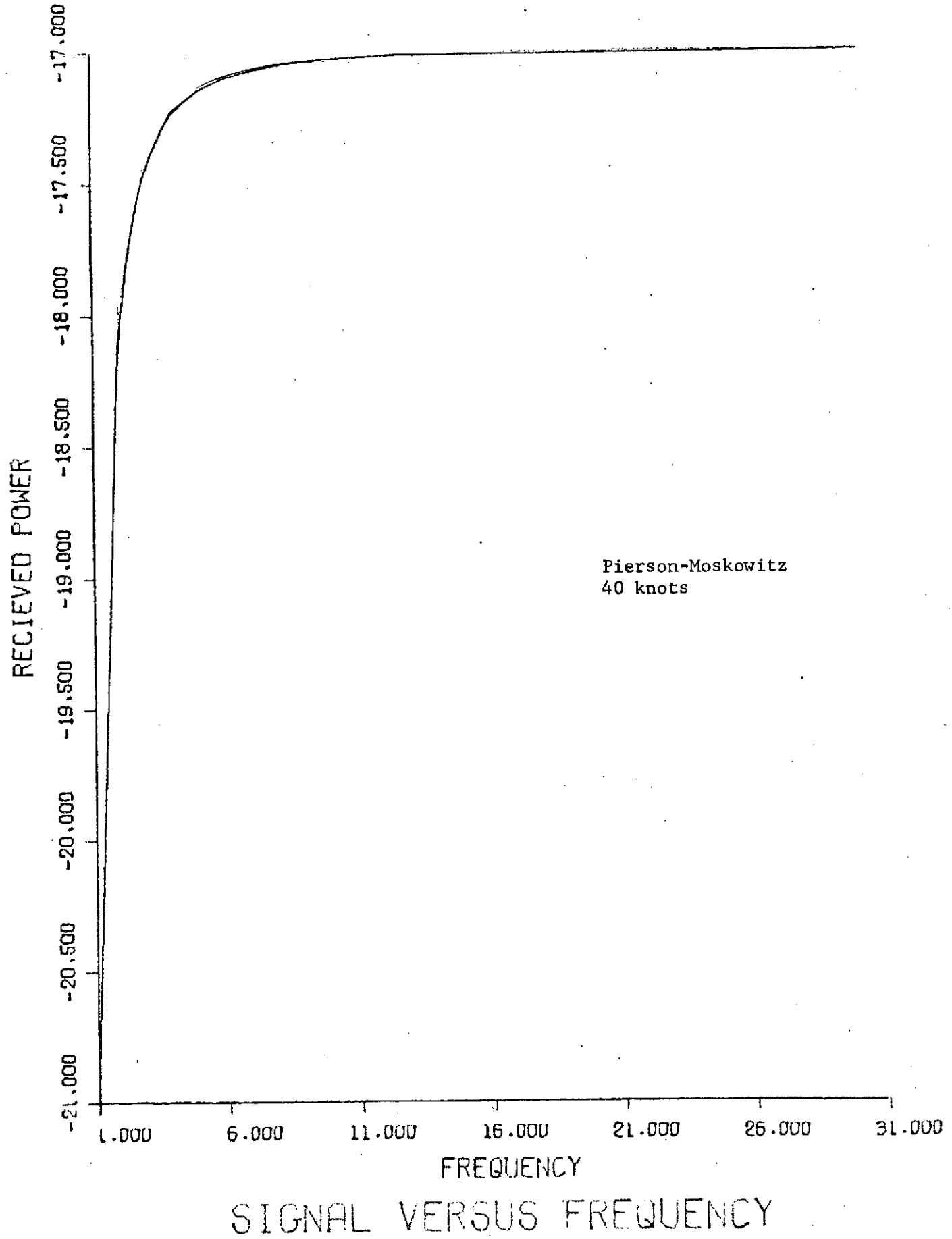

FIGURE 6. NORMALIZED RECEIVED POWER VERSUS FREQUENCY IN MHz FOR A 40 KNOT WIND VELOCITY, PIERSON-MOSKOWITZ SPECTRUM

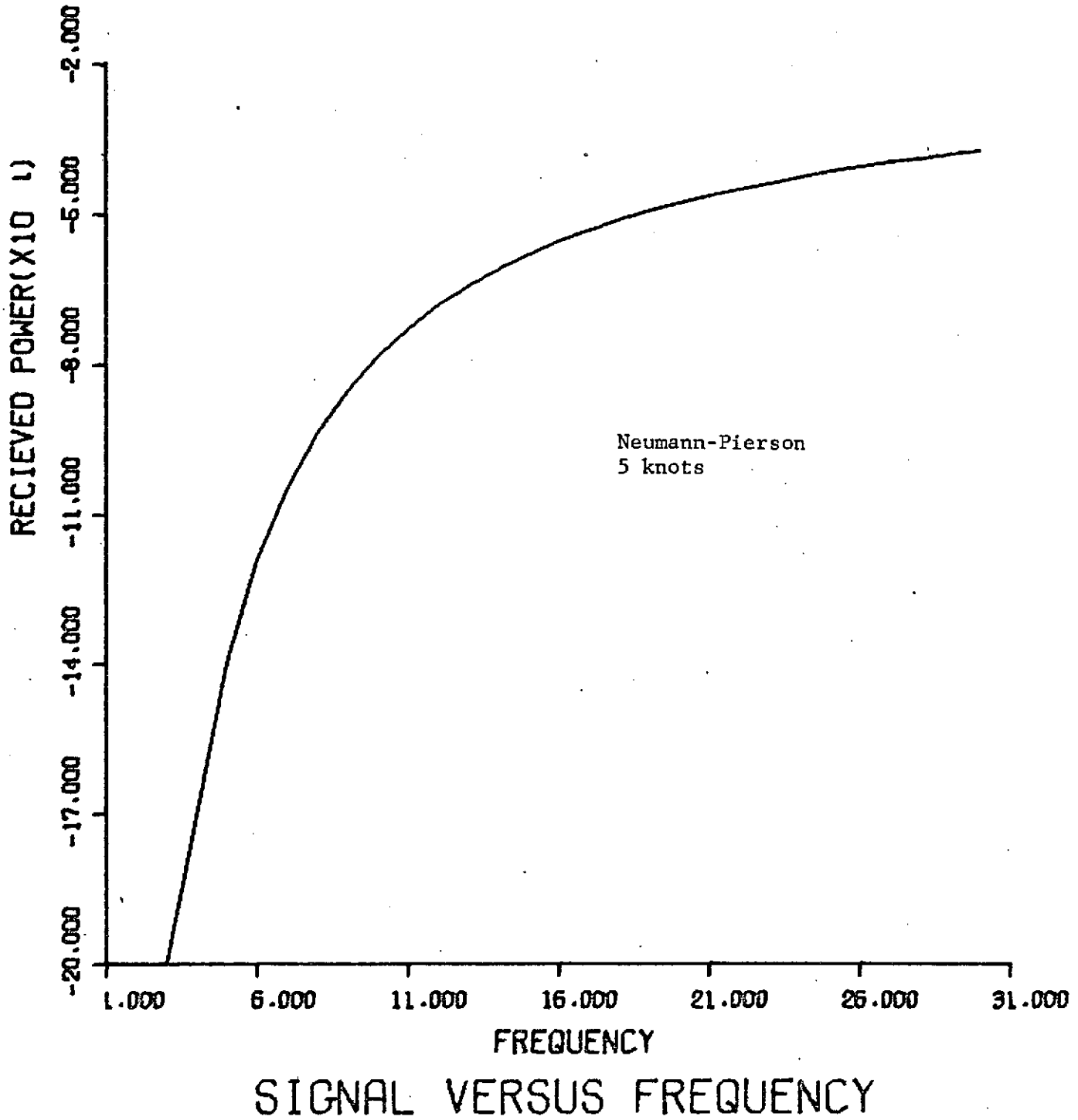

FIGURE 7. NORMALIZED RECEIVED POWER VERSUS FREQUENCY IN MHz FOR A 5 KNOT WIND VELOCITY, NEUMANN-PIERSON SPECTRUM

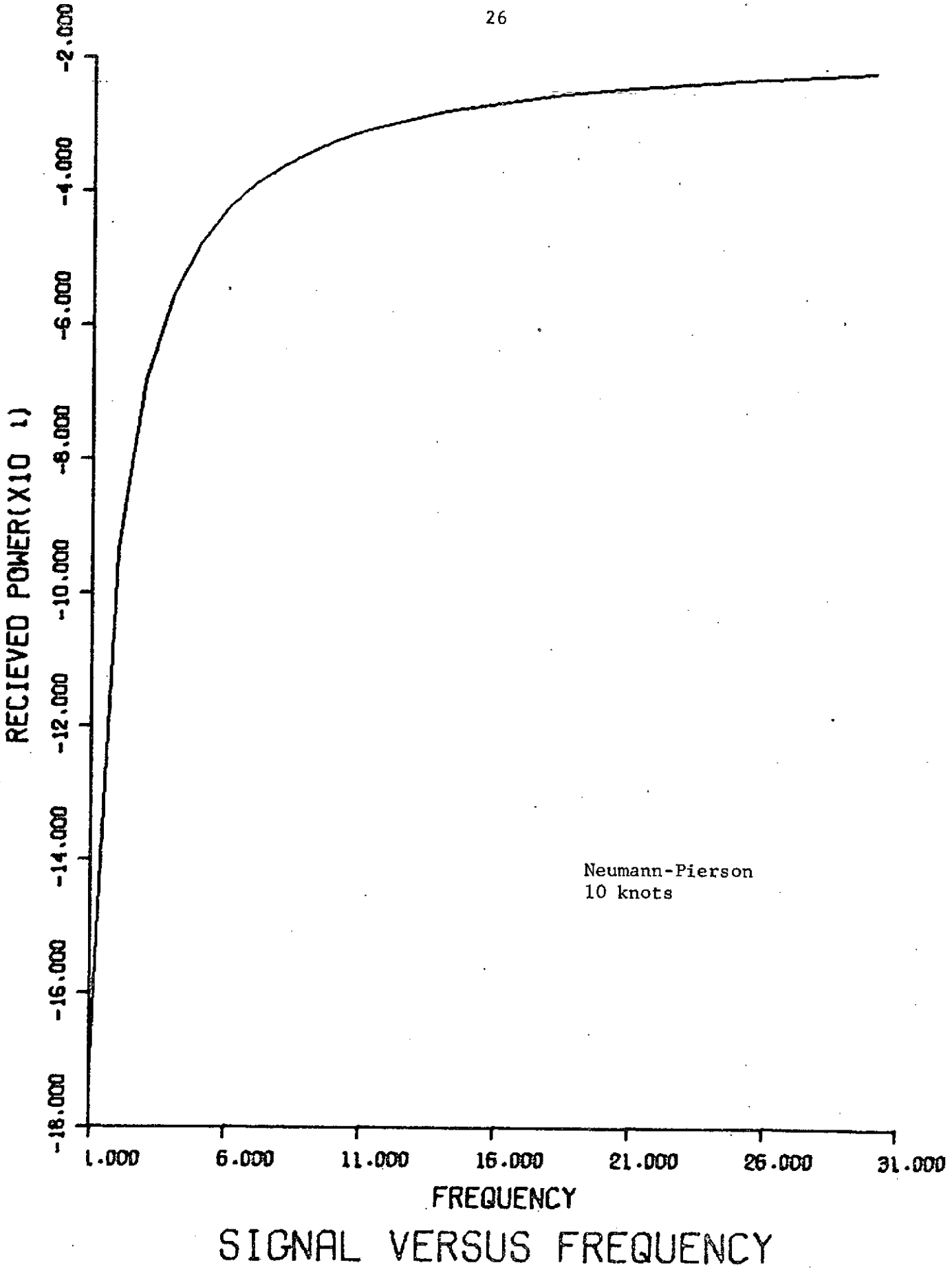

FIGURE 8. NORMALIZED RECEIVED POWER VERSUS FREQUENCY IN MHz FOR A 10 KNOT WIND VELOCITY, NEUMANN-PIERSON SPECTRUM

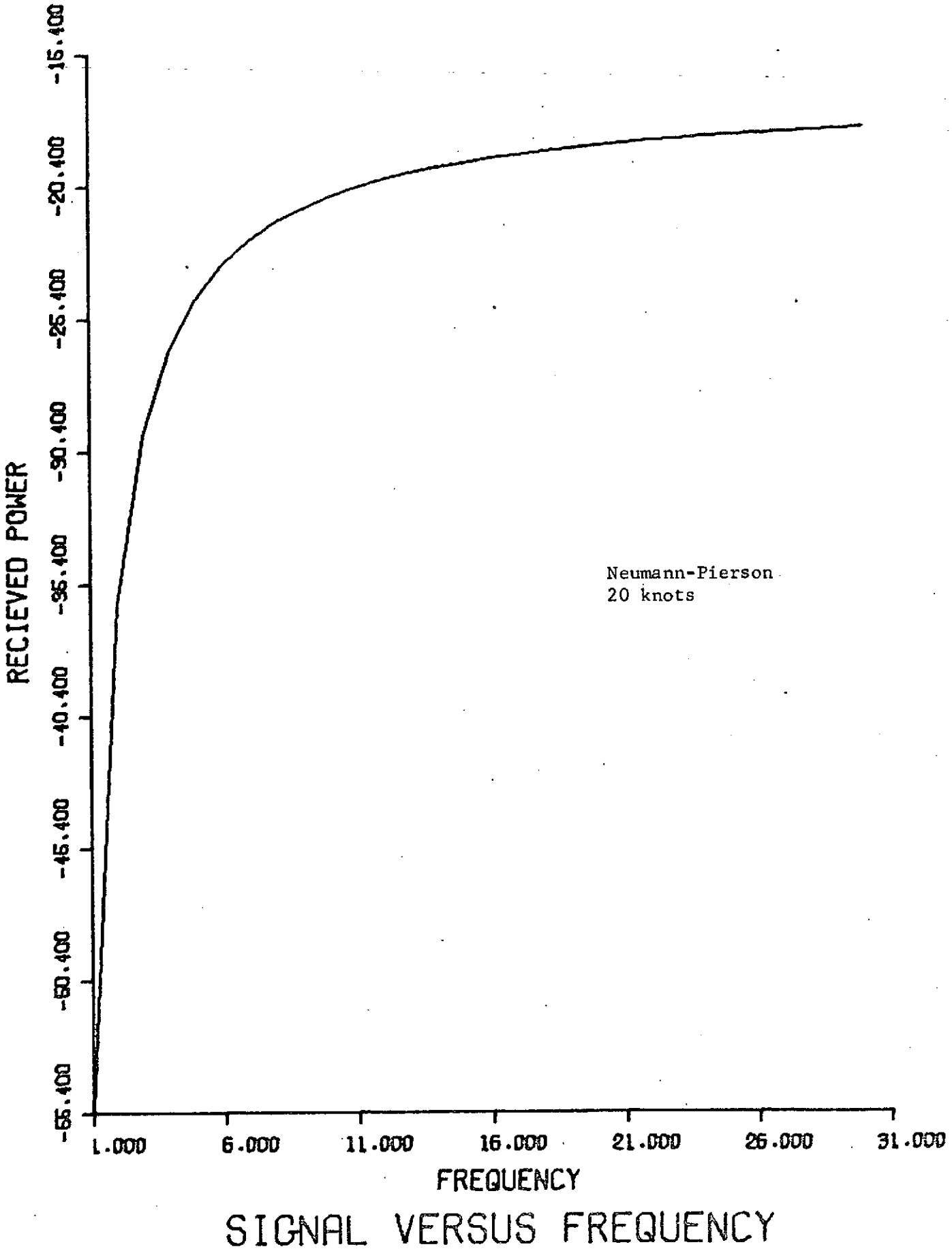

FIGURE 9. NORMALIZED RECEIVED POWER VERSUS FREQUENCY IN MHz FOR A 20 KNOT WIND VELOCITY, NEUMANN-PIERSON SPECTRUM

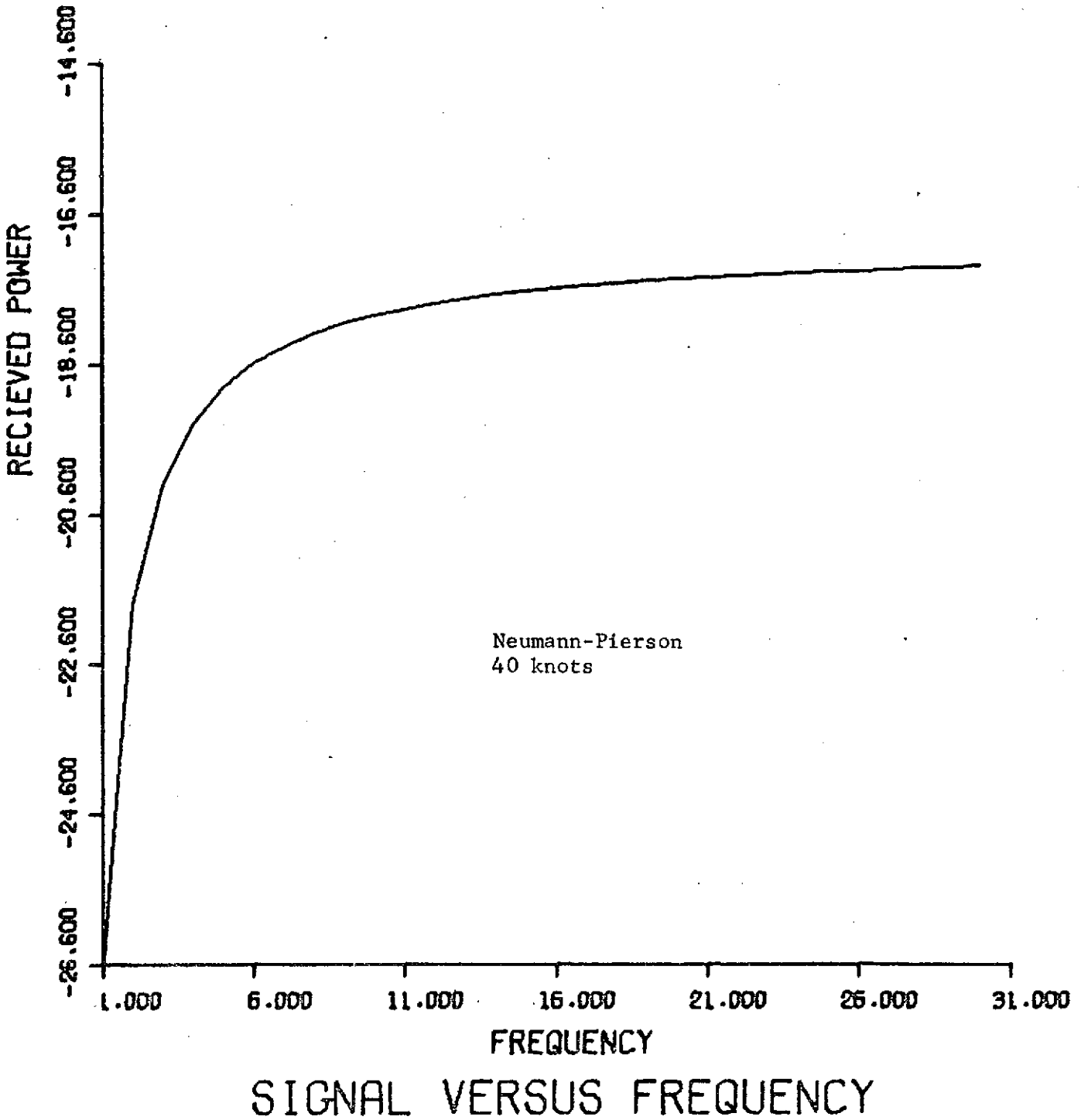

FIGURE 10. NORMALIZED RECEIVED POWER VERSUS FREQUENCY IN MHz FOR A 40 KNOT WIND VELOCITY, NEUMANN-PIERSON SPECTRUM

It is apparent that for the higher wind velocities the surface spectrum is saturated at the higher frequencies, and drops off quite steeply at the low frequency end. The actual non-directional surface spectrum is of course given by $k_o^{-4}\sigma_o$. To the extent that σ^o can be determined accurately, which is equivalent to a knowledge of the multiplier dK of Equation (34) and the received power, then the received power can be related directly to the true surface spectrum.

In order to determine sea state or RMS wave height from the received signal, it is necessary only that the integral

$$\int k_o^{-4}\ \sigma_o\ k_o dk_o \qquad (35)$$

be evaluated. To the extent that this can be done accurately, then the true RMS surface height results irrespective of any surface models. The models used for the curves of Figures 3 through 10 were simply to illustrate the form that the received signal would have and the general dependence on frequency and wind velocity or sea state.

It should be noted, that if the ocean surface structure is of a mixed nature due to the presence of swell, shore effects, etc. as well as pure wind sea, the evaluation of the integral in Equation (35) will still result in a measure of the true RMS surface height in the region of interest.

Surface Spectrum Measurements Using UHF Scattering

The surface spectrum can also be measured by operating at two UHF frequencies which are separated by a frequency in the HF region. The cross-correlation coefficient between the power scattered at the two frequencies can be related to the surface slope spectrum at a wave number corresponding to the difference frequency. This technique, if feasible, would be essentially unaffected by ionospheric propagation phenomena and thus not subject to some of the limitations of the HF approach. In addition, the hardware difficulties associated with HF antennas at the lower frequencies would be obviated.

This approach could in principle be utilized in the same bistatic configuration as the HF technique or it could be used in a backscatter mode without requiring a transmitter on the surface.

The theoretical principles underlying this approach are presented in the following section.

Two-Frequency Correlation Technique for Measurement of Ocean Wave Surface Spectra

Initial Formulation

To demonstrate the concept and principles involved, the analysis will be restricted to (a) backscatter, (b) perfectly conducting surface, (c) horizontal polarization states, (d) a one-dimensional random surface corrugated along the plane of incidence, and (e) an incidence direction not too close to the specular direction (i.e., the vertical), but yet not so close to grazing that shadowing is a problem.

The analysis to follow is based on several approximations which appear either justifiable for the sea mathematically or vindicated by experimental data. These are

(a) The slopes of the ocean surface are not too steep.

(b) The height can be represented in a composite manner as the sum of two components, i.e., $\zeta(x) = \zeta_L(x) + \zeta_s(x)$, where ζ_L includes those ocean-wave components whose heights and lengths are greater than a wavelength, and ζ_s includes those smaller-scale short gravity waves whose heights are considerably less than a wavelength. The former alone produces quasi-specular scatter while the latter alone produces Bragg scatter.

The far-field Chu-Stratton integral equation for scatter is[6]

$$\overline{E}^s = \frac{i\omega\mu_o e^{ik_oR_o}}{4\pi R_o} \int_{-L/2}^{L/2}\int_{-L/2}^{L/2} \left[\left(\hat{n} \times \overline{H}^s\right) - \hat{k}_o^s \cdot \left(\hat{n} \times \overline{H}^s\right)\hat{k}_o^s - \frac{1}{\eta_o}\left(\hat{n} \times \overline{E}^s\right) \times \hat{k}_o^s\right] \times$$

$$\times\, e^{-ik_o\hat{k}_o^s \cdot \overline{r}'}\, ds' \quad , \tag{36}$$

with $\eta_o = \sqrt{\mu_o/\epsilon_o}$. The area within a radar resolution cell is taken for convenience to be a square of side L, where L is much greater than wavelength but much smaller than the distance to the radar, R_o. The incidence and (back)scatter unit direction vectors here are $\hat{k}_o^i = \hat{x}' \sin\theta - \hat{z}' \cos\theta$, $\hat{k}_o^s = -\hat{k}_o^i = -\hat{x}' \sin\theta + \hat{z}' \cos\theta$, $\overline{r} = x'\hat{x}' + \zeta_L(x')\hat{z}'$; these are illustrated in Figure 11.

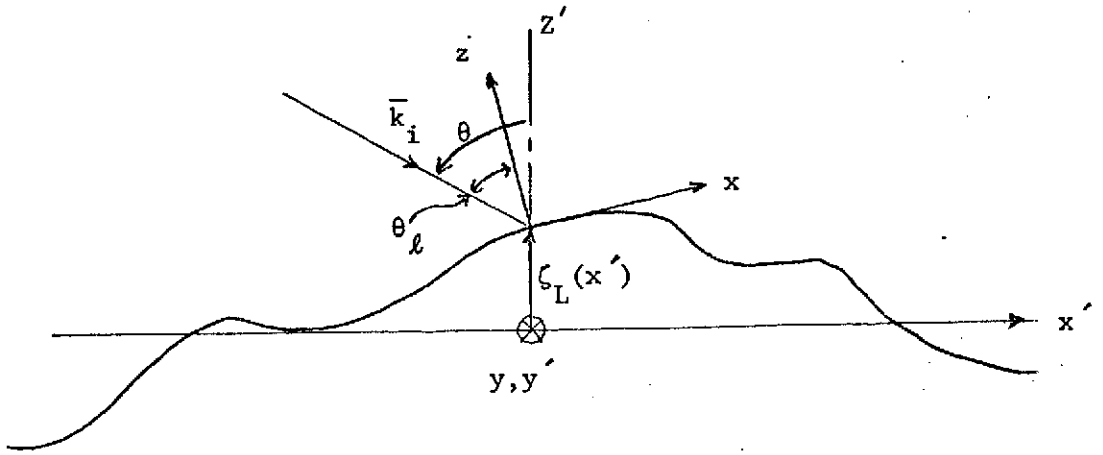

FIGURE 11. COMPOSITE ROUGH SURFACE AND BACKSCATTER GEOMETRY

On the surface, $\overline{E}^s$ and $\overline{H}^s$ are approximately composed of two terms: (a) the physical optics field, i.e., $2\hat{n} \times \overline{H}^i$, and (b) the scattered field predicted from the Rice theory. The latter produces scatter by the Bragg effect, and dominates the return reasonably far away from the specular direction, while the former dominates near the specular direction. Since we are interested only in the latter, the fields on the surface to be used in Eq. (36) are the Rice summations for the fields scattered in all directions from a slightly rough surface, $\zeta_s(x)$. The surface over which the integration is performed is $\zeta_L(x)$. Thus

$$ds' = \sqrt{1 + \left(\frac{\partial \zeta_L}{\partial x}\right)^2}\, dx'dy' \quad , \quad \text{and } \hat{n} = \left(-\frac{\partial \zeta_L}{\partial x}\hat{x}' + \hat{z}'\right) \Big/ \sqrt{1 + \left(\frac{\partial \zeta_L}{\partial x}\right)^2} \quad ,$$

and the integration now takes place over x' and y'.

The First-Order Scattered Fields at the Surface

The first-order locally scattered fields for horizontal polarization near a point x, y on ζ_L must now be found. These are:

$$E_x^s = e^{-ik_0\zeta_L \cos\theta} \cdot \sum_{m=-\infty}^{\infty} A_m E(m,z) \quad ,$$

$$E_y^s = e^{-ik_0\zeta_L \cos\theta} \cdot \sum_{m=-\infty}^{\infty} B_m E(m,z) \quad ,$$

$$E_z^s = e^{-ik_0\zeta_L \cos\theta} \cdot \sum_{m=-\infty}^{\infty} C_m E(m,z) \quad ,$$

where

$$E(m,z) = E^o \exp\left\{ia(m + \nu_\ell)x + ib(m)z\right\} \quad ,$$

where $b(m) = \sqrt{k_o^2 - a^2(m + \nu_\ell)^2}$, $a = \frac{2\pi}{L_s}$.

Here, the phase factor $e^{-ik_o\zeta_L \cos\theta}$ must be used because the incident field strikes the surface not with origin at $z' = 0$, but at $z' = \zeta_L$. The quantity ν_ℓ is $\nu_\ell = (k_o \sin\theta_\ell)/a$, where θ_ℓ and hence ν_ℓ are functions of the slope of the large-scale surface at the local incidence point x', $\zeta_L(x')$.

Since we are dealing with a one-dimensional surface, we can define the height above the large-scale undulation as $z = \zeta_s(x)$, with Fourier expansion

$$\zeta_s(x) = \sum_{m=-\infty}^{\infty} P(m)\, e^{iamx} \quad ,$$

where the spatial spectrum $W(p)$ is defined in terms of the Fourier coefficients $P(m)$ in much the same manner as for a two-dimensionally rough surface as

$$\langle P(m)P(n)\rangle = \begin{cases} 0 \text{ for } m \neq -n \\ \\ \dfrac{\pi}{L_s} W(p) \text{ for } m = -n \end{cases} \quad .$$

For horizontal polarization, we have the following results from the Rice solution for the first-order scattering coefficients:

$$A_m^{(1)} = 0 \quad ; \quad C_m^{(1)} = 0 \quad ;$$

$$B_m^{(1)} = i2k_o \cos\theta_\ell \, P(m) \quad .$$

Evaluation of Factors in Integrand of Eq. (36)

We now proceed to evaluate and simplify the various factors in the integrand of Eq. (1), using the first-order electric field expressed derived above. $\overline{H}^s$ is obtained from the following Maxwell equation:

$$\nabla \times \overline{E}^s = -\frac{\partial \overline{B}^s}{\partial t} = -\mu_o \frac{\partial \overline{H}^s}{\partial t} = i\omega\mu_o \overline{H}^s$$

where the time factor $e^{-i\omega t}$ is used throughout and suppressed.†

† Note: $\partial/\partial y = 0$ because nothing varies in y-direction.

$$\therefore \bar{H}^s = \frac{1}{i\omega\mu_o} \begin{vmatrix} \hat{x} & \hat{y} & \hat{z} \\ \partial/\partial x & 0 & \partial/\partial z \\ 0 & E_y^s & 0 \end{vmatrix} = \frac{1}{i\omega\mu_o} \left(\hat{z} \frac{\partial E_y^s}{\partial x} - \hat{x} \frac{\partial E_y^s}{\partial z} \right) .$$

Note that this is the local field near x' and $\zeta_L(x')$; hence evaluating $\bar{H}^s$ in terms of E_y and substitution into Eq. (36) gives

$$\bar{E}^s(R_o) = \frac{-iLe^{i2k_oR_o}\hat{y}'}{4\pi R_o} \sum_{m=-\infty}^{\infty} B_m \int_{-L/2}^{L/2} \left[\frac{\partial \zeta_L}{\partial x} \left(b(m) \sin\theta_s - a(m + \nu_\ell) \cos\theta_s \right.\right.$$

$$\left. + k_o \sin\theta \right) + b(m) \cos\theta_s + a(m + \nu_\ell) \sin\theta_s$$

$$\left. + k_o \cos\theta \right] e^{iamx + ia\nu_\ell x + ik_o \sin\theta x' - i2k_o \cos\theta \zeta_L} dx' . \quad (37)$$

Application of Stationary Phase Principle

Now, we look at each term of the summation separately, and evaluate the factor in square brackets in the above integrand at the specular, or stationary phase slopes. In other words, the expression in brackets is a function of $\partial\zeta_L/\partial x'$, which varies with x'. For a given m, however, only certain regions with certain slopes can contribute to the scattered field. These are found from setting the derivative of the phase equal to zero.

Before we do this, however, we will convert entirely from x to x'. We do this by noting initially that

$$\theta = \theta_\ell + \theta_s \quad ; \quad \nu_\ell = \frac{k_o \sin\theta_\ell}{a} \quad ; \quad \theta_s = \tan^{-1}\left[\frac{\partial \zeta_L}{\partial x}\right]$$

(note that $x' = x \cos\theta_s$). Thus the terms appearing in the exponential become

$$amx = \frac{amx'}{\cos\theta_s} \simeq amx' \left(1 + \frac{1}{2}\theta_s^2\right) \simeq amx'$$

$$a\nu_{\ell x} = k_o \sin\theta_{\ell x} = k_o x' \sin\theta\left(1 + \theta_s^2\right) \simeq k_o x' \sin\theta \quad .$$

The phase is now given by:

$$\therefore \varphi(x') = amx' + 2k_o x' \sin\theta - 2k_o \zeta_L(x') \cos\theta$$

$$\therefore \frac{d\varphi}{dx} = 0 = am + 2k_o \sin\theta - 2k_o \left.\frac{d\zeta_L}{\partial x}\right|_{sp} \cos\theta$$

$$\left.\frac{\partial\zeta_L}{dx}\right|_{sp} = \frac{am + 2k_o \sin\theta}{2k\cos\theta} = \tan\theta_s \Big|_{sp} \quad .$$

This conforms with the expected Bragg scatter criterion, which says that a diffraction grating of spatial wavenumber am, tipped at an angle θ_s with the x′ axis, will produce backscatter in a direction $-\theta$ if $am = 2k_o \cos\theta\,(\partial\zeta_L/\partial x') - 2k_o \sin\theta$.

Now, let us evaluate the factor in square brackets in the integrand at the stationary phase value and try to simplify it. If we retain only first-order terms in $\partial\zeta_L/\partial x'$ (or θ_s), then it can be shown that

$$[m]_{sp} = b(m) + \frac{amk_o \sin\theta + 2k_o^2}{2k_o \cos\theta} \quad .$$

Calculation of Average Scattered Power

We now square $|E^s|$ and then evaluate its average in separate stages. Denote $\overline{E}^s = E^s \hat{y}'$. Then, from Equation (37), we have

$$|E^s|^2 = \frac{L^2}{16\pi^2 R_\delta^2} \sum_{m_1} \sum_{m_2} B_{m_1} B_{m_2} [m_1]_{sp} [m_2]_{sp} \int_{-L/2}^{L/2} dx_1' \int_{-L/2}^{L/2} dx_2'$$

$$\times e^{ia(m_1 x_1' - m_2 x_2') + i2k_o \sin\theta(x_1' - x_2') - i2k_o \cos\theta\,[\zeta_L(x_i) - \zeta_L(x_2')]} \quad ,$$

where we have made the transformation indicated on page 34 to the x′ system from the x system.

At this point, let us drop the primes on all the x′s for convenience. Also, substitute

$$B_m = i2k_o \cos \theta_\ell \, P(m) \quad ,$$

where $\theta_\ell = \theta - \theta_s$ is the local angle of incidence.

Hence

$$\cos \theta_\ell \simeq \cos \theta + \frac{\partial \zeta_L}{\partial x} \sin \theta \quad .$$

Defining

$$\{am\} = [m]_{sp} \cos \theta_\ell \Big|_{sp} \quad ,$$

then

$$|E^s|^2 = \frac{k_o^2 L^2}{4\pi^2 R_o^2} \sum_{m_1} \sum_{m_2} \{am_1\}\{am_2\}^* P(m_1) P^*(m_2) \times \int_{-L/2}^{L/2} dx_1 \int_{-L/2}^{L/2} dx_2$$

$$\times e^{ia(m_1 x_1 - m_2 x_2) + i2k_o \sin \theta (x_1 - x_2) - i2k_o \cos \theta (\zeta_L(x_1) - \zeta_2(x_2)} \quad . \quad (38)$$

Now, averaging $|E^s|^2$ first with respect to the small-scale roughness process. We assume of course that ζ_s is statistically independent of ζ_L. Also, let us replace am = p with $k_o \eta$, where η is a normalized (with respect to radio wavelength) wavenumber.

From the definition of the Fourier series for ζ_s, we have

$$\langle P(m_1)P^*(m_2)\rangle_s = \begin{cases} \frac{\pi}{L_s} W(k_o\eta) & \text{for } m_1 = m_2 \\ 0 & \text{for } m_1 \neq m_2 \end{cases} ,$$

where $\langle\ \rangle_s$ indicates average with respect to the small-scale structure.

Thus

$$\langle |E_s|^2 \rangle_s = \frac{L^2k_o^2}{4\pi L_s R_o^2} \sum_m \{\eta\}^2 W(k_o\eta) \int_{-L/2}^{L/2} dx_1 \int_{-L/2}^{L/2} dx_2\, e^{ik_o(\eta + 2\sin\theta)(x_1 - x_2)}$$

$$- i2k_o \cos\theta\,[\zeta_L(x_1) - \zeta_L(x_2)] \quad .$$

Now, let us change variables to $\Delta x \equiv x_1 - x_2$ and integrate over the remaining variable. The integration limits over Δx can be replaced by $\pm\infty$, since L is taken as much larger than the correlation length of the large-scale roughness.

$$\therefore \langle |E^s|^2 \rangle_s = \frac{L^3k_o^2}{4\pi L_s R_o^2} \sum_m \{\eta\}^2 W(k_o\eta) \int_{-\infty}^{\infty} d\Delta x$$

$$\times\, e^{ik_o(\eta + 2\sin\theta) - i2k_o\cos\theta[\zeta_L(x_1) - \zeta_L(x_2)]} \quad .$$

Next, we average over the large-scale roughness structure, $\langle\ \rangle_L$. This completes the averaging process, and we denote $\ll |E^s|^2\rangle_s\rangle_L \equiv \langle |E^s|^2\rangle$. The large scale averaging process affects only the integral.

The average of this integral in the high-frequency limit ($k_o\zeta_L \to \infty$) will be evaluated by the technique outlined in Reference (7), i.e.,

$$\lim_{k_o \to \infty} \left\{ k_o \int_{-\infty}^{\infty} d\Delta x\, e^{ik_o q_x \Delta x} \left\langle e^{ik_o q_z(\zeta_L(x_1) - \zeta_L(x_2))} \right\rangle_L \right\} = \frac{2\pi}{q_z} P_L\left(+\frac{q_x}{q_z}\right) ,$$

where $q_x = \eta + 2 \sin\theta$ and $q_z = + 2 \cos\theta$.

Hence

$$\langle |E^s|^2 \rangle = \frac{L^3 k_o 2\pi}{4\pi L_s R_o^2 q_z} \sum_m \{\eta\}^2 \, W(k_o\eta) \, P_L\left(+\frac{q_x}{q_z}\right) \quad ,$$

where $P_L(d\zeta_L/dx)$ is the probability density function of the large-scale slopes of the surface.

Converting the sum into an integral, i.e.,

$$\sum_m \langle P(m) P^*(m) \rangle = \frac{1}{2} \int_{-\infty}^{\infty} W(p)\,dp \quad ,$$

we obtain

$$\langle |E^s|^2 \rangle = \frac{L^3 k_o^2}{4\pi R_o^2 q_z} \int_{-\infty}^{\infty} \{\eta\}^2 \, W(k_o\eta) \, P_L\left(+\frac{q_x}{q_z}\right) d\eta \quad . \qquad (39)$$

Covariance of the Scattered Power at Two Frequencies

Now the covariance of the power at the two frequencies, represented by radio wavenumbers k_a and k_b will be evaluated. To do this, we go back to Eq. (38).

Note first of all that $\{am\}$ can be written in terms of η, with k_a or k_b removed.

$$\therefore P_a \equiv |E^s(k_a)|^2 = \frac{k_a^2 L^2}{4\pi^2 R_o^2} \sum_{m_1} \sum_{m_2} \{am_1\}\{am_2\}^* P(m_1) P^*(m_2) \int_{-L/2}^{L/2} dx_1 \int_{-L/2}^{L/2} dx_2$$

$$\times e^{ia(m_1 x_1 - m_2 x_2)} \cdot e^{i2k_a \sin\theta\,(x_1 - x_2) \,-\, i2k_a \cos\theta\,(\zeta_L(x_1) - \zeta_L(x_2))} \quad ,$$

where we have, as before, dropped the primes on the x-y coordinates.

Hence, the covariance is

$$P_a P_b = \frac{k_a^2 k_b^2 L^4}{16\pi^4 R_0^4} \sum_{m_1} \sum_{m_2} \sum_{m_3} \sum_{m_4} \{am_1\}\{am_2\}^* \{am_3\}\{am_4\}^* P(m_1)P^*(m_2)P(m_3)P^*(m_4)$$

$$\times \int_{-L/2}^{L/2}\int\int\int dx_1 dx_2 dx_3 dx_4 \, e^{ia(m_1x_1 - m_2x_2 + m_3x_3 - m_4x_4)}$$

$$+ i2 \sin\theta\,(k_a x_1 - k_a x_2 + k_b x_3 - k_b x_4)$$

$$\times e^{-i2\cos\theta\,(k_a\zeta_L(x_1) - k_a\zeta_L(x_2) + k_b\zeta_L(x_3) - k_b\zeta_L(x_4))} \quad . \qquad (40)$$

Average Over Small-Scale Structure

We now average over the small-scale structure, noting that for Gaussian surfaces,

$$\langle P(m_1)P^*(m_2)P(m_3)P^*(m_4)\rangle_s = \begin{cases} \langle P(m_1)P^*(m_2)\rangle_s\langle P(m_3)P^*(m_4)\rangle_s + & \text{(i)} \\ + \langle P(m_1)P(m_3)\rangle_s\langle P^*(m_2)P^*(m_4)\rangle_s + & \text{(ii)} \\ + \langle P(m_1)P^*(m_4)\rangle_s\langle P^*(m_2)P(m_3)\rangle_s \quad . & \text{(iii)} \end{cases} \qquad (41)$$

Of the three terms present in the above equation, we note that the second, (ii), contributes nothing except near the specular direction ($\theta \to 0$); this occurs because it is nonzero only when $m_3 = -m_1$ and $m_4 = -m_2$. When this happens, we have $iam_1(x_1 - x_3) + i2 \sin\theta(k_a x_1 + k_b x_1)$ in the exponent, which causes it to oscillate rapidly except when $\theta = 0$.

The first term, (i), contributes in much the same manner as it did when we averaged P separately to obtain Eq. (39).

Average Over Large-Scale Structure

Let us examine the first term, (i), of Eq. (41) therefore:

$$\langle P_a P_b \rangle_{si} = \frac{k_a^2 k_b^2 L^4}{16\pi^4 R_o^4} \cdot \frac{1}{4} \int_{-\infty}^{\infty} dp_1 \int_{-\infty}^{\infty} dp_3 \{am_1\}^2 \{am_3\}^2 \, W(k_a \eta_1) W(k_b \eta_2) \cdot$$

$$\times \int_{-L/2}^{L/2} \iiint e^{ik_a(\eta_1 - 2 \sin\theta)(x_1 - x_2) + ik_b(\eta_3 - 2\sin\theta)(x_3 - x_4)}$$

$$\times e^{-i2\cos\theta[k_a(\zeta_{L1} - \zeta_{L2}) + k_b(\zeta_{L3} - \zeta_{L4})]} \, dx_1 dx_2 dx_3 dx_4 \quad .$$

Let $\Delta x_1 \equiv x_1 - x_2$ and $\Delta x_3 \equiv x_3 - x_4$. We now integrate over the large scale roughness, noting that:

$$\lim_{\substack{k_a \to \infty \\ k_b \to \infty}} \left\{ k_a k_b \int_{-\infty}^{\infty} d\Delta x_1 \int_{-\infty}^{\infty} d\Delta x_2 \, e^{ik_a q_{x1} \Delta x_1 + ik_b q_{x3} \Delta x_3} \left\langle e^{ik_a q_z (\zeta_L(x_1) - \zeta_L(x_2))} \right.\right.$$

$$\left.\left. + ik_b q_z (\zeta_L(x_3) - \zeta_L(x_4)) \right\rangle_L \right\} \Rightarrow \frac{4\pi^2}{q_z^2} P_L \left(+ \frac{q_{x1}}{q_z} , + \frac{q_{x3}}{q_z} ; x_1, x_3 \right) ,$$

where $P_L[(\partial\zeta_{L1}/\partial x_1), (\partial\zeta_{L3}/\partial x_3); x_1, x_3]$ is the joint probability density function of the two surface slopes $\partial\zeta_{L1}/\partial x_1$ and $\partial\zeta_{L3}/\partial x_3$ at two different surface points, x_1, and x_3.

We assume that the large-scale roughness process possesses statistical stationarity so that this joint density function does not vary absolutely with x_1 or x_3, but rather with their separation, $|x_3 - x_1|$. This is certainly true of the sea over areas of concern in experiments here (e.g., less than 100 km in extent). Thus:

$$\langle P_a P_b \rangle_i = \frac{k_a k_b L^4}{q_z^2 16\pi^2 R_0^4} \int_{-\infty}^{\infty} dp_1 \int_{-\infty}^{\infty} dp_3 \{\eta_1\}^2 \{\eta_3\}^2 W(k_a\eta_1) W(k_b\eta_3) \times \int_{-L/2}^{L/2}\int dx_1 dx_3$$

$$\times P_L\left(+\frac{q_{x1}}{q_z}, +\frac{q_{x3}}{q_z}; x_1, x_3\right) .$$

We now proceed to get an approximate evaluation of this integral, first interchaning the orders of integration such that $\int dp_1 \int dp_3$ is done first.

These integrals in dp_1, dp_3 can be converted to integrals in $d\eta_1$, $d\eta_3$, which can in turn be converted to slopes by letting $s_1 = q_{x1}/q_z$, $s_3 = q_{x3}/q_z$. The factors $\{\eta_1\}^2 W(k_a\eta_1)$ and $\{\eta_3\}^2 W(k_b\eta_3)$ can also be expressed as functions of s_1 and s_3, and can then be expanded into Taylor series such that

$$\{\eta_1\}^2 W(k_a\eta_1) = \{\eta_1\}^2 W(k_a\eta_1)\Big|_{s_1=0} + \frac{d[\{\eta_1\}^2 W(k_a\eta_1)]}{ds_1}\Big|_{s_1=0} s_1 + \cdots ,$$

with a similar series for $\{\eta_3\}^2 W(k_b\eta_3)$.

Higher-order terms in the series, being dependent upon the slopes s_1 and s_3, should be small when these slopes are small; they are for the sea, as implied in $P_L(s_1, s_3; x_1, x_3)$, which has a variance of the order of $\tan^{-1}(\langle s_1^2\rangle^{1/2}) \simeq 7°$ to $8°$.

Hence, if we retain only two terms of the series and do the integrations over s_1 and s_3 we will end up with two non-zero quantities:

(a) $$k_a k_b \{\eta_1\}^2 W(k_a\eta_1)\Big|_{s_1=0} \{\eta_3\}^2 W(k_b\eta_3)\Big|_{s_3=0} \times \int_{-\infty}^{\infty}\int_{-\infty}^{\infty} ds_1 ds_3 P_L(s_1, s_3; x_1, x_3) ,$$

and (b) $$k_a k_b \frac{d(\{\eta_1\}^2 W(k_a\eta_1))}{ds_1}\Big|_{s_1=0} \frac{d(\{\eta_1\}^2 W(k_b\eta_3))}{ds_3}\Big|_{s_3=0}$$

$$\times \int_{-\infty}^{\infty}\int ds_1 ds_3 s_1 s_3 P_L(s_1, s_3; x_1, x_3) .$$

The integral in (a) above is identically unity by virtue of the normalization of a probability density function.

The integral in (b) above is $R_{sL}(\Delta x)$, where $R_{sL}(\Delta x)$ is $\langle s_1 s_3 \rangle_L$, the covariance function of the two slopes s_1 and s_3 separated by $\Delta x = x_3 - x_1$.

Thus we have:

$$\langle P_a P_b \rangle_i = \frac{k_a^2 k_b^2 L^4}{q_z^2 16\pi^2 R_o^4} \left\{ \{\eta\}^4 \, W^2(k_o\eta) \Big|_{s=0} \int_{-L/2}^{L/2}\int dx_1 dx_3 \right.$$

$$\left. + \left[\frac{d[\{\eta\}^2 \, W(k_o\eta)]}{ds} \Big|_{s=0} \right]^2 \cdot \int_{-L/2}^{L/2} dx_1 \int_{-L/2-x_1}^{L/2-x_1} d(\Delta x) R_{SL}(\Delta x) \right\} \quad . \quad (42)$$

The integral in the first term is simple: L^2.

The integral in the second term should be zero for the following reason: if L is very large with respect to the correlation length of the large-scale structure, then we can replace the limits by $\pm\infty$. Then we have $\int_{-\infty}^{\infty} R_{SL}(\Delta x) d(\Delta x)$, which is $W_{SL}(0)$, the slope spectrum of the large-scale roughness evaluated at zero wavenumber. This is zero, however, since there are never ocean waves with zero wavenumber, or infinite wavelength, present on the sea.

Thus the answer for the first term is:

$$\langle P_a P_b \rangle_i \approx \frac{k_a^2 k_b^2 L^6}{q_z^2 16\pi^2 R_o^4} \{\eta\}^4 \, W^2(k_o\eta) \Big|_{s=0} \quad . \quad (43)$$

This is the square of $\langle |E^s|^2 \rangle$ given in Eq. (39), if that equation is evaluated in the same, approximate manner by expanding $\{\eta\}^2 \, W(k_o\eta)$ in a series.

Now, let us examine the third term, (iii), of Eq. (41):

$$\langle P_a P_b \rangle_{siii} = \frac{k_a^2 k_b^2 L^4}{16\pi^4 R_o^4} \cdot \frac{1}{4} \int_{-\infty}^{\infty} dp_1 \int_{-\infty}^{\infty} dp_3 \{a m_1(k_a)\}\{a m_1^*(k_b)\}\{a m_3(k_b) a m_3^*(k_a)\}$$

$$\times W(k_a\eta_1) W(k_b\eta_3) \int_{-L/2}^{L/2}\int\int\int dx_1 dx_2 dx_3 dx_4 \times$$

$$\times e^{ik_b(\eta_1 - 2\sin\theta)(x_1 - x_4) + ik_a(\eta_3 - 2\sin\theta)(x_3 - x_2)}$$

$$\times e^{i2\sin\theta\Delta k(x_1 - x_3) - i2\cos\theta\left[k_b\left(\zeta_{L1} - \zeta_{L4}\right) + k_a\left(\zeta_{L3} - \zeta_{L2}\right)\right] + 0} \quad ,$$

where $\Delta k \equiv k_a - k_b$ = separation (beat) wavenumber.

Also, we note from the orthogonality requirement on the small-scale Fourier coefficients, P(m), that $m_4 = m_1$ and $m_2 = m_3$.

Also, the quantity 0 in the exponential argument refers to all terms of the order of $\Delta k\zeta_L \cos\theta$ or smaller; Δk is to be kept small enough that it will make $\Delta k\zeta_L$ considerably less than unity. Hence, all such terms in the exponential are to be neglected here.

We note that since $am_1 = am_4$, this implies that $k_a\eta_1 = k_b\eta_4$ is a natural definition. The same applies to $am_2 = am_3 \Rightarrow k_b\eta_2$. Thus we have, after averaging over the large-scale roughness,

$$\langle P_a P_b \rangle_{iii} = \frac{k_a k_b L^4}{q_z^2 16\pi^2 R_0^4} \int_{-\infty}^{\infty} dp_1 \int_{-\infty}^{\infty} dp_3 \{\eta_1\}^2\{\eta_3\}^2 W(k_a\eta_1)W(k_b\eta_3) \times$$

$$\times \iint_{-L/2}^{L/2} dx_1 dx_3 e^{i2\Delta k \sin\theta(x_1 - x_3)} P_L\left(\frac{q_{x1}}{q_z}, + \frac{q_{x3}}{q_z}\ ; x_1\ , x_3\right) \quad ,$$

where q_{x1}/q_z and q_{x3}/q_z are the same as before, the surface slopes evaluated at x_1 and x_3 required for Bragg scatter.

This equation is identically the same as that at the top of page 41, except for the factor $e^{i\Delta k \sin\theta(x_1 - x_3)}$ in the integrand. The steps in the solution are thus identical to those previously. Thus we obtain the following result:

$$\langle P_a P_b \rangle_{iii} = \frac{k_a^2 k_b^2 L^4}{q_z^2 16\pi^2 R_0^4} \left\{\{\eta\}^4 W^2(k_0\eta)\right|_{s=0} \int_{-L/2}^{L/2} dx_1 \int_{-L/2}^{L/2} dx_3 e^{i2\Delta k(x_1 - x_3)\sin\theta}$$

$$+\left[\frac{d(\{\eta\}^2\ W(k_o\eta))}{ds}\right]_{s\ =\ 0} \int_{-L/2}^{L/2} dx_1 \int_{-L/2}^{L/2} dx_3 R_{SL}(\Delta x) e^{-i2\Delta k\Delta x\ \sin\ \theta} \quad , \qquad (44)$$

where $\Delta x \equiv x_3 - x_1$, and where we had used the fact that

$$\int_{-\infty}^{\infty}\int_{-\infty}^{\infty} ds_1 ds_3 s_1 s_3 P_L(s_1, s_3; x_1 x_3) = \langle s_1 s_3 \rangle = R_{SL}(\Delta x) \quad .$$

Carrying out the first two integrations, we obtain:

$$\int_{-L/2}^{L/2} dx_1 e^{i2\Delta k x_1\ \sin\ \theta} = L \cdot \frac{\sin\ (\Delta kL\ \sin\ \theta)}{(\Delta kL\ \sin\ \theta)} \quad .$$

The second term is the important one because it gives the desired slope spectrum of the large scale structure. We show this as follows:

$$\int_{-L/2}^{L/2} dx_3 \int_{-L/2\ +\ x_3}^{L/2\ +\ x_3} d(\Delta x)\ R_{SL}(\Delta x) e^{-i2\Delta k\Delta x\ \sin\ \theta} = \frac{L}{\pi} W_{SL}\ (2\Delta k\ \sin\ \theta)$$

Thus we obtain for Eq. (44)

$$\langle P_a P_b \rangle_{iii} = \frac{k_a^2 k_b^2 L^6}{q_z^2 \cdot 16\pi^2 R_o^4} \left\{\left[\frac{\sin\ (\Delta kL\ \sin\ \theta)}{\Delta kL\ \sin\ \theta}\right]^2 \{\eta\}^4\ W^2(k_o\eta)\Big|_{s\ =\ 0}\right.$$

$$\left. + \left[\frac{d(\{\eta\}^2\ W(k_o\eta))}{ds}\right]^2_{s\ =\ 0} \cdot \frac{1}{\pi L}\ W_s(2\Delta k\ \sin\ \theta)\right\} \quad . \qquad (45)$$

Thus, $\langle P_a P_b \rangle = \langle P_a P_b \rangle_i + \langle P_a P_b \rangle_{iii}$, where the first term comes from Eq. (42) and the second term comes from Eq. (45).

Variance of Scattered Power

We now take the variance of the scattered power about its mean, i.e., $\mathrm{Var}[P(\Delta k)] \equiv \langle P_a P_b \rangle - \langle P_a \rangle \langle P_b \rangle$, where the factors in the latter term are obtained from Eq. (38) by expanding $\{\eta\}^2 W(k_o \eta)$ in the same manner as done here. Then it turns out that $\langle P_a P_b \rangle_i = \langle P_a \rangle \langle P_b \rangle$ to the order of terms retained here.

Hence, $\mathrm{Var}[P(\Delta k)] = \langle P_a P_b \rangle_{iii}$, i.e.,

$$\mathrm{Var}[P(\Delta k)] = \frac{k_a^2 k_b^2 L^6}{q_z^2 16\pi^2 R_o^4} \left\{ \left[\frac{\sin(\Delta k L \sin\theta)}{\Delta k L \sin\theta} \right]^2 \left[\{\eta\}^2 W(k_o \eta) \right]_{s=0}^2 \right.$$

$$\left. + \left[\frac{d(\{\eta\}^2 W(k_o \eta))}{ds} \right]_{s=0}^2 \cdot \frac{1}{\pi L} W_{SL}(2\Delta k \sin\theta) \right\} . \qquad (46)$$

Interpretation

(a) The first term in Eq. (46) is merely the convolution of the range resolution cell on the surface, i.e., (L/2) sin θ, with the two-way separation wavenumber, 2Δk. Assumed here of course is that the illumination over the cell is uniform and zero outside. If the cell is pulse-limited, it means that the pulse is rectangular. If the cell is beam-limited, this means that the beam is uniform out to the three-decibel point and zero outside.

For realistic illumination functions across this cell, the (sin x)/x function will be replaced by the Fourier transform of the actual illumination pattern. With a properly tapered illumination function, the first term can be kept very small, so long as ΔkL is very large compared to unity.

A properly designed experiment would make the illumination pattern and L large enough (i.e., even approaching CW) so that the first term is negligible compared to the second in Eq. (46). Then Δk will be swept through the significant lower end of the gravity wave spectrum, i.e., Δk corresponding to Δf swept from about 2 MHz to 20 MHz, providing a sampling of the slopes of all gravity waves whose wavelengths vary between about 100 meters and 10 meters.

Derivations Required in Expansion in Phillips Saturation Region for Small-Scale Roughness

In order to quantitatively determine the magnitude of the factors appearing in (45) containing $\{\eta\}^2 W(k_o\eta)$ and its derivative, we must employ a model for W(p), the one-dimensional spatial height spectrum for the smaller-scale roughness. Since we plan on using a center frequency around 1 GHz, this means that $k_o\eta$ appearing as the argument of W is of the order of 15 m^{-1}; this in turn means that Bragg scattering is produced by ocean waves of the order of 30 cm - 1 meter long. Waves on the ocean of these lengths nearly always exist, and follow a Phillips-type spectral behavior because they are usually fully developed.

In two dimensions, the usual Phillips spectrum for saturated gravity waves is written as $W(p,q) = 4B/\pi(p^2 + q^2)^2$ for $p > 0$, $-\infty < q < \infty$.

To convert this to a one-dimensional spatial spectrum in p, we must integrate over q to obtain:

$$W(p) = \frac{B}{p^3} \tag{47}$$

for $p > 0$. The dimensionless constant B is found empirically to be approximately 0.005.

To evaluate the required factors at $s = 0$, we note the relationship between p, η, and s:

$$\eta = \frac{p}{k_o} = 2s \cos\theta - 2 \sin\theta \quad .$$

Then

$$\frac{\{\eta\}}{k_o} = \left[\sqrt{1 - (2s \cos\theta - \sin\theta)^2} + \cos\theta + s \sin\theta\right] \times \left[\cos\theta + s \sin\theta\right]$$

and

$$W(k_o\eta) = \frac{B}{8k_o^3} \left|s \cos\theta - \sin\theta\right|^{-3} \quad .$$

Using these quantities, the required factors, when evaluated at $s = 0$, become:

$$\{\eta\}^2 \, W(k_o \eta)\Big|_{s\,=\,0} = \frac{B \cos^4 \theta}{2k_o \sin^3 \theta} \quad , \quad \text{and} \tag{48}$$

$$\frac{d(\{\eta\}^2 \, W(k_o \eta))}{ds}\Big|_{s\,=\,0} = \frac{-\,B \cos^3 \theta}{2k_o \sin^4 \theta} (5 \sin^2 \theta - 3 \cos^2 \theta) \quad . \tag{49}$$

When these factors, evaluated in (48) and (49) above, are substituted into (45) for the variance of the scattered power, we obtain

$$\mathrm{Var}[P(\Delta k)] = \frac{k_a k_b L^6 B^2 \cot^6 \theta}{2^6 \pi^2 R_o^4} \left\{ \cos^2 \theta \left[\frac{\sin (\Delta k L \sin \theta)}{\Delta k L \sin \theta} \right]^2 + \right.$$

$$\left. + \frac{(5 \sin^2 \theta - 3 \cos^2 \theta)^2}{\pi L \sin^2 \theta} W_{SL}(2\Delta k \sin \theta) \right\} \quad . \tag{50}$$

Since it is the second term in Eq. (50) which contains the desired information about the large-scale gravity-wave slope spectrum, it is desirable to select θ, the incidence angle, such that the magnitude of the second term is enhanced. For horizontal polarization and backscatter, as considered here, a poor choice would be θ at or near 37.8° from the vertical, for this value makes $(5 \sin^2 \theta - 3 \cos^2 \theta)$ appearing in the second term identically zero. On the other hand, a value of θ near 60° will usually result in the second term being larger than the first term, for W_{SL} non-zero and near its saturation value. As mentioned previously, further reduction of the first term can be effected by better pulse shaping so that the $(\sin x)/x$ factor is replaced by one that falls off much more rapidly for large ΔkL.

IV PROPAGATION FACTORS LIMITING THE OPERATION OF AN HF ORBITAL SEA-STATE SENSOR

Introduction

Pertinent and perhaps crucial to the feasibility of an HF orbital sea-state sensor is the evaluation of those propagation factors which may limit its utility and thus undermine its competitive position vis-à-vis other techniques. The factors of interest are chiefly related to the transmission of high frequencies through the ionosphere. It happens that the most useful frequencies are also those most affected by the ionosphere. The principal factor which is likely to have a limiting effect is the opacity of the ionosphere to the lower part of the HF spectrum. Not so decisive, but still important, may be the excess transmission loss due to absorption. Other factors of importance may include noise, magnetoionic splitting and the resulting polarization rotation, and possibly, bandwidth and Doppler limitations. Clearly, an assessment of the effects of the above factors is essential at this stage of the study not only to the delineation of the sensor's capability but also the eventual choice of system parameters and operational modes.

In the following paragraphs the above propagation effects are examined in detail.

Minimum Penetration Frequencies

For the purpose of this discussion it is assumed that an orbital sensor is above the level of maximum ionization in the uppermost layer of the ionosphere, the F2 layer. Consequently, the transmission between the sensor and the surface will be largely controlled by the conditions existing in the F2 layer.

With this assumption, the task of predicting the minimum penetration frequencies is identical to that of predicting the F2 layer's critical frequencies. These can be related to the published predictions of the monthly median MUF (zero) F2. The latter parameters are published monthly by ITSA (Institute of Telecommunication Sciences) and made available as world maps for each even hour of Universal, or Greenwich Mean Time.[8] Using these maps, ionospheric predictions can be made for any time or geographic location of interest, and any ionospheric conditions as characterized, for instance, by the sunspot number.

To illustrate the procedure and to examine the ionospheric variation at different times in the seasonal and polar cycles, five graphs (Figures 12 through 16) have been prepared, showing the minimum vertical incidence penetration frequencies as a function of Local Mean Time. The geographic location chosen for this illustration is 50°N, 30°W, and corresponds to a position located in a rather heavily traveled route in the North Atlantic. The conditions are those predicted for the winter and summer of solar cycle 20 for both its minimum Sunspot number (SSN $\approx$ 17) and its maximum Sunspot number (SSN $\approx$ 106). Also shown is the prediction for the maximum of the earlier cycle (No. 19) in winter (SSN $\approx$ 180).

It should be noted that several conditions affect the use and interpretation of these curves. One is connected with the definition of MUF (zero) F2 which is really the maximum usable frequency at which an extraordinary wave can be reflected from the F2 layer. Thus, the lowest penetration frequency of interest to this discussion will, in general, be lower than MUF (zero) F2 by approximately one half the gyrofrequency at the location (and height) of interest. Typically, this adjustment is small (approximately .07 MHz). The second condition concerns the utilization of the predicted frequencies at angles of incidence other than the normal. In such instances, the penetration frequencies must be adjusted upward by being multiplied by the secant of the angle of interest. Thus, for a sensor which is programmed (or directed) to commence reception within ±25° from the vertical, this implies a 10 percent increase in the penetration frequency.

Returning to Figures 12 to 16, we note several characteristics associated with the F2 layer. A diurnal anomaly is exemplified by the diurnal asymmetry in the prediction graphs. The winter curves show some correlation with the solar elevation angle with the maximum occurring near noon of the Local Mean Time. In summer, that maximum occurs in the afternoon and is not very pronounced. In fact, near maximum conditions prevail most of the day. A seasonal anomaly, seen here because of the high latitude of our assumed observation point, is manifested by the fact that the penetration frequencies (for daytime) in winter exceed those predicted (and observed) in summer. For the conditions chosen in our illustration this appears to be true at both extremes of the solar cycle.

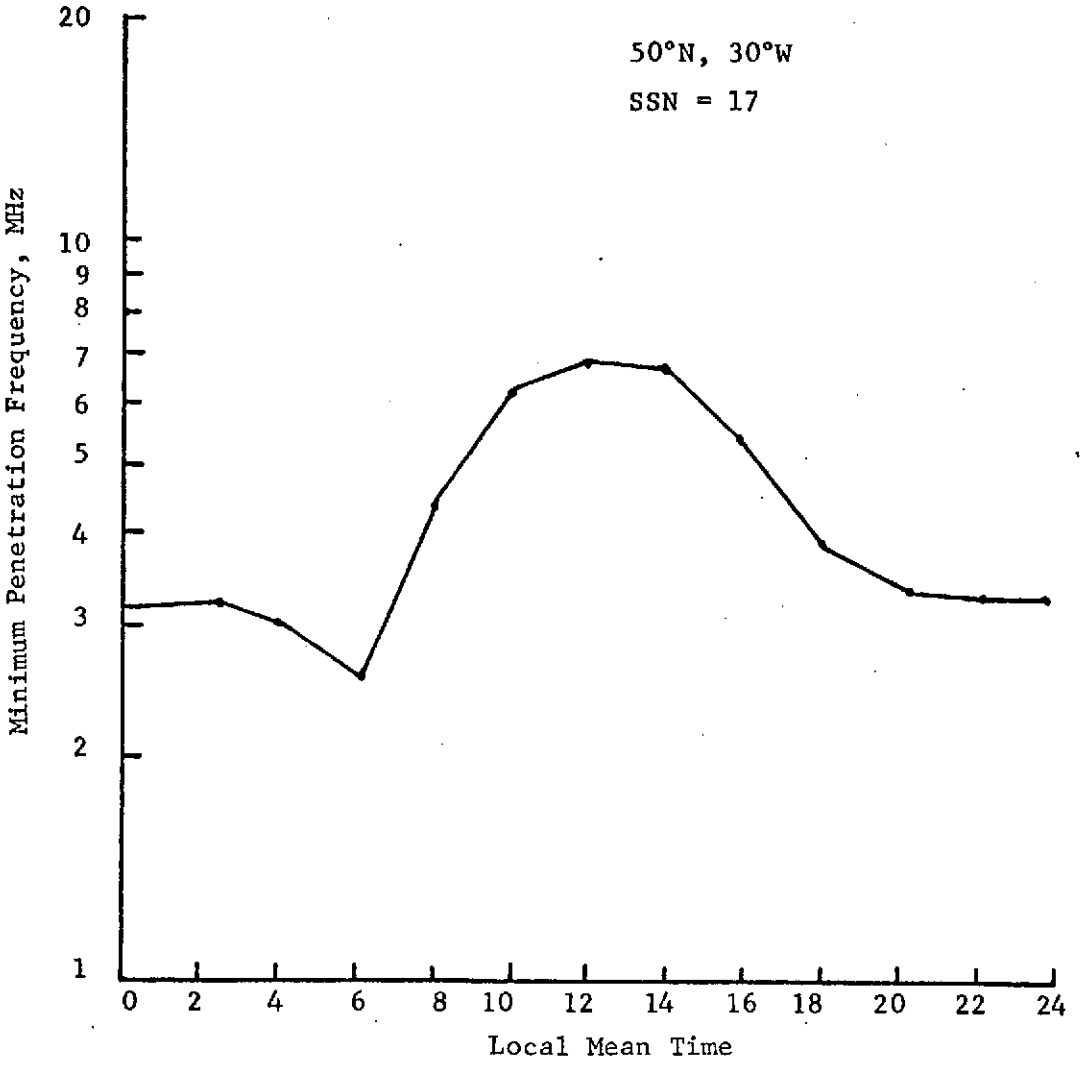

FIGURE 12. MINIMUM PENETRATION FREQUENCY VERSUS LOCAL MEAN TIME, WINTER

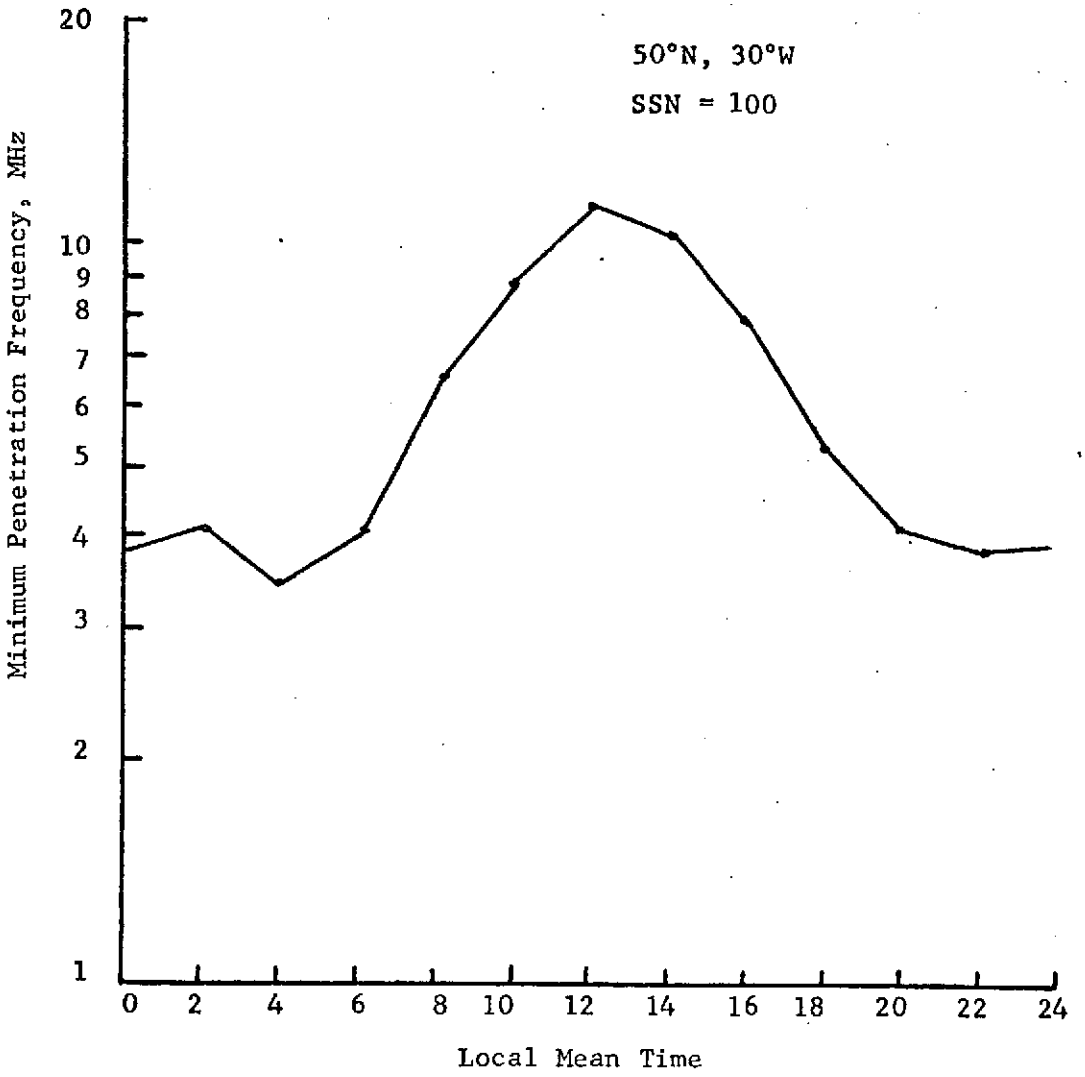

FIGURE 13. MINIMUM PENETRATION FREQUENCY VERSUS LOCAL MEAN TIME, WINTER

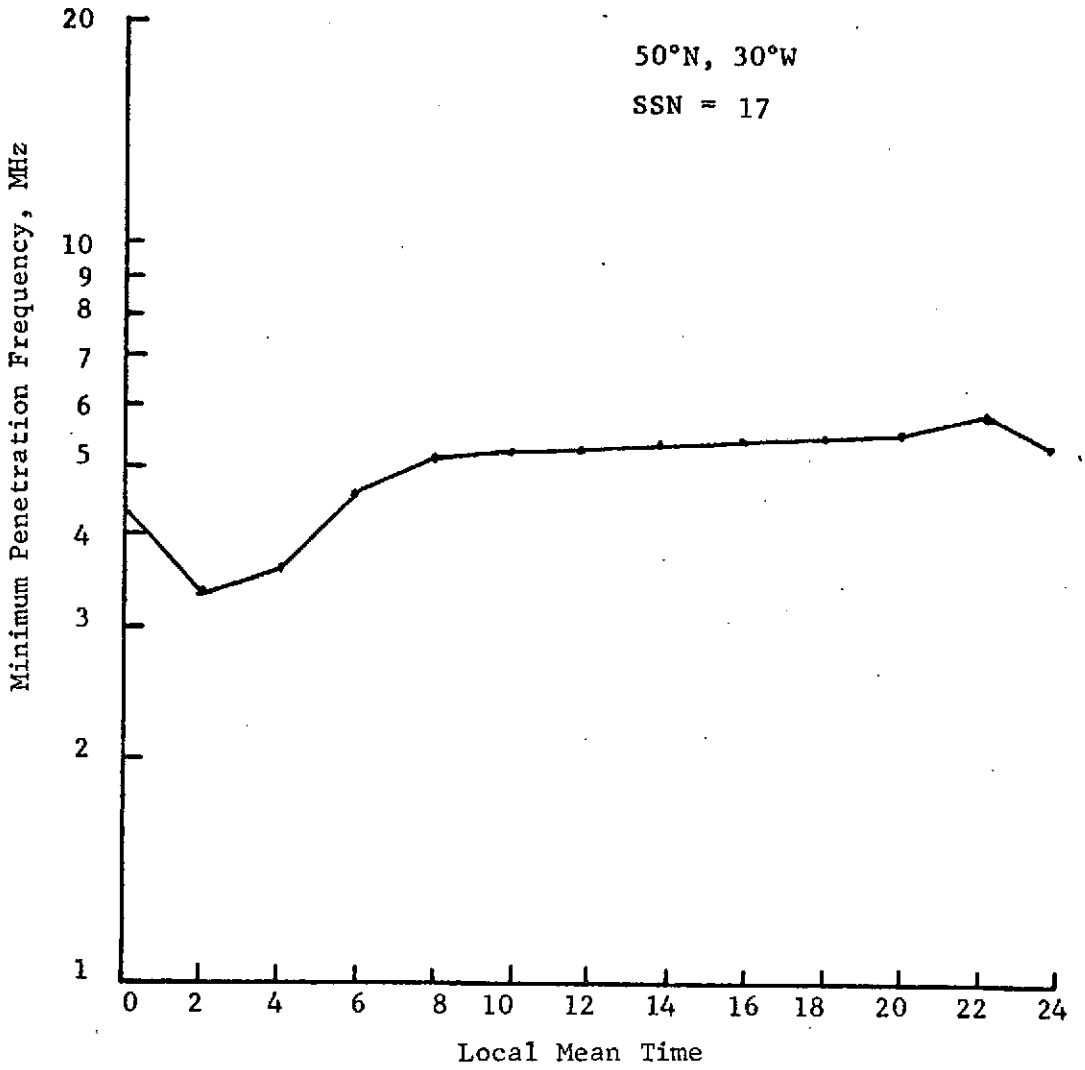

FIGURE 14. MINIMUM PENETRATION FREQUENCY VERSUS LOCAL MEAN TIME, SUMMER

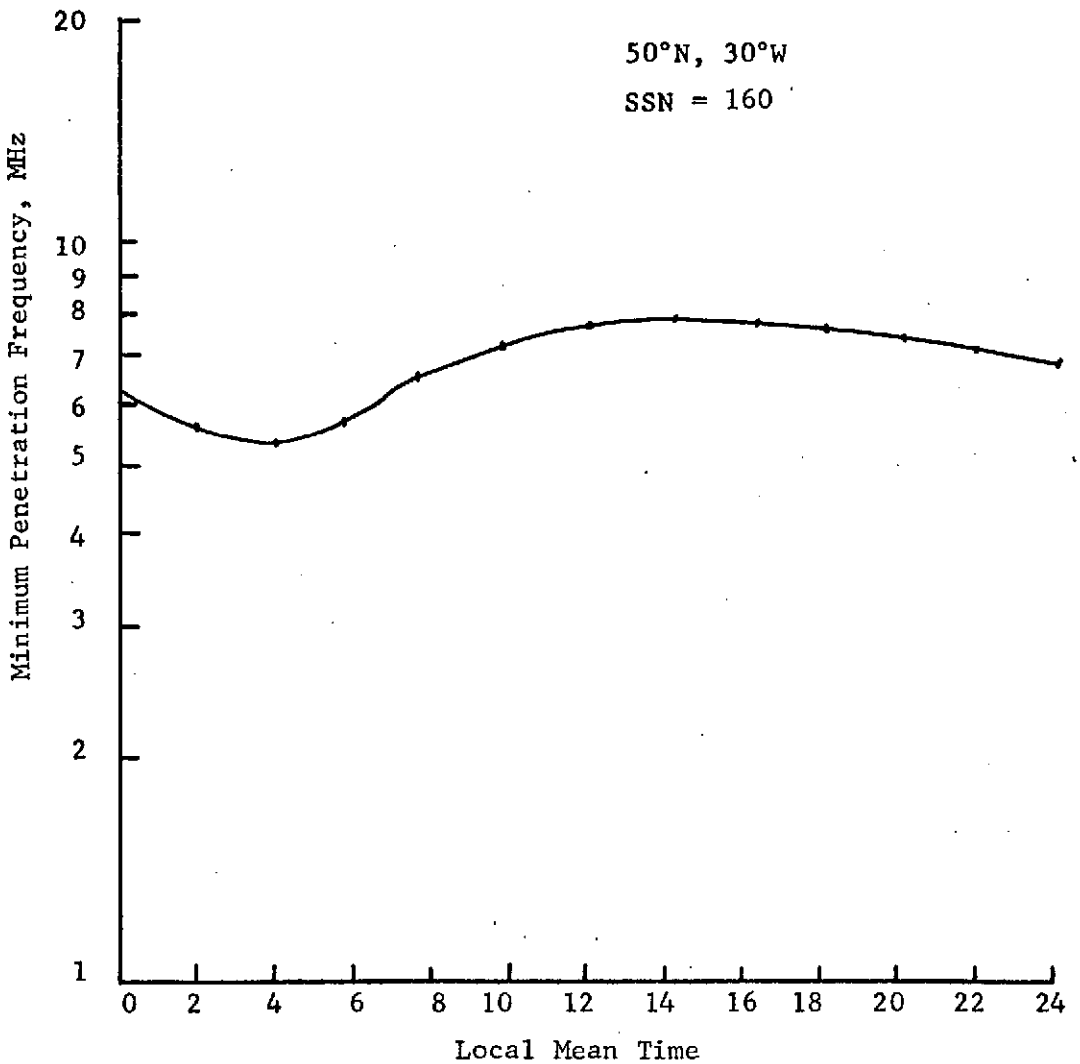

FIGURE 15. MINIMUM PENETRATION FREQUENCY VERSUS LOCAL MEAN TIME, SUMMER

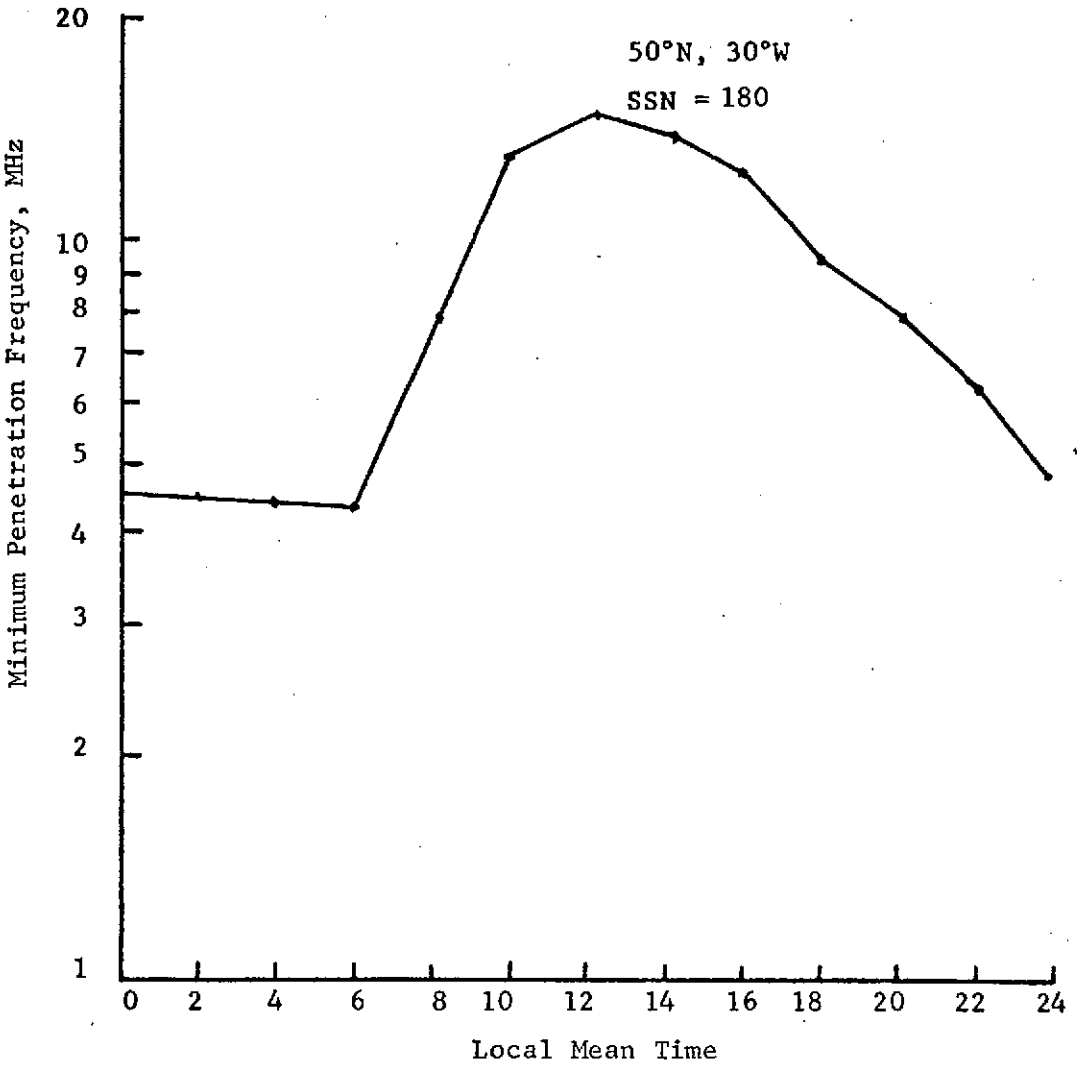

FIGURE 16. MINIMUM PENETRATION FREQUENCY VERSUS LOCAL MEAN TIME, WINTER

Our choice of SSN = 180 (winter = December) is not coincidental. Not only is the maximum SSN higher in that solar cycle (No. 19) but in December another anomalous behavior is observed in the F2 layer--the so-called December anomaly. Because of that anomaly (maximum seasonal ionization) and the high Sunspot number, the predictions of Figure 16 can be viewed as being representative of the worst propagation conditions which can be expected in the quiet ionosphere at the particular point of observation.

In the above discussion, we have not aimed at an extensive geographic coverage, but rather at a reasonably representative set of predictions. From these the following conclusions can be deduced:

(1) Propagation conditions favorable to the operation of the orbital sensor prevail, in a quiet ionosphere, generally at night between 0 and 6 hours local time. At such times transmission of frequencies as low as 5 MHz should be possible at the highest Sunspot numbers in both winter and summer.

(2) In periods of very low solar activity and in summer continuous transmission both day and night at frequencies as low as 6 MHz should be possible. In winter, transmissions of limited duration (0 to 8 hours) should be possible at frequencies as low as 3.5 MHz.

(3) Daytime transmissions, under 10 MHz, are possible throughout all seasons in periods of low and moderate solar activity; also, in summers in periods of high solar activity.

This discussion has not considered propagation conditions in the polar region or at times of geomagnetic storms. It is doubtful if the proposed approach would be useful in polar regions or at times of abnormal ionospheric conditions.

Absorption Loss

The absorption loss associated with the penetration of the ionosphere by an HF wave is related to the preceding discussion although quantitative analysis is, for a number of reasons, somewhat less tractable. The principal reasons for this are the scarcity of definitive measurements, the tentativeness of the available models and parameters used and, most important, the absence of computation routines comparable to that used in predicting critical frequencies.

The experimental data available consists largely of scattered measurements employing transmission from satellites or riometer measurements. Also available are several models using more or less (mostly less) realistic profiles of the ionosphere.

An estimate of the magnitude of the absorption loss can be made from measurements involving satellites.[9] It should be recognized, however, that the results obtained refer to a particular set of circumstances and that their extrapolation may present considerable difficulties. Fortunately, the circumstances of the available measurements represent conditions typical of the most severe ones to be encountered in the quiet ionosphere.

The most useful measurements available are those obtained with Sputnik I and II. The observational parameters were:

Frequency: 20 and 40 MHz

Time: October, November, 1957; 8 to 9 hours local time

Observation Point: 55° 42'N, 37° 18'E (approximate)

Height of satellite: 450 km+

Applicable SSN: ~ 200

Predicted MUF (zero) F2: 14 MHz at 8 hours LMT

The measurements made were of the received field strength; knowing the parameters of the systems, as well as the distance between the satellite and the ground station, the coefficient of absorption can be determined as

$$e^{-\Gamma} = E_x/E_o \quad , \tag{51}$$

where E_x = actually observed field strength and E_o = nonabsorbed, or free-space, field strength calculated from the system parameters. The value of Γ thus deduced for the point of nearest approach (estimated to be at about 450 km) is 1.35 or a total loss of approximately 12 dB. This is, we emphasize, an absorption loss associated with a daylight transmission. It is unfortunate that no nighttime estimates are available for it would certainly help with the process of extrapolation.

Just precisely how much can we say about the extrapolation of this loss to other circumstances? Suppose the observations were made at night, say, at 2 hours LMT, with all other parameters remaining as before. Suppose we observed the nighttime transmission at 5 MHz. Finally, suppose we repeated these measurements at the time when SSN is at its minimum, say, equal to 10.

To be truthful, none of the above questions can be answered with any degree of certainty without going through a rather complex modeling effort. For one, the above value of absorption loss can be almost entirely accounted for by the absorption in the F2 layer with the remainder of the ionosphere (D, E, and F1 layers) contributing less than 20 percent of the total. Whether a similar distribution of loss prevails at night is doubtful. It is also not certain how the contributions from various layers are distributed at different times during the solar epoch.

We can answer the posed questions at a risk of being tentative but, hopefully, not entirely wrong. For this purpose we assume that the observed absorption loss can be attributed to a single, well behaved layer for which, as long as the absorption is nondeviative, the absorption loss for a single transit is proportional to

$$(f_{cr}/f)^2 \tag{52}$$

where f_{cr} = critical frequency (approximately equal to MUF (zero) F2) and f is the operating frequency.

Thus, if during the night f_{cr} = 4.5 MHz, transmissions at 20 MHz would suffer an absorption loss of 1.22 dB; a transmission at 5 MHz would suffer a 19.5 dB loss. For SSN = 10, the critical frequency is $\approx$ 3 MHz, thus, above 5 MHz, transmissions at night would suffer a loss of about 8.7 dB. These last two values are, admittedly, rather high and perhaps unexpected. Unfortunately, sufficient data to verify these values are not currently available. For the time being we must conclude that the transmission loss, due to absorption, is not negligible especially at the lower penetration frequencies. It may not be imprudent to allow for as much as 15 dB absorption loss in the total loss budget.

It should be noted that all of the foregoing discussion has been restricted to conditions typical of a quiet ionosphere and it has also been assumed that we are dealing only with nondeviative absorption. For frequencies of interest to the sea-state sensor this is usually, but not always, true.

The HF Noise Environment

Another factor which must be considered in the process of evaluating the performance of an HF orbital sea-state sensor concerns the noise and interference levels in the immediate environment of the sensor. Together with the assessment of other environmental and system effects (absorption, polarization mismatch, etc.) the noise data are needed for the specification of such primary parameters as the transmitted power, waveform parameters, etc, to assure satisfactory performance of the sensor.

The unique mission of an orbital sea-state sensor requires a characterization of the noise environment at frequencies and in locations not normally utilized for communications. Consequently, noise and interference data for HF communications systems are not usable in our considerations. Neither are the data obtained at HF for ground-based sensors although it is useful background information and can be extrapolated to some extent.

It is evident that the most useful data will result from measurements which have been performed in circumstances nearly matching those anticipated for the HF sensor. To this end we have examined programs implementing orbital, top-side HF ionosondes. In what follows the available (and accessible) data are reviewed, and subsequently applied to calculations of the scattered power density at the sensor.

Measurements of HF noise both within and above the ionosphere have been performed in a program leading to the realization of top-side ionosondes, chiefly these concerned the Alouette I and II satellites although some other measurements were also performed by rocket probes.[10] In the case of the Alouette measurements these were conducted over an extended period of time in the frequency range from 1 to 15 MHz at altitudes of 500 to 3000 km. The receiver employed a 40 KHz bandwidth in conjunction with a half-wave dipole. These measurements disclosed the existence of several noise "bands" in the frequency spectrum each, tentatively, being attributed to a different generating mechanism. Briefly, these are as follows:

(1) Cosmic noise - Observed over the entire range of frequencies and characterized by a slow-varying intensity, generally some 30 dB above the receiver noise level.

(2) Ionospheric noise - Generally observed below the local hybrid frequency (roughly equal to the square root of the sum of squares of plasma and gyrofrequency) and thus, also below the penetration frequency, its level can exceed, at some frequencies, the receiver noise by as much as 80 dB. For obvious reasons this source of noise is of little consequence to the operation of the HF sensor.

(3) Solar noise - Generally submerged in the cosmic noise except in periods of solar activity; when observed, it is broad band and varies in intensity from the cosmic noise level to 30 or more dB above it. Occasionally, it can obliterate all other emissions, including strong interference from ground sources.

(4) Ground and Near-Ground noise - and man-made signals; these are observed, generally, above the penetration frequency although, occasionally, an anomalously propagated signal can be received below it. This noise originates from atmospheric storms, man-made devices and from ground-based HF communication circuits. Evidence exists pointing to a rather high level of these emissions (usually observed over land), exceeding, on occasion, the receiver threshold by as much as 90 dB.

Cosmic Noise Levels

Of the four noise bands identified only the cosmic noise and the ground emission are of interest to the present discussion. The solar noise, although quite high, is too sporadic to be used as a reference in the sensor's design.

For reasons which will be elaborated below, the cosmic noise emerges as the dominant source in the environment anticipated for an HF orbital sensor. A graph showing the cosmic noise spectrum obtained from the Alouette satellite and also including other measurements is shown in Figure 17.[10] Note that at the lowest frequency considered usable for the HF orbital sensor (f = 3.5 MHz) the cosmic noise temperature is of the order of $4 * 10^6$ °K.

Ground and Near-Ground Noise and Interferences

We have noted in the preceding section that the high level of noise and interference which is observed above the ionosphere at frequencies above the penetration frequency is chiefly attributed to ground and near-ground emissions. These include atmospheric noise, noise originating with man-made devices and installations, and the interference produced by ground-based, HF communication circuits. The available, satellite acquired data, does not allow conclusions as to the geographic distribution or diurnal and seasonal variations. Presumably, the high level quoted by Hartz was observed over densely populated land masses (say, North American continent) since neither Alouette I or II employed data storage facilities. Whether similarly high levels of ground noise would have been observed over the Indian Ocean, for example, is highly doubtful. It can be argued, that with the exception of transmitters located near the suborbital point and having reasonable antenna gains near the vertical, the interference from other communication circuits should be minimal. This is because such circuits, operating over oblique paths, will quite certainly employ frequencies much higher than those of the sensor. Of course, the above argument does not preclude interference from an anomalously propagated noise, whatever its source. The probability of occurrence of such interference, or its level, is however, difficult to assess.

The noise originating with atmospheric storms presents essentially a similar problem although its spectrum occupancy is broad band. Thanks to the concerted effort of organizations such as CCIR, adequate information on its level, distribution, and occurrence at the ground level is available. We know, for example, that local storms generally tend to occur in the afternoon hours over land masses;[11] seasonally, the storm centers tend to move northward during the northern hemisphere summer and vice versa. Therefore, the atmospheric radio noise is greatest during the local summer and least during the local winter. An example of atmospheric noise, together with other emissions, observed at

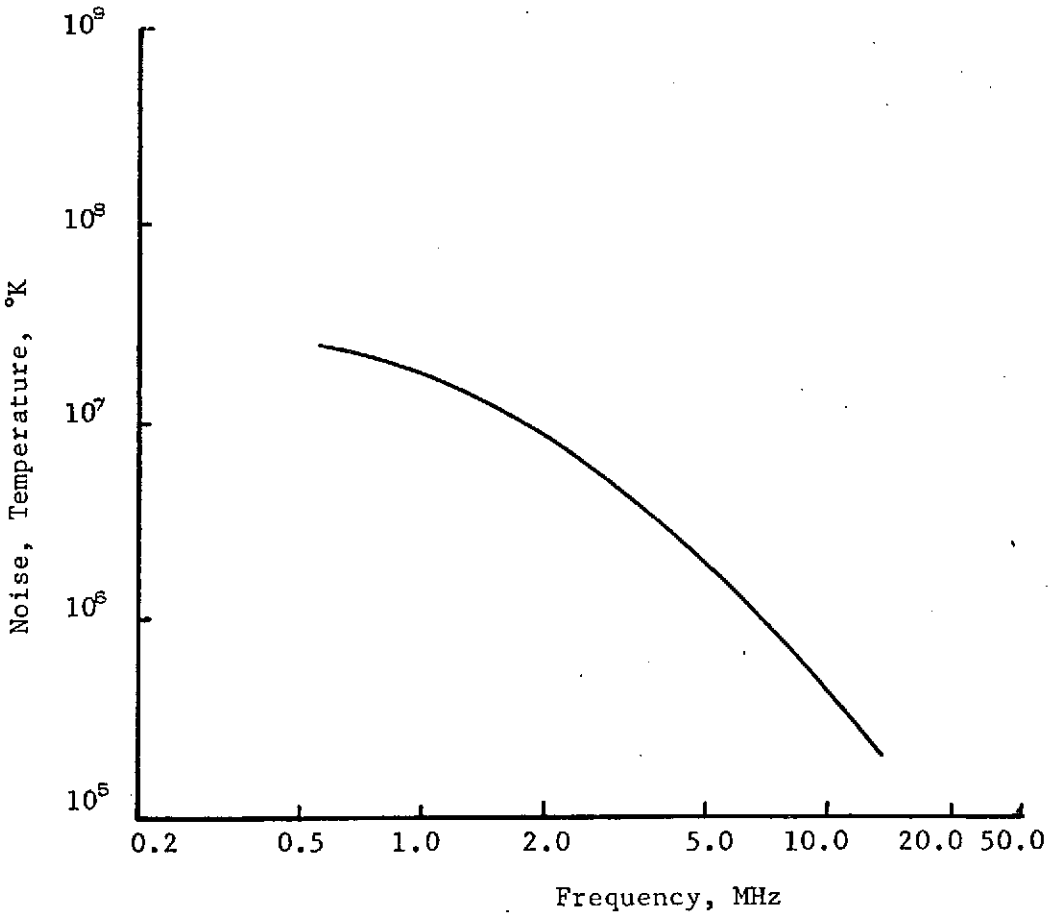

FIGURE 17. THE COSMIC NOISE SPECTRUM AS DETERMINED FROM THE ALOUETTE DATA AND OTHER MEASUREMENTS (After Hartz, 1969)

Washington, D.C., is shown in Figure 18. Such records are now available for virtually every location on the globe and are being continually updated.[12]

The value of such records to our discussion is that it demonstrates that even at the ground the cosmic noise can exceed both the man-made emissions and the atmospheric noise (at least in winter). For mid-ocean locations, this relationship is almost always true except near the equator. We should note, however, that such records do not, as a rule, include interference from active communication circuits.

It can be concluded, therefore, that the noise environment of an HF orbital sensor can be expected, with reasonable certainty, to be dominated by the cosmic noise, especially so at locations remote from the land masses and at frequencies close to the local penetration frequency. An occasional interference exceeding in intensity the cosmic noise level must be expected, its origin can be, as we have seen, either terrestrial or solar or both.

Ionospheric Doppler Effects

A radio signal scattered from the sea surface and subsequently propagated through the ionosphere will have imparted to it a Doppler frequency shift. The total Doppler shift on the received HF signal will consist of a number of components. A geometric shift due to the motion of the receiver, a shift due to the motion of the scattering surface, and a Doppler shift due to propagation through the ionosphere. The principal components of the ionospheric Doppler contribution arise because of the dispersive and time-variant characteristics of the ionosphere. Since the optical Doppler will be used to determine the directionality of the ocean surface spectrum, these additive components may constitute an error which must be estimated and perhaps corrected.

In the application of the HF orbital sensor, Doppler processing is essential for the complete recovery of the directional information from the sea surface. Thus, the effect of the ionosphere on the total Doppler shift must be examined. This is done in the following paragraphs assumming a spherically stratified ionosphere, transmission frequencies above the F2 penetration frequency and the gyrofrequency, and quasi-planar geometry.

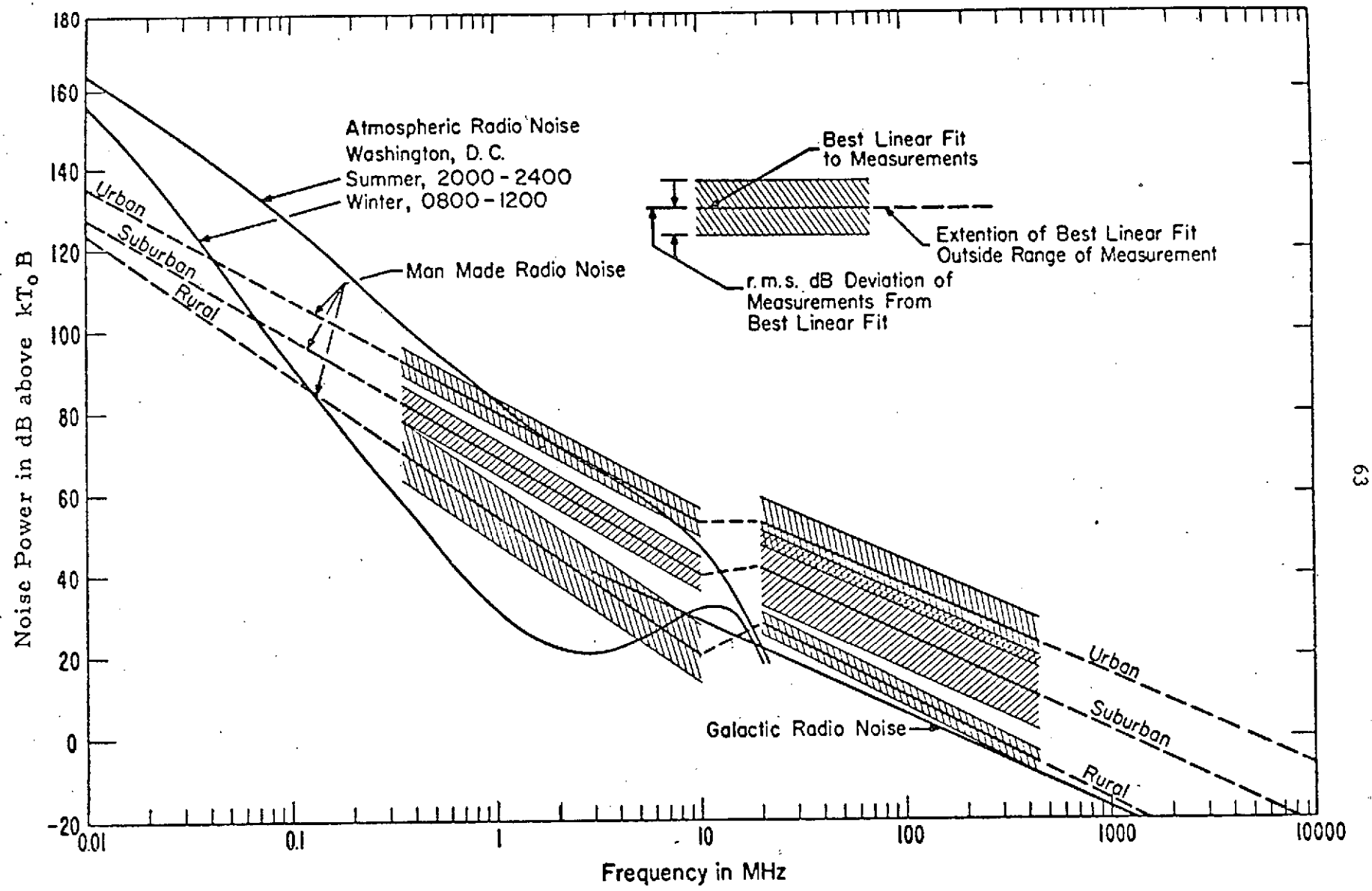

FIGURE 18. MEDIAN VALUES OF RADIO NOISE POWER AS RECORDED WITH A SHORT VERTICAL LOSSLESS ANTENNA

Basic Considerations of the Doppler Shift

The Doppler shift imparted to the radio signal by the ionosphere may be attributed to two mechanisms: (1) the time-variant nature of the medium as exemplified by its motion, local winds, and the consequent movement of "irregularities" sudden ionization, etc, and (2) the dispersive characteristics of the ionosphere which, when interposed between two terminals such as the orbiting satellite and a fixed location on the ground, leads to a time varying phase path and, thus, to a Doppler shift. Of the two mechanisms, the first is of primary interest for fixed, point-to-point communications between ground stations over ionospheric paths. The second mechanism is more dominant in space-to-ground circuits, although both of the mechanisms are operative.

Referring to Figures 19 and 20, consider a source, located in the ionosphere and emitting a radio signal of frequency ω; this signal when received upon its transit through the ionosphere will be proportional to

$$\sin (\omega t - \phi) = \sin \psi(t) \quad , \tag{53}$$

where ϕ is the phase retardation of the wave. This is given by

$$\phi = \frac{\omega}{c} \int_{R_o}^{R_o+h} \mu(\tau) \frac{d\tau}{\cos \zeta} \quad , \tag{54}$$

where $\mu(\tau)$ is the real part of the refractive index of the medium and ζ is the local angle defined by the path and radial directions. The instantaneous frequency of the received signal is

$$f = \frac{d\Psi}{d\tau} = \omega \left(1 - \frac{1}{c} \frac{d}{d\tau} \int_{R_o}^{R_o+h} \mu(\tau) \frac{d\tau}{\cos \zeta}\right) \quad . \tag{55}$$

It is clear from the above that for a stationary source and ionosphere, there will be no observable Doppler, although the wave arrival angle at the ground terminal will be, in general, affected by refraction.

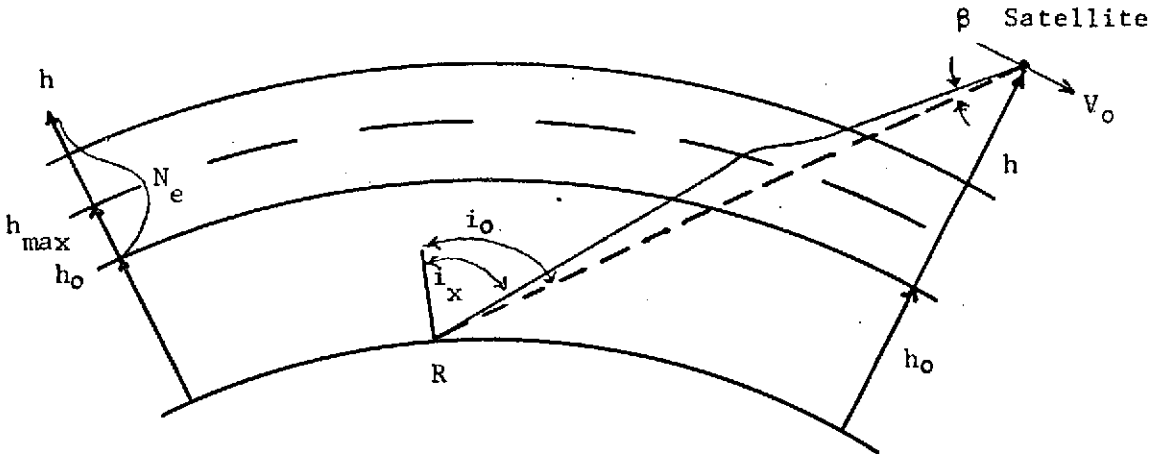

FIGURE 19. TYPICAL RAY PATH AND ELECTRON DISTRIBUTION IN THE IONOSPHERE

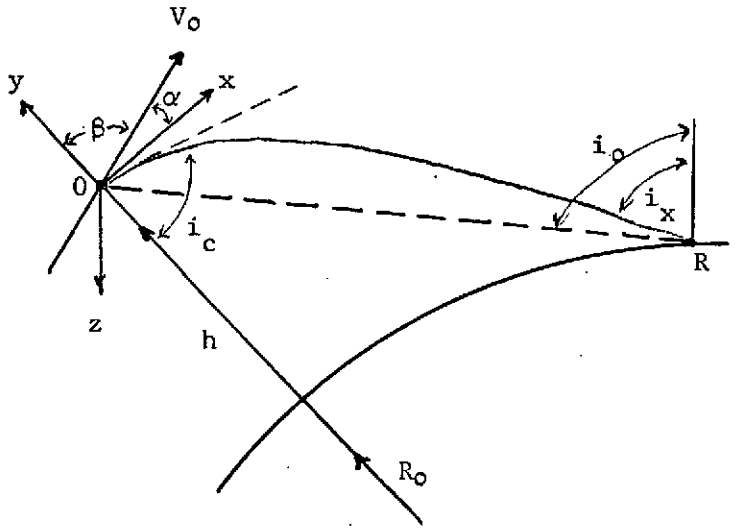

FIGURE 20. DERIVATION OF THE DOPPLER SHIFT IN A SPHERICALLY STRATIFIED IONOSPHERE

However, if the ionosphere is stationary, but the source is traveling at an orbital velocity V_o with the direction cosines of V_o as defined in Figure 2, we have for the component of $V\infty$ in the direction of the refracted wave,

$$V_d = V_o \ (\cos \alpha \sin i_c - \cos \beta \cos i_c) \quad . \tag{56}$$

Now the Doppler shift in a medium characterized by the index of refraction μ_c at the point of entry into the medium is

$$\Delta f = f \frac{V_d}{c/\mu_c} = f \frac{V_d}{\nu_c} \quad ,$$

where ν_c is the characteristic phase velocity of the medium.
Thus

$$\Delta f = f \ V_o \frac{\mu_c}{c} (\cos \alpha \sin i_c - \cos \beta \cos i_c). \tag{57}$$

For a spherically stratified ionosphere

$$\mu_c \ r \sin i_c = R_o \sin i_x,$$

where $r = R_o + h$, therefore

$$\Delta f = V_o \frac{f}{c} \left\{ \frac{R_o}{R_o+h} \cos \alpha \sin i_x - \cos \beta \sqrt{\mu_c^2 - \left(\frac{R_o}{R_o+h} \right)^2 \sin^2 i_x} \right\} . \tag{58}$$

Here i_x is final angle of arrival (or zenith angle) at the ground. Before proceeding with further simplications we note the two influences in the above expression for Δf. One is the influence of the local (i.e., immediate environment of the satellite) index of refraction μ_c; the other influence resides in the angle i_x which is the result of an integrated refraction over the entire path. For high altitude satellites the integrated influence predominates; furthermore, for a circular orbit at any altitude $\cos \beta = o$ and

$$\Delta f = V_o \frac{f}{c} \left(\frac{1}{1 + \frac{h}{R_o}} \right) \cos \alpha \sin i_x \ . \tag{59}$$

Thus, the calculation of Δf for this case is reduced to the calculation of the refractive effect. This can be done by, for example, by ray-tracing in the model ionosphere. For our purpose it will be sufficient to utilize the result of a simplified calculation[13] in which it is assumed that the transmitted frequency is above both the penetration and gyrofrequency, the effect of collisions are neglected, and $h \ll R_o$. For such an ionosphere

$$\sin i_x \approx \sin i_o \left\{ 1 - \frac{K}{f^2} \bar{N} \right\} \tag{60}$$

where

$$\bar{N} = \frac{1}{h} \int_o^h N dh \ .$$

Consequently, we have

$$\Delta f \approx V_o \frac{f}{c} \left(\frac{1}{1 + \frac{h}{R_o}} \right) \cos \alpha \sin i_o \left\{ 1 - \frac{K}{f^2 h} \int_o^h N dh \right\} \approx \Delta f_o + \Delta f_i \tag{61}$$

The first term of the above result is, of course, the geometric Doppler while the second term can be termed the ionospheric Doppler error. We note that the latter is inversely proportional to frequency and height and directly proportional to the sine of the zenith angle, velocity, and the integrated electron density.

It will be of interest also to note that the ratio

$$\frac{\Delta f_i}{\Delta f_o} = \frac{K}{f^2 h} \int_o^h N dh \ , \tag{62}$$

where

$$K = \frac{e^2}{8\pi^2 \varepsilon_o m} = 4.025 * 10^1 \text{ (MKS Units)} \ .$$

Some Experimental Results and Extrapolations

To estimate the magnitude of the ionospheric Doppler effect we now will examine some measurements which were previously discussed with respect to absorption loss estimates. The circumstances of these measurements were: Location - Moscow, USSR; Time - November, 1957, 8-9 hours, LT; Frequency - 20 MHz; Penetration frequency at the time of measurements - $f_oF2 \simeq 11.4$ MHz; Height of the satellite - $h \approx 500$ km. The electron distribution for which the calculated absorption loss best approximated the measured values was found by Kasautser[14] to follow the so-called biparabolic law with an exponential continuation from above the $3/2\ h_{max}$ level. For such a model the integrated electron density was $1.5 * 10^{17}$ electron/m^3. For this value and a height of 500 km, we have (at f = 20 MHz)

$$\frac{\Delta f_i}{\Delta f_o} = \frac{4.025 * 10^1}{5 * 10^5 * 4 * 10^{14}} * 1.5 * 10^{17} = .03. \qquad (63)$$

So far as the magnitude of Δf_i is concerned we can assume a typical zenith angle ($i_x = 25°$) and an orbital velocity ($V_o = 8 * 10^3$ m/sec). For $\alpha = 0$, then

$$\Delta f_i \simeq 5.9 \text{ Hz}.$$

Using the above ratio of 3 percent we see that the geometric Doppler for the above conditions was about 200 Hz.

We can compare these deductions with those of Lawrence and Little[15] who predict Δf_i equal, about to 4 Hz at a time of 15 seconds after zero crossing. Actual measurements performed under similar, but not identical, circumstances by Hibbard and Thomas[16] yield a value of about 8 Hz. We quote these values to verify the order of magnitude of our calculations. It is, however, impossible to ascertain all the important parameters of these measurements, such as time, f_oF2 or the altitude of the satellite.

If such information were available, an extrapolation of the Doppler shift would be quite possible. For example, in the ionospheric model employed by Harautser we have

$$\int_o^h Ndh \approx .96\, N_{max}\, h_{max} + 7 * 10^1\, N_{max} \left(1 - e^{-.008\, H}\right)$$

$$\approx N_{max} \left\{ .96\, h_{max} + 70 \left(1 - e^{-.008\, H}\right)\right.$$

where H = height of the satellite above the 3/2 h_{max} level and $h_{max} \approx 120$ km. If we assume that the form of the distribution is not affected by the solar cycle (which is not quite true) but only the value of N_{max}, then we can relate $\int_o^h Ndh$ to the measured or predicted value of f_oF2, since

$$f_{cr} = \sqrt{80.5\, N_{max}}$$

Consequently, we can write

$$\int_o^h Ndh \approx 1.24 * 10^{-2} f_{cr}^2 \left\{ .96\, N_{max} + 70 \left(1 - e^{-.008\, H}\right)\right\}. \qquad (64)$$

For the example calculated earlier we had $f_{cr} = 11.4$ MHz. Suppose that the measurements were performed at the time when $f_{cr} = 5$ MHz. The corresponding values of Δf_i would then have been

$$\Delta f_i \Big|_{5\ MHz} = f_i \Big|_{11.4\ MHz} \left(\frac{5}{11.4}\right)^2 \approx .193\, \Delta f_i \Big|_{11.4\ MHz}.$$

or approximately 1.13 Hz. This example illustrates, incidently, the distinct advantages of operating the orbital sensor in the night hours at which time the penetration frequencies, absorption, and Doppler ionospheric errors are low.

An Algorithm for an Adaptive Doppler Error Correction

Calculating the ionospheric Doppler error is not the only way through which correction of the measured Doppler can be effected. Obviously, measuring the ionospheric Doppler imposed on the direct signal from the transmitter would accomplish this task. However another scheme which appears to have, at least, the virtue of simplicity can also be devised to recover the geometric Doppler directly from the HF Doppler measurements. Consider the relation obtained earlier, now written as follows

$$\Delta f = \Delta f_o + \Delta f_i = f\left(\frac{\Delta f_o}{f}\right) - \frac{1}{f}(f\Delta f_i) = fD_o - \frac{1}{f}D_i \quad , \tag{65}$$

where now D_o, D_i are functions independent of frequency. Suppose we measure Δf at two closely spaced frequencies such that $f_2 = pf_1$ so that

$$\Delta f_1 = f_1 D_o - \frac{1}{f_1} D_i$$

$$\Delta f_2 = pf_1 D_o - \frac{1}{pf_1} D_i \quad . \tag{66}$$

By multiplying the second equation by p and subtracting the first from the second we have

$$(\Delta f_1)_o = f_1 D_o = \frac{p\Delta f_2 - \Delta f_1}{p^2 - 1} \tag{67}$$

Thus, measurement of the total Doppler at two related frequencies leads directly to the determination of the geometric component.

It is difficult, at this point, to speculate just how accurate this procedure would be and there seem to be no data, within reach, which would illuminate this question. Similarly, no obvious criterion has been found, thus far, for choosing the ratio of $f_2/f_1 = p$. Presumably, this criterion would be determined by our ability to measure the Doppler difference.

Faraday Rotation

When traversing the ionosphere, any linearly polarized wave will decompose into two elliptically polarized waves which traverse slightly different paths with different propagation velocities. As a result the plane of polarization of a linearly polarized wave will be rotated upon passage through the ionosphere. The amount of rotation is related to a weighted integral of the electron density distribution over the propagation path, or[17]

$$\Psi_{F_L} \approx \frac{K_L}{f^2} \int_a^b N_e \, B \cos\theta \, ds$$

$$\Psi_{F_T} \approx K_T \int_a^b N_e \, B^2 \sin^2\theta \, ds \quad , \tag{68}$$

where Ψ_F is the total angle of rotation, B is the magnetic field strength, N_e the electron density, and θ is the angle between the local magnetic field direction and the propagation direction. The specific expression Ψ_{F_L} or Ψ_{F_T} used depends upon whether the propagation is nearly along the magnetic field or transverse to it. For the HF frequencies of interest, the total angle of rotation may be hundreds of radians, thus the relationship between the polarization of the received signal at the satellite and the polarization at the ocean surface will not be known in general. This essentially precludes use of polarization information to obtain the directional spectrum for an HF orbital sensor.

V SYSTEMS CONSIDERATIONS AND REQUIREMENTS

Directional Spectrum Determination

For an HF orbital system the directional spectrum can be determined by the use of the observed Doppler at the satellite, or by the use of a transmitting antenna with horizontal directivity. At HF frequencies, particularly the lower frequencies, directional antennas tend to be somewhat large and limited in bandwidth. For a surface transmitter which is buoy mounted, for example, an antenna with horizontal directivity would not, in general, be feasible.

Thus, the signal Doppler appears to be the most feasible way of obtaining the directionality of the surface height spectrum. If ionospheric effects are neglected, the received Doppler has two components. One of these is the geometric or optical component due to the satellite's velocity. The other is due to the motion of the ocean waves and is given by Equation 2. Consider an omnidirectional transmitting antenna illuminating the ocean surface. A satellite-borne receiver is located at a height h and passes on a particular orbit so that at the closest point of approach the satellite is located at an angle θ from the transmitter zenith. The geometry of this situation is illustrated in Figure 21.

For a satellite at an altitude h, moving with a velocity V_o (assumed to be 8000 m/s) at an angle α with respect to the positive x-axis (assumed to lie in the mean wind direction) the geometric Doppler shift of a signal scattered from a surface area dA is

$$\Delta f = V_o \frac{fo}{c} \frac{\rho \cos(\varphi - \alpha) - h \sin\theta \cos(\varphi' - \alpha)}{\sqrt{h^2 + \rho^2 \cos^2\theta - 2\rho h \cos\theta \sin\theta \cos(\varphi' - \varphi)}} \tag{69}$$

The Doppler shift of the direct signal from the transmitter is

$$\Delta f = -V_o \frac{fo}{c} \sin\theta \cos(\varphi' - \alpha) \, . \tag{70}$$

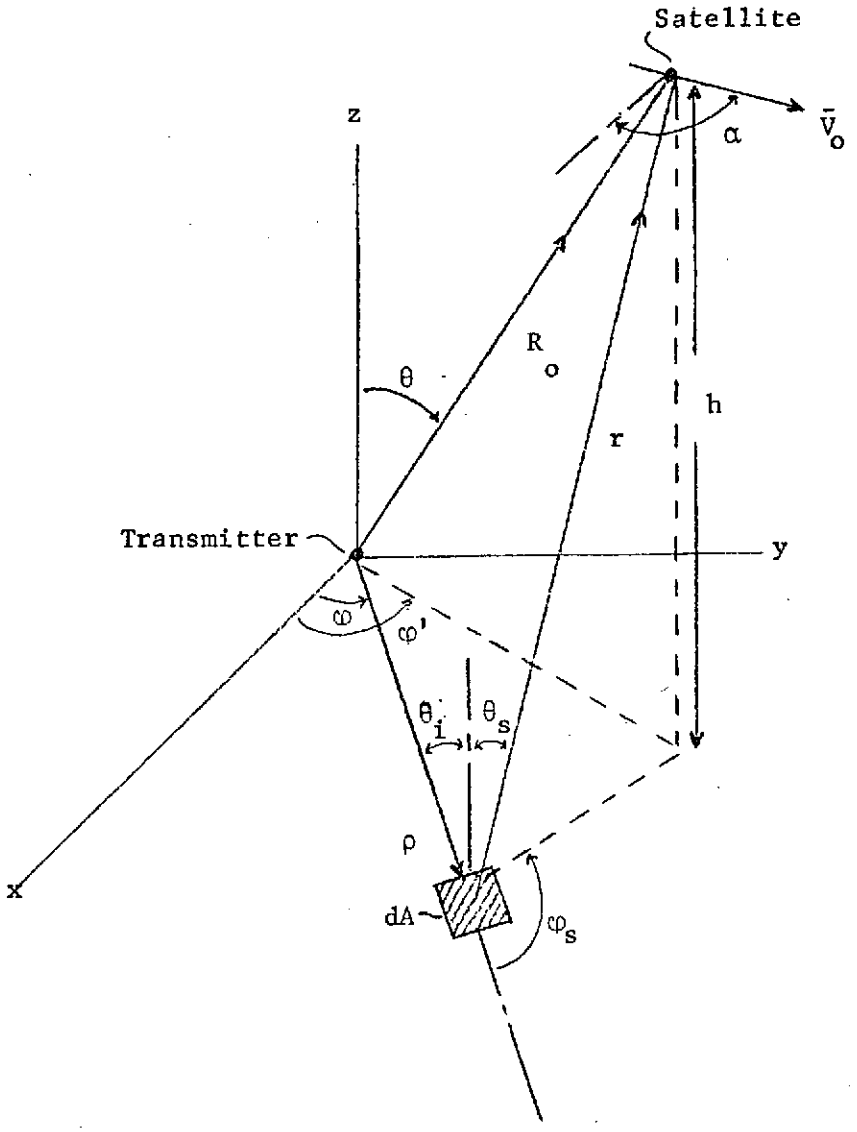

FIGURE 21. SYSTEM GEOMETRY

It is apparent from an examination of Equation 69 that for a scattering area located at a particular position in terms of ρ, φ a specific Doppler shift is imposed on the received signal.

To remove the effect of the radial distance ρ from the Doppler shift and obtain a quantity depending only on the azimuthal location of the scattering region φ we will examine the relationship between the total transit time for a signal scattered from a location ρ, φ and the transit time for the direct signal. The differential delay between the direct signal and the scattered signal is given by

$$\tau = \left(\frac{1}{c}\right) \left\{ \rho - (h/\cos\theta) + \sqrt{h^2 + \rho^2 \cos^2\theta - 2\rho h \cos\theta \sin\theta \cos(\varphi - \varphi')}/\cos\theta \right\} \qquad (71)$$

It should be noted that in these expressions (Equations 69, 71) a flat earth has been assumed. In actuality spherical earth geometry should be used. This was done during this study, however, for the range of parameters of interest the results differ negligibly from the flat earth case and the flat earth expressions are used for simplicity.

Equations 69 and 71 can be used to determine the relationship between the angular location of a scattering region and the Doppler shift, subject to the constraint that the received signal lies in a specific range cell, i.e. the differential delay τ is fixed. Given a value of φ and τ, Equation 71 can be solved for ρ and thus used with φ in Equation 69 to determine the Doppler shift.

These expressions can also be used to obtain constant Doppler and delay contours on the surface by fixing Δf and τ and solving for ρ and φ. A computer routine to do this was developed and Figure 22 illustrates the constant Doppler and delay contours for a satellite with h = 400 km, $\theta = 10°$, $\varphi' = 130°$, and $\alpha = 40°$. These particular parameters correspond to the satellite located at the closest point of approach.

From Figure 22 we see that at a specific delay and Doppler frequency there are two different angular locations which have the same Doppler shift. If the angular location on the surface is to be determined via the Doppler shift then this ambiquity must be resolved. This can be done in general by making

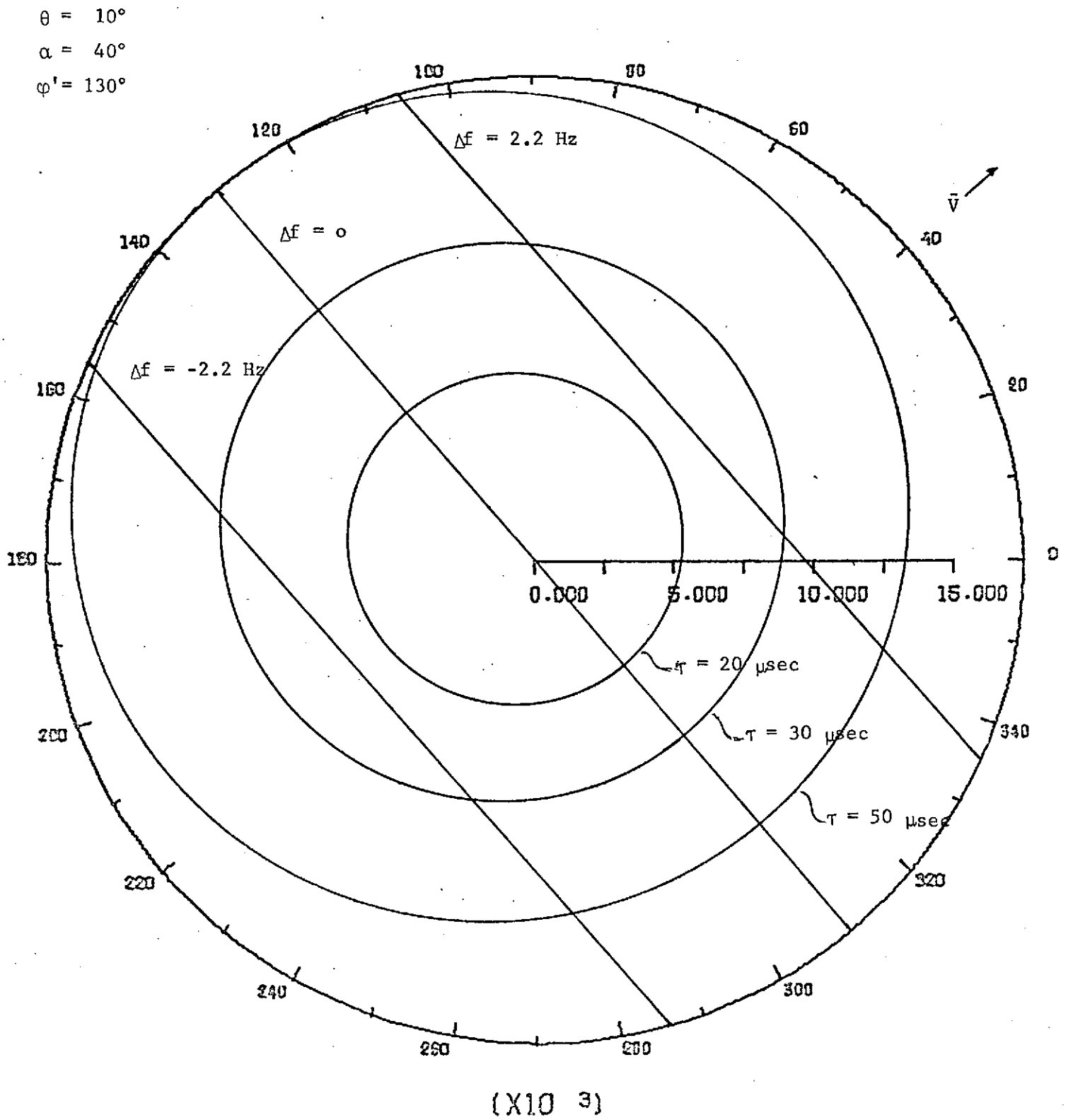

FIGURE 22. CONTOURS OF CONSTANT DELAY AND DOPPLER ON THE SURFACE AT THE POINT OF CLOSEST APPROACH

use of multiple range cells, or using similar information from another orbital location. With multiple range cells and the information derived from an entire pass considerable redundant information is obtained.

At the satellite receiver, the signal has a Doppler spread due to the cumulative effect of the scattering from the different regions of the ocean surface illuminated by the transmitter. The total integrated signal power contains information about the wave height spectrum at the incident wave number, while the directional information resides in the shape and relative intensity of the Doppler spectrum. This comes about due to the different regions of the surface contributing to different frequencies of the Doppler spectrum with an intensity which is determined by the ocean wave directionality at that point.

To determine the specific form of the received Doppler spectrum it is necessary to transform the expression for the received power at the satellite

$$dP_r = \frac{P_t G_t G_r \lambda_o^2 L}{(4\pi)^3 \rho^2 r^2} \sigma^o \rho d\rho d\varphi \tag{72}$$

from the ρ, φ coordinates to f, τ coordinates.
In the f, τ system

$$dP_r = \frac{P_t G_t G_r \lambda_o^2 L}{(4\pi)^3 \rho r^2} \sigma^o |J| \, d\tau df \quad , \tag{73}$$

where J is the Jacobian representing the transformation from the ρ, φ coordinates to the f, τ coordinates. The value of J is given by

$$J = \frac{\partial \rho}{\partial \tau} \frac{\partial \varphi}{\partial f} - \frac{\partial \rho}{\partial f} \frac{\partial \varphi}{\partial \tau} \tag{74}$$

The explicit value of J in terms of the geometric parameters can be obtained by evaluating the partial derivatives using Equations 69 and 71. The resulting expressions are very complex and will not be repeated here. These have been programmed, however, and in Figures 23 and 24 the unfolded Doppler frequency and the magnitude of J have been plotted versus the angular position on the

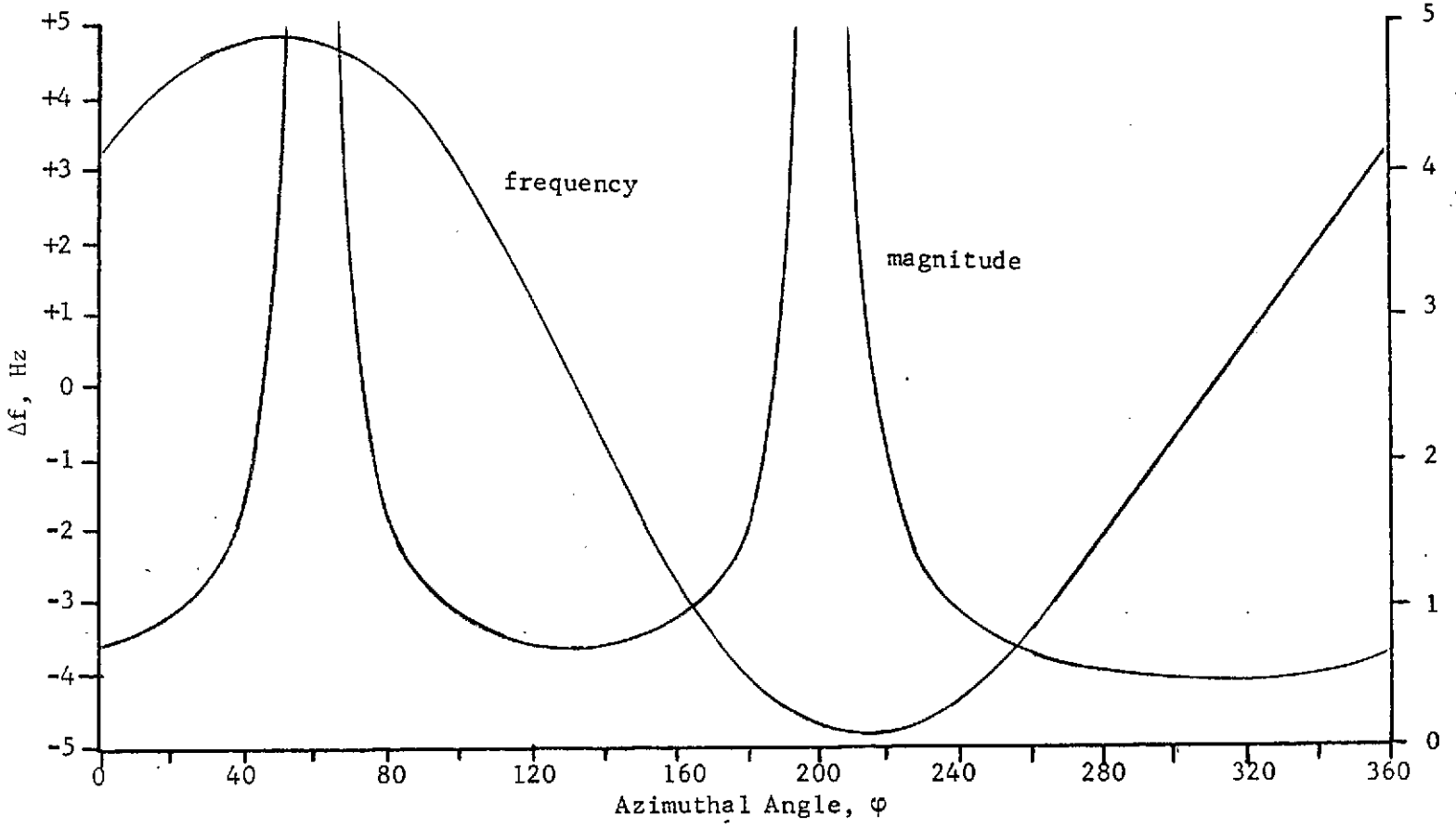

FIGURE 23. UNFOLDED DOPPLER SPECTRUM

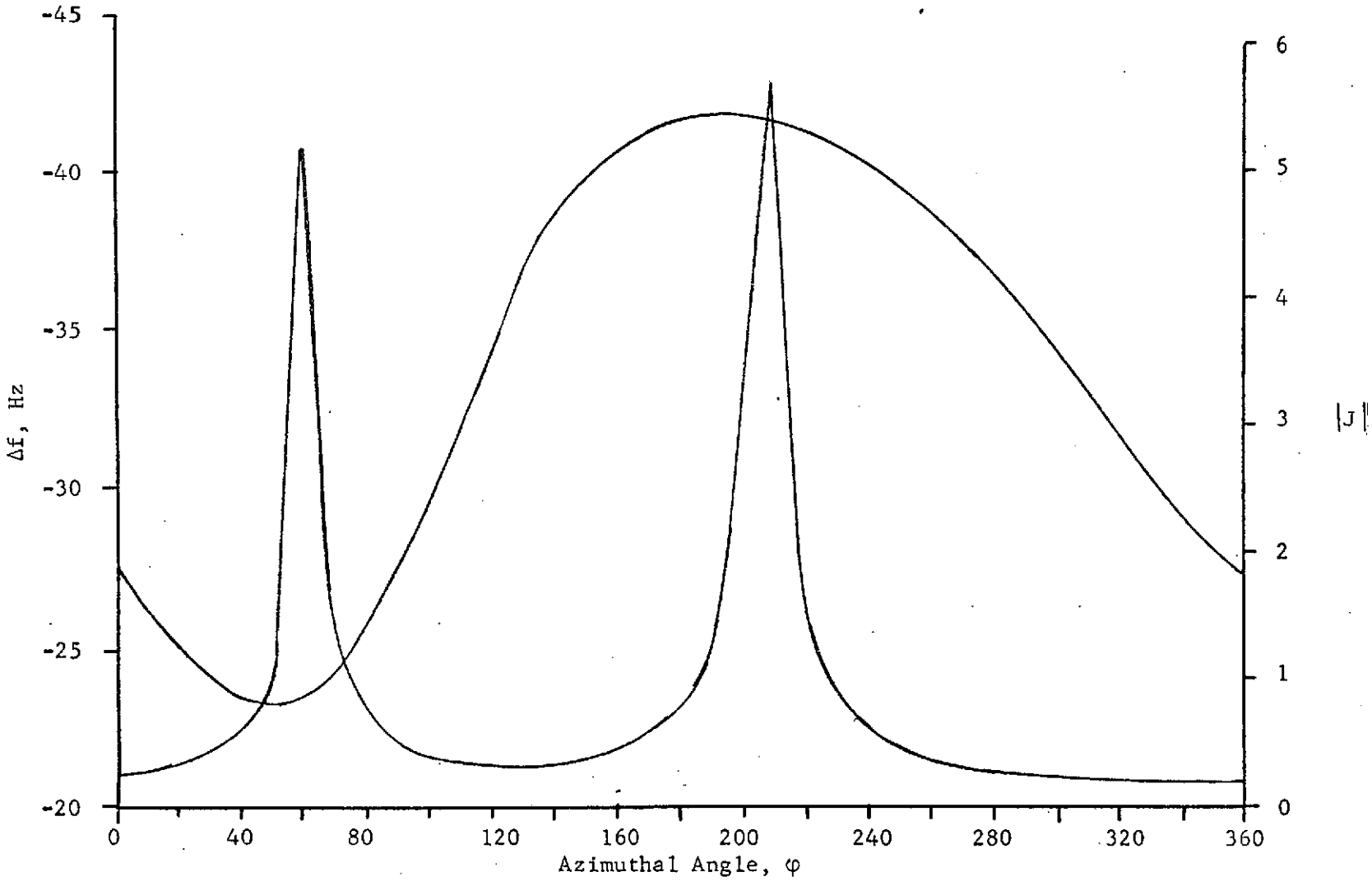

FIGURE 24. UNFOLDED DOPPLER SPECTRUM

surface for two different sets of conditions. One for $\theta = 10^{\circ}$, $\alpha = 40^{\circ}$, and $\varphi' = 130^{\circ}$ or CPA, and one for $\theta = 20^{\circ}$, $\alpha = 40^{\circ}$, and $\varphi' = 80$. Both of these figures correspond to a situation where all the surface regions are scattering with equal intensity or an isotropic wave height spectrum.

From these figures we see that the spectrum would peak at values near the maximum and minimum frequency excursions and drop to a lower value in the middle. The actual observed spectrum will be folded due to the angular ambiquity discussed earlier and will also be determined by the surface wave directionality and the scattering geometry. In Figures 25 and 26 curves are given of the actual Doppler spectrum that would be observed with a 1 Hz resolution for an isotropic wave height spectrum and a $\cos^2 \varphi$ wave height spectrum directionality. These curves were computed using a computer program in which all of the relevant effects have been incorporated. The satellite was located at $\theta = 10°$, $\varphi' = 120°$ for these curves with $\alpha = 40°$.

The expression used to compute these Doppler spectra was Equation 73 integrated with respect to τ over a 3 km range cell. The differences in the received Doppler spectrum resulting from the different directional dependences of the ocean wave height spectrum are quite apparent in Figures 25 and 26.

System Parameters

In order to determine the equipment configurations required for an HF orbital sea-state sensor we must know the required system parameters. One such parameter is the signal-to-noise ratio at the receiver. The total signal power power at the receiver is given by

$$P_r = \int_{f_1}^{f_2} \int_{\tau_1}^{\tau_2} \frac{P_t G_t G_r \lambda^2 L}{(4\pi)^3 \rho r^2} \sigma^o |J| \, d\tau df \quad , \tag{75}$$

The noise power as discussed in Section IV is due to cosmic noise and has a maximum effective noise temperature of $4 * 10^6$ °K. The noise power associated with this temperature is

$$N = KTB = 5.5 * 10^{-17} \quad \text{Watts/Hz} \tag{76}$$

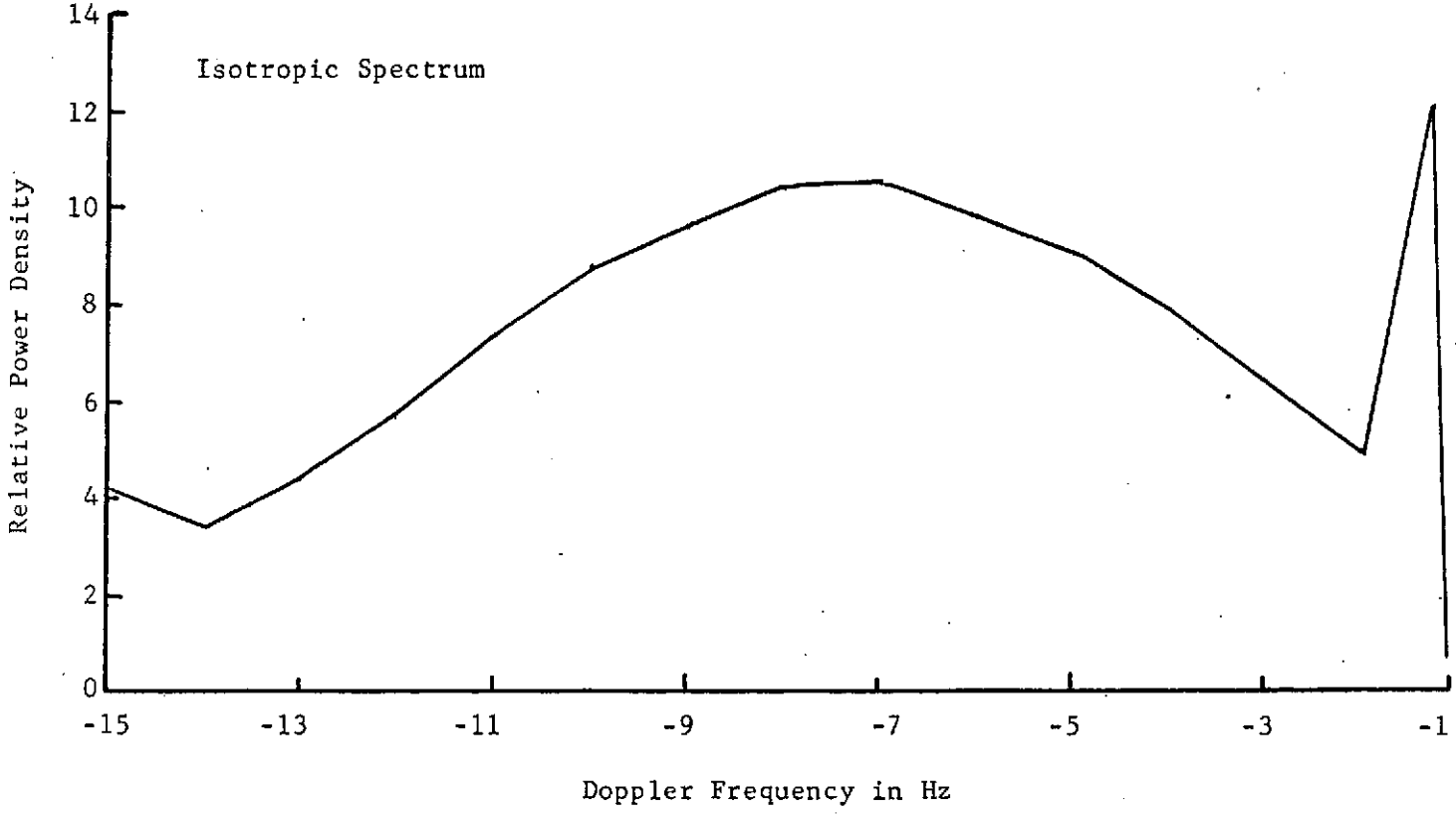

FIGURE 25. RECEIVED DOPPLER SPECTRUM FOR A SATELLITE WITH $\theta = 10°$, $\varphi' = 120°$, AND $\alpha = 40°$

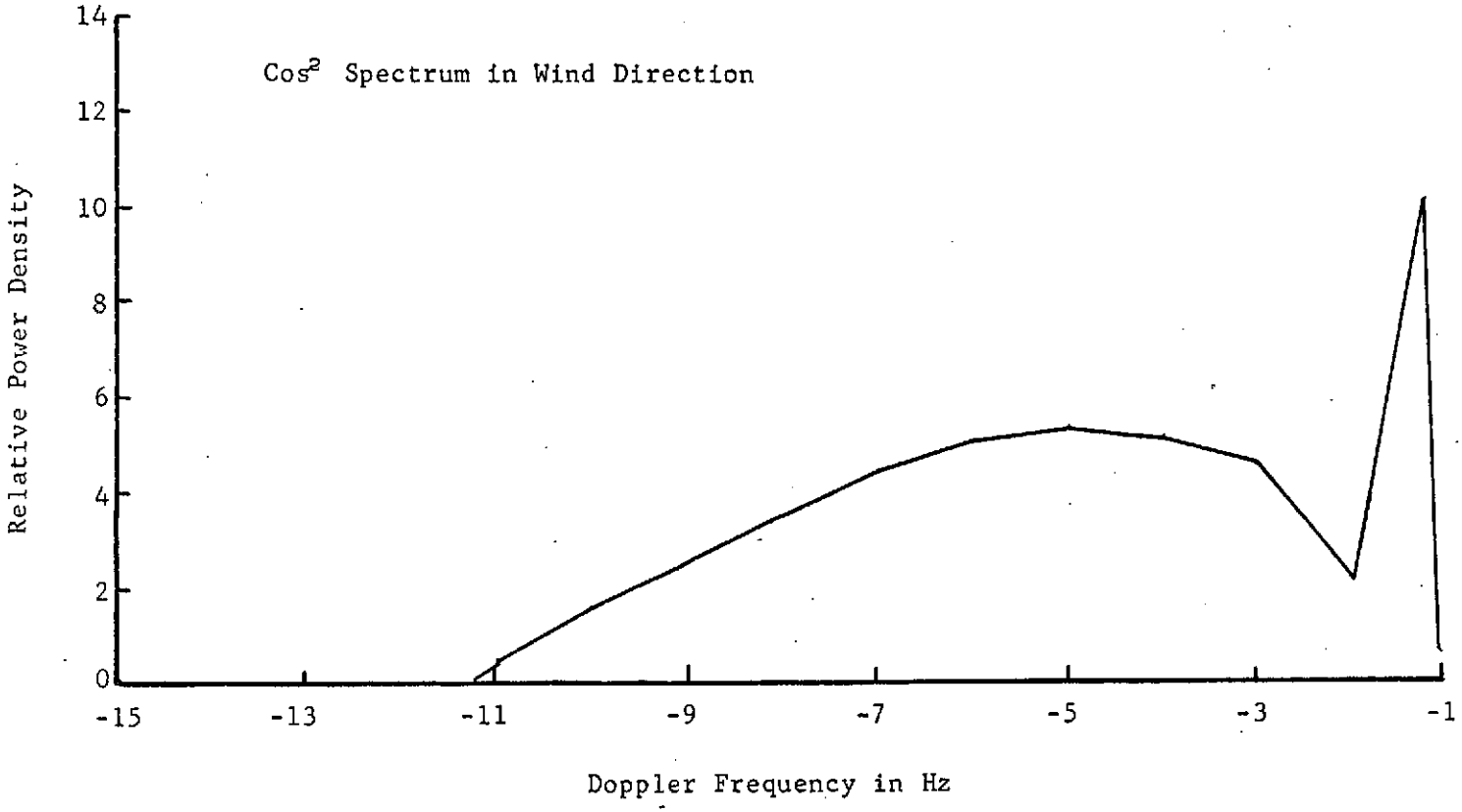

FIGURE 26. RECEIVED DOPPLER SPECTRUM FOR A SATELLITE WITH $\theta = 10°$, $\varphi' = 120°$, AND $\alpha = 40°$

The signal-to-noise ratio for a matched filter receiver is then

$$\frac{S}{N} = \frac{P_r}{N} = \int_{f_1}^{f_2} \int_{\tau_1}^{\tau_2} \frac{P_t G_t G_r \lambda^2 L T}{(4\pi)^3 \rho r^2 N} \sigma^o |J| \, d\tau df \quad , \tag{77}$$

where T is the coherent integration time.

In evaluating this expression the loss factor L should be broken into two parts

$$L = L_c + F_R \tag{78}$$

where L_c includes such factors as ionospheric absorption, mismatch loss, and other miscellaneous system losses. The specific value of L_c is of little consequence as long as an adequate signal-to-noise ratio exists. Since the losses appearing in L_c will affect both the direct and scattered signals the ratio of the two will be independent of these and accurately reflect the scattering properties of the surface.

The factor F_R is different, however. This factor is the excess loss above the free space value suffered by the incident field as it propagates as a ground wave from the transmitter to the scattering region on the surface. This loss is a function of the range of the scattering region from the transmitter, the frequency, and the surface properties, i.e., sea state. A detailed examination of HF ground wave propagation over a rough sea is presented in Reference 18. Figures 27 and 28, reproduced from that report, illustrate the effect of sea state on the ground wave loss. Since this loss is sea state dependent, and it must be either known or negligible in order to recover the surface wave height spectrum from the received signal, the surface area utilized must be confined. The maximum range should probably be confined to the order of 20 to 25 km in order that the variation in F_R with both frequency and sea state be less than 3 dB.

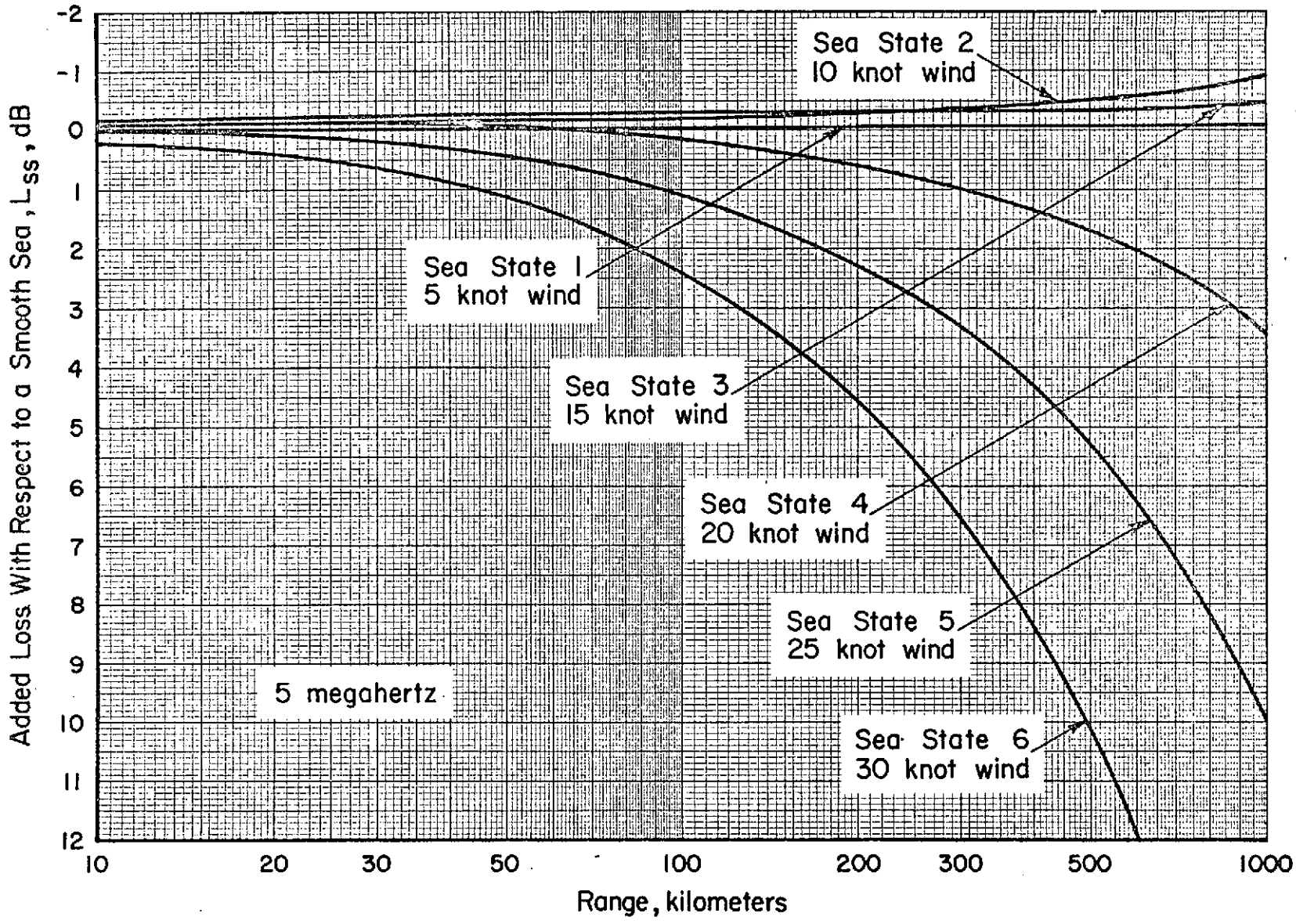

FIGURE 27. ADDED TRANSMISSION LOSS DUE TO SEA STATE AT 5 MHz. ANTENNAS ARE LOCATED JUST ABOVE SURFACE. NEUMANN-PIERSON OCEAN-WAVE SPECTRUM WITH PROPAGATION IN UPWIND-DOWNWIND DIRECTION.

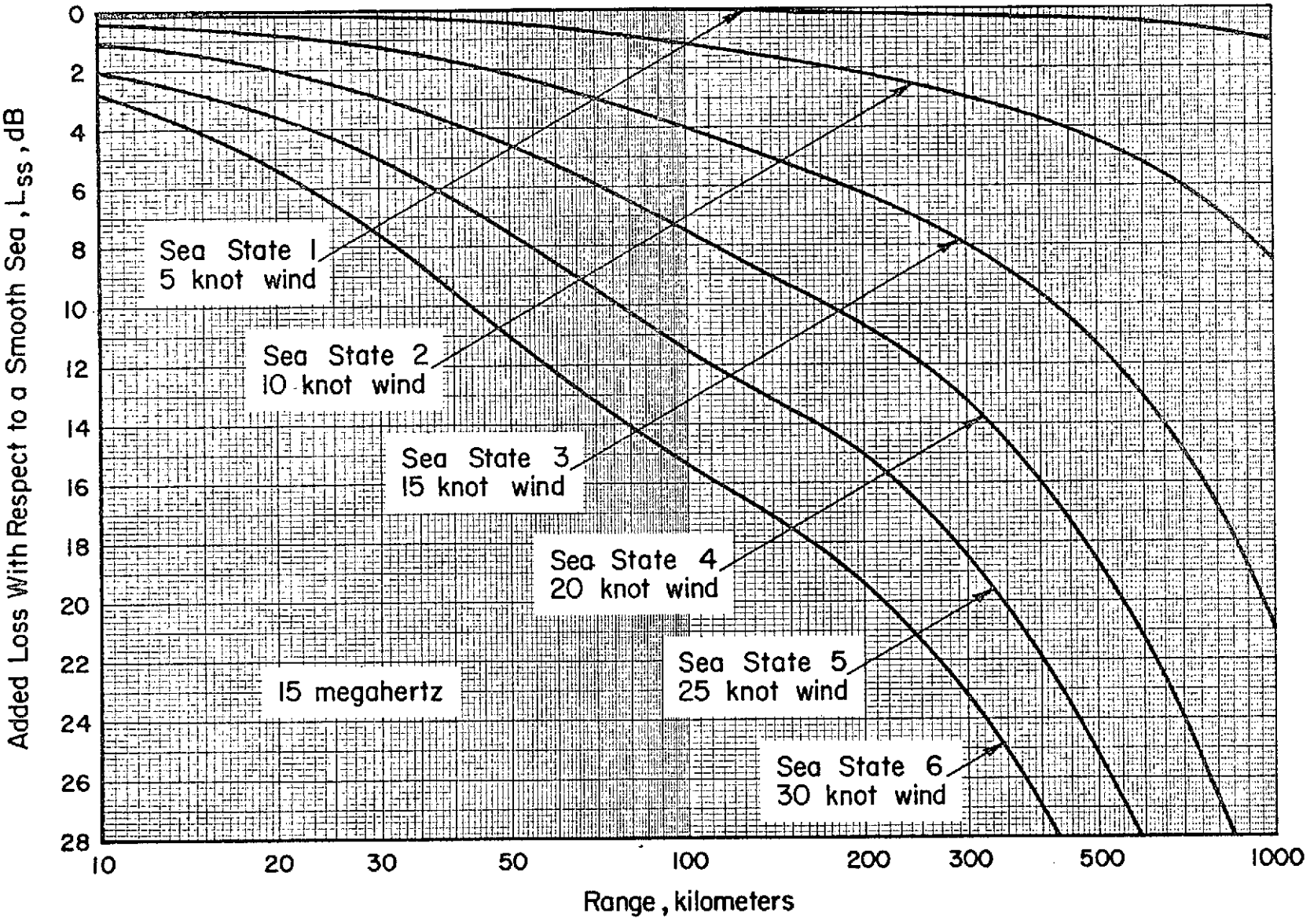

FIGURE 28. ADDED TRANSMISSION LOSS DUE TO SEA STATE AT 15 MHz. ANTENNAS ARE LOCATED JUST ABOVE SURFACE. NEUMANN-PIERSON OCEAN-WAVE SPECTRUM WITH PROPAGATION IN UPWIND-DOWNWIND DIRECTION

With this constraint on the maximum range and the value of F_R the signal-to-noise ratio has been computed for a 400 km orbit with a 10 watt average transmitter power output, a noise power of $5.4 * 10^{-17}$ watts/Hz, an integration time of .02 s, a 10 μs range cell, a total loss L of 20 dB, and a Pierson-Moskowitz isotropic wave height spectrum corresponding to a 20-knot wind velocity. For the purpose of this computation the antenna gains were assumed to be unity. The signal-to-noise ratio versus frequency for this case is illustrated in Figure 29.

The very sharp rise in the signal between 3 and 4 MHz is characteristic of the surface spectrum for this wind velocity as illustrated by Figure 5. By about 5 to 6 MHz we are in the saturation region and the slight decline in the SNR as the frequency increases is due to the λ^2 factor in Equation 77 and the frequency dependence of L. It should be noted that the noise power assumed was constant and not frequency dependent. In fact, it would tend to decrease with increasing frequency as illustrated in Figure 17, thus causing the SNR to generally increase slightly with frequency in contrast to the trend shown in Figure 29. The SNR values illustrated in Figure 29 indicate that 10 watts of average power are more than adequate for the system.

The choice of a 10 μs range cell is based on several criteria. As indicated previously, the maximum range of interest is of the order of 20 to 25 km. In order to Doppler process for the directional surface spectrum and solve the angular ambiquities, several range cells may be required within the 20 to 25 km limit. In addition, the direct signal must be isolated and be relatively uncontaminated by energy scattered from the immediate vicinity of the transmitter since it is required for reference purposes. All these constraints indicate that as narrow a range cell as practicable is desired. A further reason for this is the range/Doppler coupling indicated in Figure 22. If the range cell is too large, the angular resolution on the surface becomes limited by the range cell size rather than by the Doppler resolution available. These constraints indicate that a range cell of 10 to 20 μs is required. Narrower range cells would probably cause hardware difficulties, while larger cells would create several problems as discussed above.

The overall system parameters required of an HF orbital sea-state sensor are given in Table I. The specific hardware implementations of these parameters are discussed in the following section.

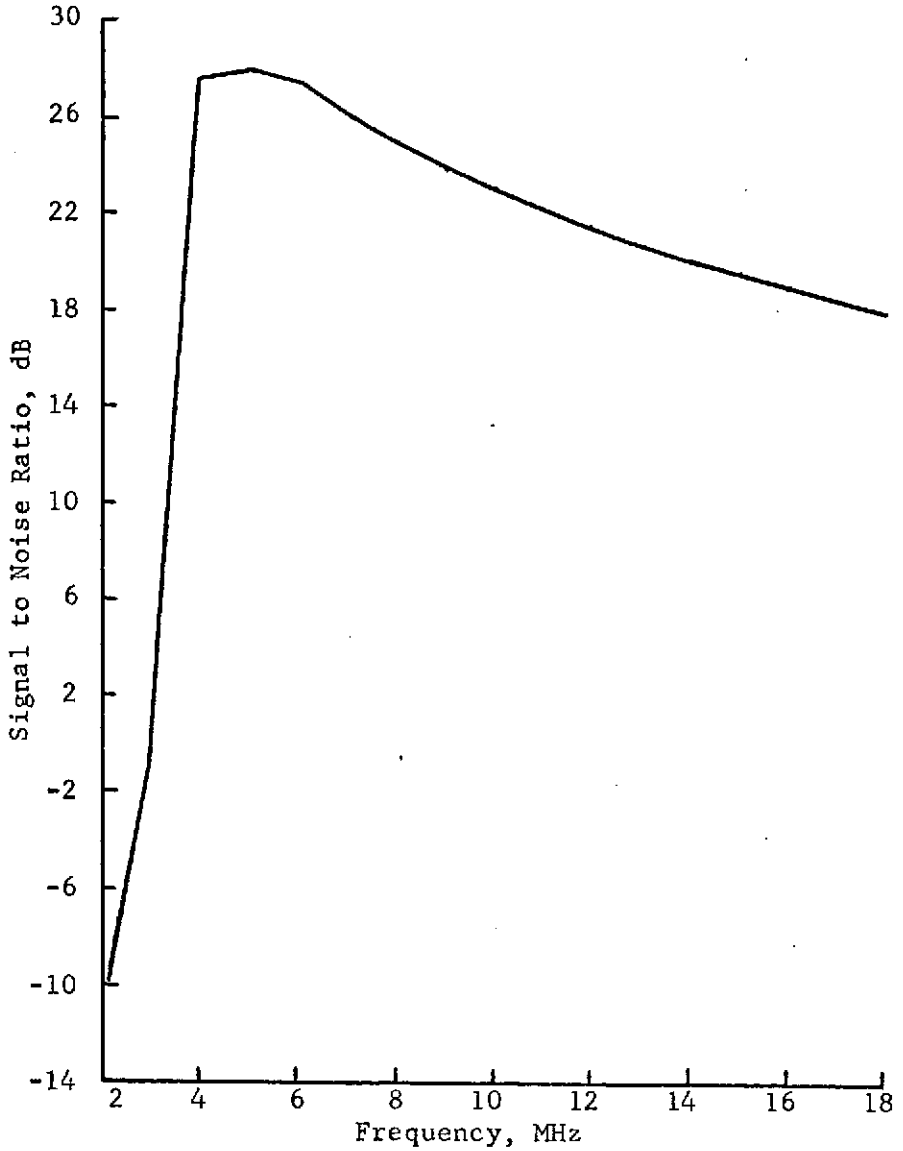

FIGURE 29. SIGNAL TO NOISE RATIO VERSUS FREQUENCY

TABLE I. SYSTEM PARAMETERS

Transmitter
Power Output - 10 watts average
Frequency - 3 to 30 MHz, switched in 1 to 2 MHz steps
Stability - 1 part in 10^8
Spectral width - <.5 Hz
Pulse width - 10 to 20 μs
Antenna - vertical polarization, azimuthally omnidirectional
PRF - 500 to 1000 pps
Receiver
Frequency - 3 to 30 MHz, switched in 1 to 2 MHz steps
Noise figure - not critical
Local oscillator stability - 1 part in 10^8
Time synchronization - not critical
IF bandwidth - 50 to 100 kHz
System bandwidth - 25 to 50 Hz
Coherent Integration Time - 1 s
Range Gates - 3 or more
Antenna - Horizontally polarized

Prior to discussing the hardware requirements, however, it is of interest to inquire about the effect of not being able to operate below about 3 MHz on the ability of the HF sensor to determine the RMS surface height for the higher sea states. The RMS surface height is obtained as indicated in Equation 16 by integrating the surface spectrum. This was done for cases where the lowest useful operating frequency was assumed to 1 MHz, 3 MHz, and 5 MHz, respectively. The results are presented in Table II, where the mean-square surface height estimates obtained with the Pierson-Moskowitz spectrum and various lower frequency limits are compared with the exact values for several wind velocities. The table clearly indicates that a lower frequency limit of 3-5 MHz is adequate for wind velocities up to 20 knots or sea state 4. For a 40 knot wind or sea state 8, even operation down to 1 MHz results in an error of a factor of 2.

TABLE II. MEAN SQUARE SURFACE HEIGHT ESTIMATES IN METERS FOR VARIOUS WIND VELOCITIES VERSUS THE LOWEST OPERATING FREQUENCY

Lowest Operating Frequency, MHz	5 knots	10 knots	20 knots	40 knots
0.0 (exact value)	.00137	.022	.352	5.63
1.0	.00137	.022	.350	2.39
3.0	.00137	.022	.301	.38
5.0	.00137	.022	.296	.139

Hardware Requirements

In order to satisfy the system parameters presented in Table I, several different hardware configurations might be used. The factor which influences the hardware configuration the most is the choice of waveform. If a single pulse-Doppler waveform is chosen, then a coherent transmitter capable of radiating a pulse train consisting of 10 to 20 μs pulses with an average power of the order of 10 watts is necessary. In order to reduce the peak power requirements, it is desirable to operate at a high pulse repetition rate or some form of pulse compression might be used. Both the transmitter and receiver must be synchronously stepped over the frequency range of 3 to 30 MHz, remaining at a particular frequency for at least one s in order that Doppler processing for a 1 Hz resolution can be accomplished. Resolution of this order would allow an angular resolution of about 10° on the ocean surface.

The transmitter stability should be of the order of 1 part in 10^8 in order to achieve the desired Doppler resolution. The receiver local oscillator stability must be of the same order.

From a hardware design standpoint it appears that the hardware required to implement a pulse-Doppler orbital system with the required parameters would not present any fundamental difficulties. The choice as to how much processing would be done on board the satellite and how much on the ground obviously cannot be made

now. It is probable that a command receiver would also be desired at the transmitter site in order to allow the transmitter to be activated only on command. This would be particularly true for a buoy-mounted transmitter.

Probably the most uncertain element with respect to the hardware configuration concerns the transmitting and receiving antennas. It is necessary that the transmitting antenna be vertically polarized, and a simple vertical whip will suffice. On the other hand, the resolution of the angular ambiguity associated with the use of the received signal Doppler for determination of the directional spectrum would be aided considerably if a directional transmitting antenna were available. A directivity pattern that would be useful would be the ability to illuminate one angular quadrant at a time, or even a figure eight type of pattern could be of use if switchable in orientation.

Two vertical monopoles can be used to obtain a figure eight type of pattern in the horizontal plane if phased properly. In order to change the orientation by 90°, however, a spacing of the order of one-half wavelength is required between the elements. At 3 MHz this corresponds to 50 meters, a rather large separation. If four elements are used, they can be spaced much closer and a switchable figure eight pattern obtained. The spacing in this case corresponds to about one-eighth of a wavelength or approximately 12 meters at 3 MHz. This is still too large for a buoy-mounted system, although it could be used on a ship. If several elements were used at the transmitter, either two or four, the phasing network would also have to be switched as the transmitter frequency is changed.

The receiving antenna must be horizontally polarized. The simplest receiving antenna appears to be a long horizontal wire. No specific attention has been given to the achievement of this for a satellite receiver, although it is appreciated that it might present some difficulty.

An Aircraft Experiment

In order to validate the concepts presented here and further define the hardware configuration required for an operational HF bistatic sea state monitor, an aircraft experiment should be carried out. During this experiment an aircraft-borne receiver should be utilized with a transmitter located on a ship to measure the directional surface spectrum in an area which is also instrumented with wave spars or other conventional instrumentation for wave height measurements.

C-2

Such an experiment will not only verify the concept and aid in defining the required satellite hardware but will allow the system and hardware requirements to be determined for the use of the HF bistatic technique as an aircraft-borne ground truth measurement system. In fact, it is the only system currently known which may be capable of measuring the full directional spectrum relatively easily and at relatively low cost. One can envision a system in which the aircraft drops a relatively low-cost buoy containing the transmitter and then by flying on a straight-line path near the buoy location obtains the full directional wave height spectrum in the vicinity of the buoy.

For a satellite-borne HF bistatic sea state sensor the orbital motion of the satellite and the resultant Doppler shift imposed on the scattered signal can be used in conjunction with range resolution to determine the directional dependence of the ocean surface spectrum. Doppler spreads of as much as 40 to 50 Hz can result, and Doppler processing to provide a 1 Hz resolution would allow the surface spectrum directionality to be obtained with approximately a 10° resolution. For a typical aircraft-borne receiver, however, the Doppler spread would typically be of the order of 0.5 to 0.7 Hz. Thus, to achieve the same surface resolution would require Doppler processing to a resolution of 0.01 to 0.02 Hz. Doppler processing to this order, although possible, would present some problems and will complicate the experimental equipment requirements. On the other hand no ionospheric limitations will exist for an aircraft-borne system.

It would be desirable to utilize a coherent waveform and carry out Doppler processing, if possible. This would allow the unambiguous directional spectrum to be obtained and would validate the concept of using the signal Doppler for obtaining the directional spectrum. In addition, if the direct signal is available, such factors as variations in the transmitter power output and the transmitting and receiving antenna gains with operating frequency can be removed by referencing the scattered signal level to the direct signal level. If the direct signal is not available, these factors must be initially measured in order that the measured scattered signal levels can subsequently be corrected.

For a coherent pulse-Doppler airborne system, the equipment requirements are essentially the same as in the satellite case, except that Doppler resolutions of the order of 0.01 to 0.02 Hz are required for the same angular resolution. This means that coherent integration times of the order of 50 to 100 s would be necessary with transmitter and local oscillator stabilities of the order of one part in 10^{10}

over periods of the order of 50 to 100 s. The basic spectral line widths of the transmitter and local oscillator should be less than 0.01 Hz. Purely from a hardware standpoint, these requirements are attainable, and a pulse-Doppler waveform could be used for the aircraft experiment. One problem that would be encountered with Doppler resolutions of the order of 0.01 to 0.02 Hz would be spreading due to fluctuations in the aircraft's velocity. This may limit the attainable Doppler resolution to about 0.05 Hz and the subsequent angular resolution to approximately 36°, assuming a maximum 10 percent velocity fluctuation.

Although a pulse-Doppler approach as suggested for a satellite system appears feasible for an aircraft experiment, some thought has also been given to the use of a coherent FMCW waveform which would provide both range and Doppler resolution. Such a waveform appears to have some advantages over the pulse-Doppler with respect to hardware simplifications. It also appears to be somewhat more flexible and more immune to interference. Such a system is relatively simple, in that the transmitter radiates a coherent waveform which is swept over intervals of 50 to 100 kHz at a basic sweep rate of perhaps a MHz, thus providing 10 sweeps per s. The frequency versus time waveform is essentially a sawtooth in shape. At the receiver the receiver local oscillator is synchronously swept over the same frequency interval at the same rate, except that the sweep starting points are delayed in time by an amount corresponding to the range delay between the transmitter and receiver. The receiver local oscillator is also offset by a fixed amount corresponding to a desired IF frequency. This would nominally be somewhere in the HF band so that a conventional communications receiver could be used as the IF amplifier. The scattered signal, after mixing with the receiver local oscillator, then has a spectral spread which corresponds to different ranges. At the receiver output the signal for each sweep is sampled, A/D converted, and recorded on digital tape. The number of sweeps recorded is determined by the desired Doppler resolution. For example, if one recorded 256 sweeps at a rate of 10 sweeps per s, a Doppler resolution of 0.04 Hz would result. Typically, a 100-kHz bandwidth might be swept 10 times per s for 25.6 s. If 128 received signal samples per sweep are recorded, then sufficient data would exist to generate 64 range cells with a 3 km resolution per cell and 256 Doppler cells with a resolution of 0.04 Hz per cell. These would be generated digitally by the application of the fast Fourier transform row by row and then column by column to the 128 × 256 matrix of data consisting of the 128 samples per sweep and the 256 sweeps. Actually, to save processing time only the desired

range cells would be generated. Thus, only a few of the columns resulting from the first row by row transform would be subsequently transformed.

In terms of hardware requirements, the stability and spectral purity required of the transmitter and receiver local oscillator for the FMCW case are the same as for a pulse-Doppler system. For the FMCW waveform, however, no peak power problems exist, and the IF bandwidth required in the receiver is comparable to that normally encountered in HF communications receivers. For example, with the waveform parameters quoted above, an IF bandwidth of only 1.28 kHz is required.

This reduction in the IF bandwidth requirements could be of particular importance for an aircraft experiment. In the case of an orbital sensor, the ionosphere will screen the receiver from much of the man-made interference, and the use of a 50 to 100 kHz IF bandwidth may be possible without the system being seriously affected by the interference. For an aircraft, however, the situation is quite different. It is very unlikely that 50 to 100 kHz of essentially clear bandwidth is available anywhere in the HF region, and 20 or more such channels would be required for the bistatic system. In addition, the use of a pulse-Doppler waveform, which requires that high-power short pulses be emitted for a period of the order of 1 to 2 minutes, would tend to cause considerable interference to other HF band users.

The FMCW waveform, because of its limited IF bandwidth requirements and because IF limiting can be used to ameliorate against strong interfering signals, would, in general, be much less susceptible to interference than the pulse-Doppler waveform. In addition, because the frequency is continually sweeping, much less interference to other HF band users would result from the FMCW waveform.

The FMCW technique, in general, appears to be very flexible in that extensive preprocessing data editing can be carried out, if desired. For example, various weightings can be applied to reduce frequency sidelobes, the effects of aircraft acceleration or a curved flight path can be compensated, etc. The FMCW technique appears feasible, and it has been used recently for several applications. For example, several HF backscatter oblique ionosondes have very successfully used this approach.

The FMCW approach does, however, require good time synchronization between the transmitter and receiver. For example, a 1 μs timing error in the sweep start time corresponds to a 0.3 km range error. For sea state measurements, however, range

errors of this order would not appear to be as serious as for some other applications. A block diagram of a transmitter and receiver using the FMCW waveform is given in Figure 30.

For an aircraft experiment a somewhat undesirable alternative to the use of the signal Doppler for determination of the surface spectrum directionality is the use of the average signal polarization and a proper experimental geometry. For example, for a flight path which is essentially a constant direction flight passing over, or near, the transmitting site, those surface regions which are intersected by a vertical plane through the flight path are the primary contributors to a horizontally polarized receiving antenna oriented along the flight path. A trailing wire would be representative of such an antenna. Thus, by using such a horizontally polarized antenna, combined with flights at a number of azimuths over the transmitter, the surface spectrum directionality can be estimated.

For a horizontally polarized receiving antenna, unless a directional transmitting antenna is used, there will be a 180° ambiguity in the directional information obtained. For example, the upwind-downwind spectral component versus the crosswind spectral component can be obtained; however, the upwind component cannot be separate from the downwind component. The use of a directional transmitting antenna is possible, as discussed previously, with a ship-based transmitter.

From the standpoint of the overall experimental hardware cost and complexity, it appears that the use of a noncoherent system with the signal polarization used to obtain a measure of the directionality of the surface spectrum would be suitable. If Doppler processing is not used, then the demands upon the transmitter and receiver local oscillator stability and spectral purity will be substantially less. In fact, it appears that a CW or long-pulse system could be used since the direct signal would appear to be 10 to 20 dB below the scattered signal if CW or long pulses are used in conjunction with a vertical whip transmitting antenna.

In this event, the experimental hardware would consist of a CW or long-pulse HF transmitter capable of being switched in frequency over the range from approximately 1 to 30 MHz in 15 to 30 steps. The switching times are not critical; however, something less than a second is desirable. The average power output required would be of the order of 1 watt. The transmitter frequency could either be crystal controlled or use high-quality tuned circuits since stability of the order of a part in 10^7 is all that would be required for noncoherent processing.

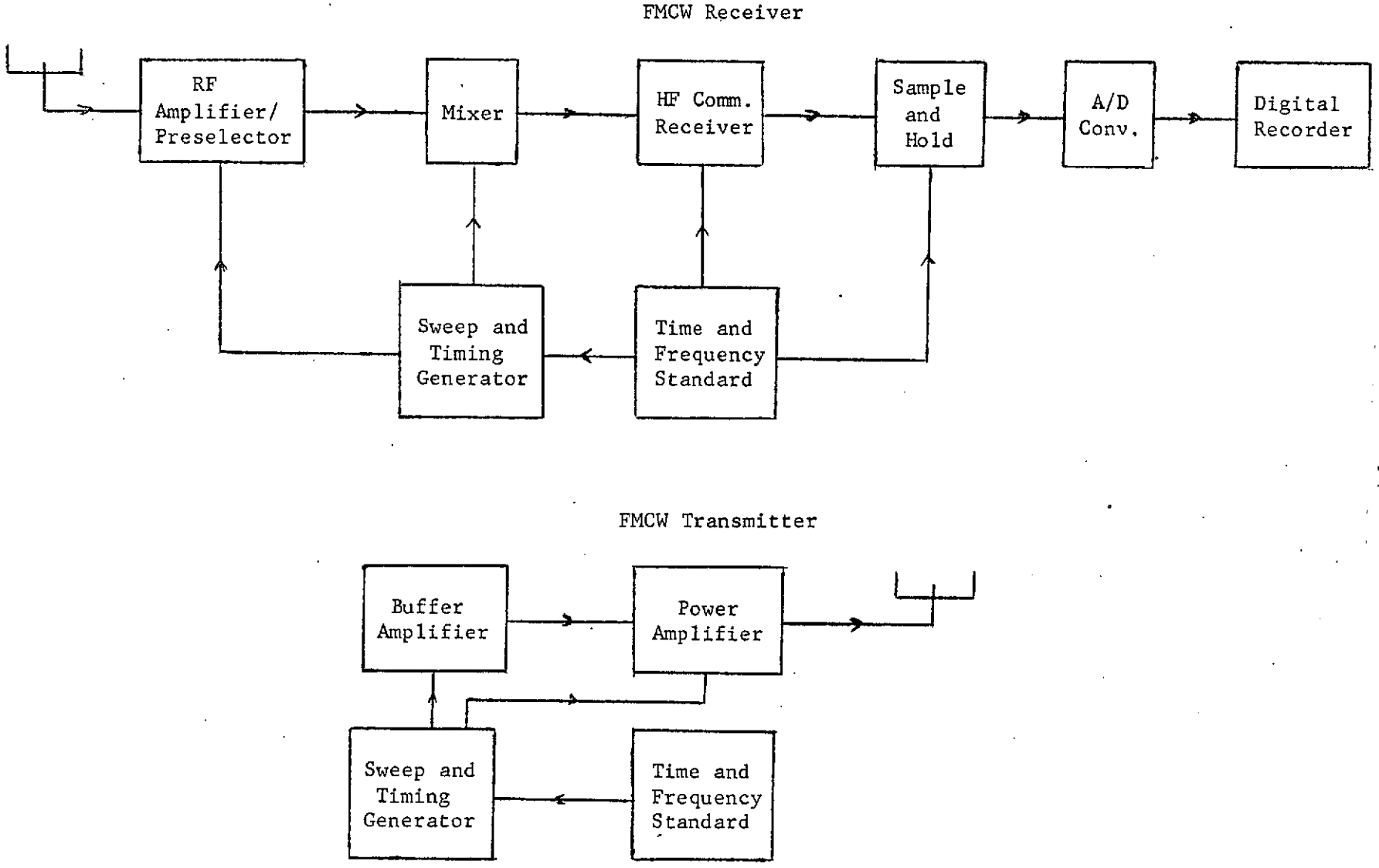

FIGURE 30. FMCW HARDWARE CONFIGURATION

REFERENCES

1. Kline, M., The Theory of Electromagnetic Waves, John Wiley & Sons, Inc., New York (1951), "Reflection of Electromagnetic Waves by Slightly Rough Surfaces" (S. O. Rice).

2. Barrick, D. E., and Peake, W. H., "A Review of Scattering From Surfaces with Different Roughness Scales", Radio Science, Vol 3, pp 865-868 (1968).

3. Roll, H. V., and Fischer, G., "Eine Kritische Bemerkung Zum Neumann-Spectrum de Seeganges", Deutschen Hydrogr. Zeitschrift, Vol 9, pp 9-14 (1956).

4. Phillips, O. M., Dynamics of the Upper Ocean, Cambridge University Press, London (1966), pp 109.

5. Longuet-Higgens, M. S., "Mass Transport in the Boundary Layer at a Free Oscillating Surface", Jour. Fluid Mechanics, Vol 8, No 2, pp 293-306 (1960).

6. Ruck, G. T., Barrick, D. E., Stuart, W. D., and Krichbaum, C. K., Radar Cross Section Handbook, Volume I, Plenum Press, New York (1970), pp 52-54.

7. Barrick, D. E., "Relationship Between Slope Probability Density Function and the Physical Optics Integral in Rough Surface Scattering", Proc. IEEE, Vol 56, No 10, pp 1728-1729 (October, 1968).

8. Davies, K., "Prediction of Ionospheric Characteristics at CRPL* for Sky-Wave Radio Propagation at High Frequencies", Telecommunication Journal, Vol 31, No 12, pp 1-12 (December, 1964).

9. Kazantsev, A. N., Romanova, T. S., and Kleusutenko, A. Ya., "The Determination of the Absorption of Radio Waves in the Ionosphere From Observations on Artificial Earth Satellites", Radiotekhnika i Elektronika, Vol 3, No 9, pp 1107-1121 (1958).

10. Hartz, T. R., "Radio Noise Within and Above the Ionosphere", Proc. IEEE, Vol 57, pp 1042-1050 (June, 1969).

11. Disney, R. T., Gichlow, W. O., "Radio Noise Sources and Characteristics", NBS Course in Radio Propagation, Lecture No. 29 (July, 1961).

12. CCIR Report 322, "World Distribution and Characteristics of Atmospheric Radio Noise", I.T.U., Geneva (1964).

13. Alpert, Ya. L., "The Study of the Ionosphere and Interplanetary Gas Employing Artificial Earth Satellites and Space Rockets", Planet. Space Sci., Vol 9, pp 391-443 (1962).

14. Kazautsev, A. N., "Absorption and Electron Distribution in the F2 Layer Determined from Measurements and Transmitted Radio Signals from Earth Satellites", Planet. Space Sci., Vol 1, pp 130-135 (1959).

15. Lawrence, R. S., Little, C. G., and Chiveis, H. T. A., "A Survey of Ionospheric Effects Upon Earth-Space Radio Propagation", Proc. IEEE, Vol 52, pp 4-27 (1964).

16. Hibberd, F. H., and Thomas, J. A., "The Determination of the Electron Distribution in the Upper Ionosphere from Satellite Doppler Observations", J. Atmosph. Terr. Phys., Vol 17, pp 71-81 (1959).

17. Ruck, G. T., Barrick, D. E., Stuart, W. D., and Krichbaum, C. K., Radar Cross Section Handbook, Volume II, Plenum Press, New York (1970), p 786.

18. Barrick, D. E., "Theory of Ground-Wave Propagation Across a Rough Sea at Dekameter Wavelengths", Research Report, Battelle Memorial Institute (January, 1970).

APPENDIX

DETERMINATION OF MEAN SURFACE POSITION AND SEA STATE FROM THE RADAR RETURN OF A SHORT-PULSE SATELLITE ALTIMETER

DETERMINATION OF MEAN SURFACE POSITION AND SEA STATE FROM THE RADAR RETURN OF A SHORT-PULSE SATELLITE ALTIMETER

by

Donald E. Barrick

INTRODUCTION

Sea surface roughness has always represented an unavoidable degradation to the performance of a satellite radar altimeter[1,2] . It would be desirable for geodetic purposes to measure the position of the mean sea surface to an accuracy of less than a foot. Sea states over the oceans result in waveheights commonly of the order of six or more feet. It is physically obvious that such waveheights will "stretch" the receiver output pulse in some way, producing an uncertainty in the position of the mean surface of the order of the sea waveheight. Since sea state at any given time and place on the ocean is usually unknown, and since the interaction mechanism of an altimeter pulse with the sea has not yet been fully analyzed, doubt has remained as to the efficacy of an altimeter to determine mean sea level to the precision geodetically desired.

It is the purpose of this discussion to show that sea state effects on altimeter performance need not limit its accuracy, primarily because the interaction between the radar pulse and the ocean waves is understood and predictable. Using a physically simple but rigorous theory, the pulse distortion from wind-driven sea waves will be analyzed. The validity of the results will be established by comparison with two independent sets of experimental data.

Based upon the analysis set forth herein, the mean sea level can be extracted from a satellite altimeter receiver signal. A simple one-step process will be suggested, whereby the incoherent, averaged signal versus time is differentiated, and the mean level is seen immediately as the position of the peak. The rms ocean waveheight and/or wind speed responsible for the ocean waves can then be inferred directly from the width of this signal derivative pulse.

PHYSICAL THEORY RESPONSIBLE FOR SCATTER

For the microwave frequencies at which an altimeter will operate, scatter from the sea within the near-vertical region directly beneath the satellite is quasi-specular in nature. This means that such scatter is produced primarily by specular or glitter points on the surface whose normals point toward the satellite. This is the same mechanism producing the dancing glitter of sunlight or moonlight on a water surface. Such scatter persists only as far as 15-20° from the vertical, since gravity waves can seldom maintain slopes greater than this amount before they break and dissipate energy. A physical picture of the specular points illuminated within a short-pulse radar cell advancing at an angle θ with respect to the mean surface is shown in Figure A-1.

This specular point scatter is readily predictable from geometrical and/or physical optics principles, and has been analyzed previously[3]. Here we extend the theory to include the height of the surface, since the short radar pulse will not illuminate the entire surface at a given time, but only those waves whose heights are sufficient to lie within the radar pulse. As the starting point, we note both from elementary geometrical optics principles or from more rigorous physical optics derivations[3,4], that the field scattered from N specular points (expressed in terms of the square root of the backscatter cross section) is

$$\sigma_B^{1/2} = \sum_{i=1}^{N} \pi^{1/2} \, g_i^{1/2} \, e^{i2k_o h_i \cos\theta} \quad , \tag{A-1}$$

where g_i is the Gaussian curvature at the i-th specular point, i.e., $g_i = |\rho_{1i}\rho_{2i}|$, with ρ_{1i} and ρ_{2i} as the principal radii of curvature at this point. Also, h_i is the height of the i-th specular point above the mean surface (taken as k = 0), θ is the angle of incidence from the vertical, and $k_o = 2\pi/\lambda$ is the free-space radar wavenumber, λ being the wavelength.

Squaring the above equation and averaging with respect to the phase, φ_{ij}, note that $\varphi_{ij} = 2k_o \cos\theta(h_i + h_j)$ will be uniformly distributed between zero and 2π as long as the sea waveheight is larger than the radar wavelength. Thus the average of the double summation over i and j is zero except where j = -i, reducing the result to a single summation:

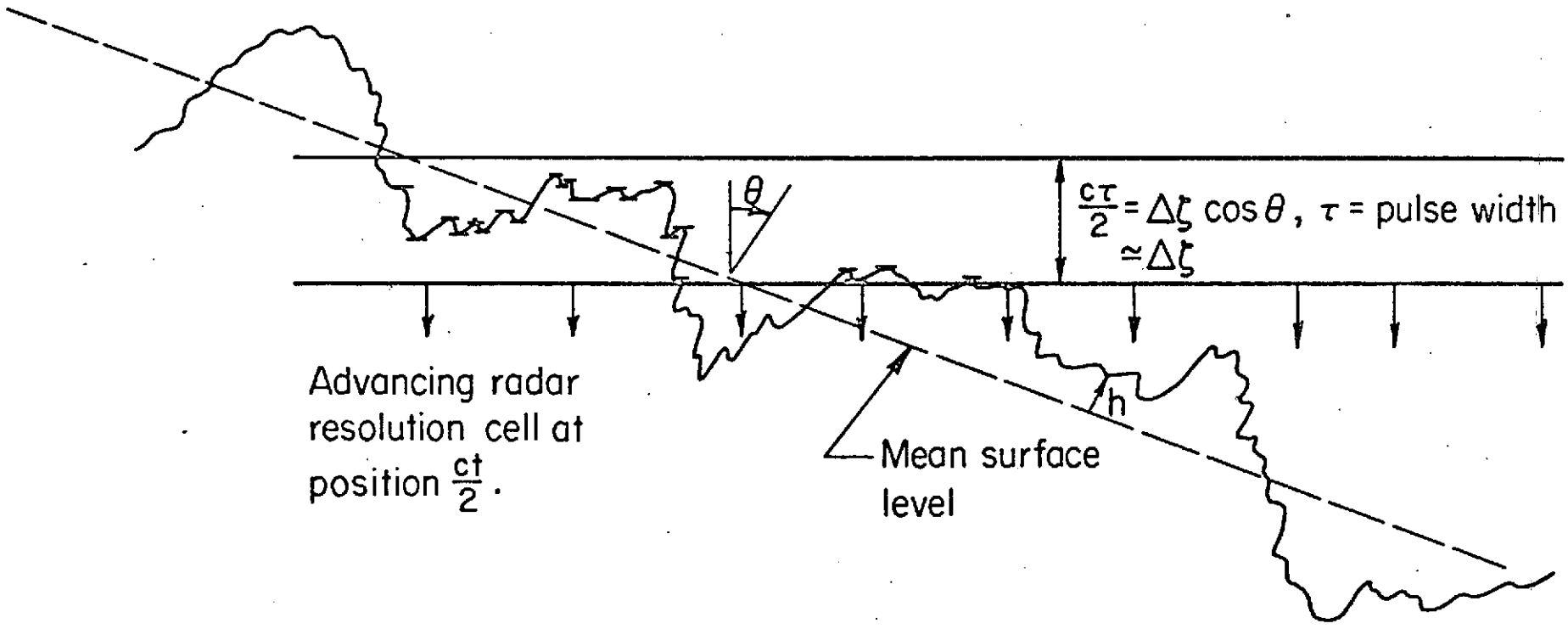

FIGURE A-1. PHYSICAL PICTURE OF SPECULAR POINT SCATTER. SPECULAR POINTS WITHIN RADAR RESOLUTION CELL ARE SHOWN HIGHLIGHTED.

$$\langle \sigma_B \rangle_{ph} = \pi \sum_{i=1}^{N} g_i \quad . \tag{A-2}$$

Now, we rewrite this equation in integral form as a distribution of specular points versus height above the surface, h, and Gaussian curvature, g, as

$$\langle \sigma_B \rangle_{ph} = \pi A \int_{-\infty}^{\infty} dh \int_{0}^{\infty} N(h,g) g \, dg \quad , \tag{A-3}$$

where AN(h,g) is the number of specular points within a surface patch of area A, within the height interval h to h + dh, and with Gaussian curvatures between g and g + dg.

The averaging process is completed by defining $n(h,g) \equiv \langle N(h,g) \rangle$ as the average specular point density, and we then denote $\eta^o(h)$ as the average radar cross section per unit area of the surface per unit height increment, Δh, at a given height h; thus

$$\eta^o(h) = \pi \int_{0}^{\infty} n(h,g) \, g \, dg \quad . \tag{A-4}$$

Here we employ the normalization $\sigma^o = \int_{-\infty}^{\infty} \eta^o(h) dh$, where σ^o is the standard average backscatter cross section per unit area. Thus, a short pulse producing a vertical radar resolution cell of width Δh at height h will produce, on the average, a radar cross section per unit area of $\eta^o(h)\Delta h$.

The specular point density, n, can readily be determined (almost by inspection) from the work of Barrick[3] preceding Eq. (A-7) of that paper; one must merely include height in the probability densities. Thus the density of specular points within area A is

$$n(h,g) \, dg = p(h, \zeta_{xsp}, \zeta_{ysp}, \zeta_{xx}, \zeta_{yy}, \zeta_{xy}) \left| \zeta_{xx}\zeta_{yy} - \zeta_{xy}^2 \right| d\zeta_{xx} d\zeta_{yy} d\zeta_{xy} \quad , \tag{A-10}$$

where p is the joint probability density function of the surface height h, the surface slopes ζ_x, ζ_y, and the second partial derivatives of the surface at a given surface point. Since it is known a priori that scatter is originating at surface regions

with their normals pointing toward the satellite, the slopes which must be used are geometrically known; we denote them ζ_{xsp} and ζ_{ysp}.

Likewise, the Gaussian curvature at a specular point is found from differential geometry to be

$$g = \frac{(1 + \zeta_{xsp}^2 + \zeta_{ysp}^2)^2}{|\zeta_{xx}\zeta_{yy} - \zeta_{xy}^2|} \quad . \tag{A-11}$$

Hence we arrive at the result

$$\eta^o(h) = \pi \int_{-\infty}^{\infty}\int\int |\zeta_{xx}\zeta_{yy} - \zeta_{xy}^2| p(h,\zeta_{xsp},\zeta_{ysp},\zeta_{xx},\zeta_{xy},\zeta_{yy}) \times$$

$$\frac{(1 + \zeta_{xsp}^2 + \zeta_{ysp}^2)^2}{|\zeta_{xx}\zeta_{yy} - \zeta_{xy}^2|} d\zeta_{xx} d\zeta_{yy} d\zeta_{xy}$$

$$= \pi(1 + \zeta_{xsp}^2 + \zeta_{ysp}^2)^2 \, p(h,\zeta_{xsp},\zeta_{ysp}) \tag{A-12}$$

For backscatter, the squared factor in parentheses is merely equal to $\sec^4 \theta$, where θ is the incidence angle from the vertical. Also, it is simple to show that, while the surface height h and second derivatives are correlated, the height and slopes are uncorrelated. Hence, if the surface is Gaussian (or nearly so, which is true for the sea), the height and slopes are statistically independent and we have

$$\eta^o(h) = \pi \sec^4 \theta \, p(h) p(\zeta_{xsp},\zeta_{ysp}) \quad , \tag{A-13}$$

where $p(h)$ is the height probability density and $p(\zeta_x,\zeta_y)$ is the joint slope probability density. The above result can now be applied to predict the average radar cross section observed at a short-pulse altimeter as a function of time.

APPLICATION TO SHORT-PULSE SATELLITE ALTIMETER

1. General Development

Eq. (A-13) can now be applied to the problem depicted in Fig. A-2: a satellite at altitude H emitting a spherical pulse which in turn sweeps past a spherical earth. The spatial pulse width for a backscatter radar is $c\tau/2$, where c is the velocity of light and τ is the time width of the pulse (compressed, if applicable) at the receiver output. Likewise, the distance of the spherically emanating pulse from the satellite, measured in time at the receiver from transmission of the signal, is $ct/2$. However, for convenience, we henceforth choose $t = 0$ as the time that the center of the spherical pulse shell strikes the uppermost cap of the spherical earth. In other words, in the absence of any roughness, the received pulse from the suborbital point will be a replica of the processed transmitter pulse, and we choose its center time position as a reference in order to study the effect of sea state on pulse distortion.

First of all, we note from Fig. A-2 that the angle of incidence, θ, at any point on the surface is given by $\theta \approx \psi + \varphi \simeq \psi(1 + H/a)$ for θ small. The incidence angle at the intersection of the mean earth spherical surface and the center of the pulse cell, expressed in terms of receiver time is then $\theta \simeq \sqrt{(ct/H)(1 + H/a)}$. For a short pulse, θ can be considered a constant within the pulse cell width. The height, h, to a point at the center of the cell above the mean sea surface can then be given as

$$h = \frac{H(1 - \cos\psi) + a(1 - \cos\varphi) - (ct/2)\cos\psi}{\cos\varphi} \qquad (A\text{-}14)$$

and for ψ small, this reduces to

$$h \simeq \frac{H}{2}\psi^2\left(1 + \frac{H}{a}\right) - \frac{ct}{2} \quad . \qquad (A\text{-}15)$$

At this point, we must make some assumptions about the surface statistics and radar properties in order to perform the integration. For the sake of studying the general nature of the radar return, we make the following assumptions: (i) the signal shape is flat, of width τ, and zero everywhere else, (ii) the antenna beam pattern is uniform out to ψ_B off the axis, and zero everywhere else; ψ_B is thus the

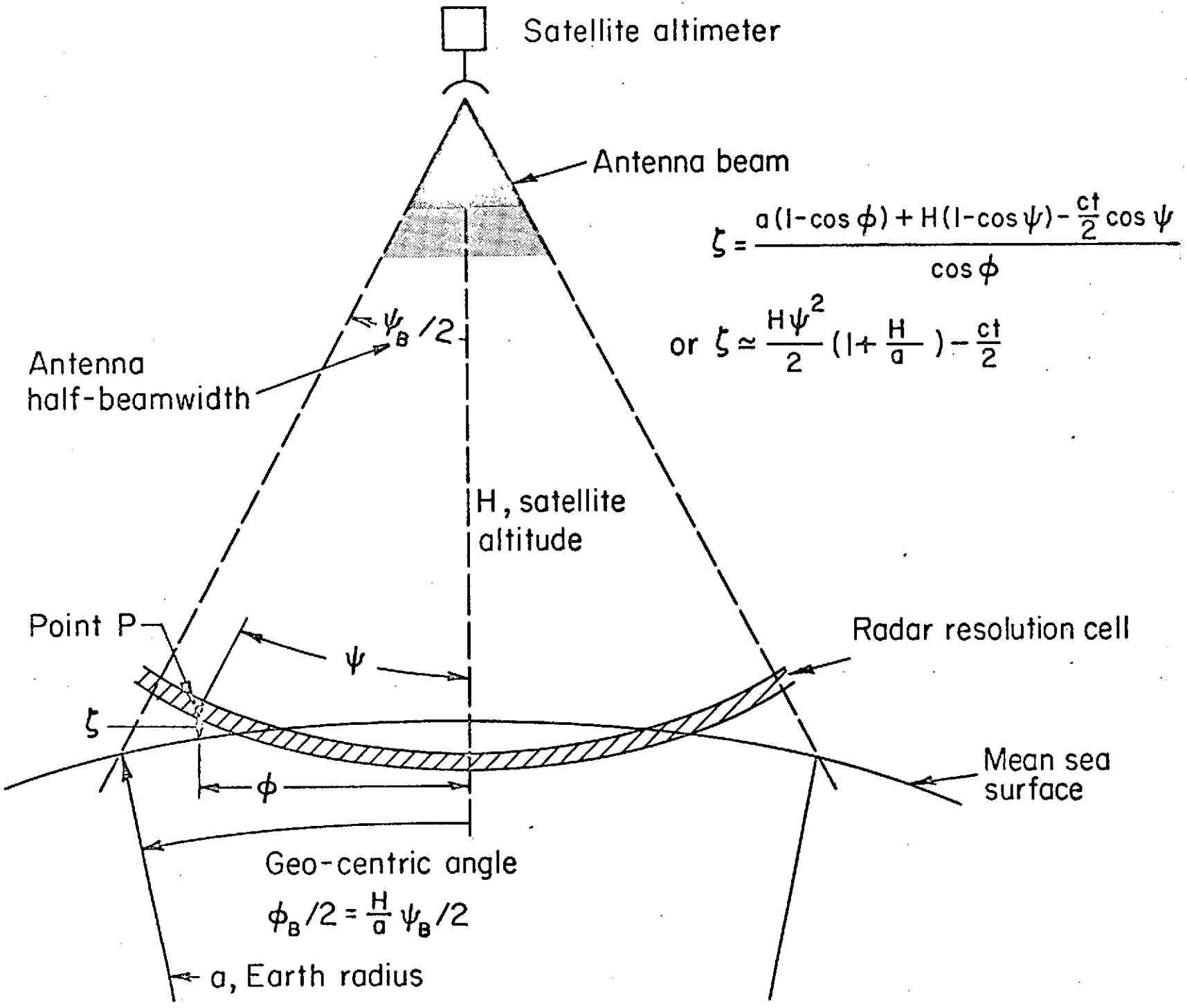

FIGURE A-2. GEOMETRY OF SATELLITE ALTIMETER

half-power half-beamwidth of the antenna*. We assume also that the sea surface height and slope probability distributions are Gaussian, realizing of course that the height distribution to second order is not quite Gaussian, but slightly skewed from the symmetric Gaussian shape, and has less probability in the tails. Furthermore, we assume that the sea is nearly isotropic, making the slopes ζ_x and ζ_y independent of wind direction. This is quite valid for very small incidence angles (and hence specular slopes).

Thus we have

$$p(\zeta_{xsp},\zeta_{ysp}) = p(\tan\theta) = \frac{1}{\pi s^2} e^{-\frac{\tan^2\theta}{s^2}} , \qquad \text{(A-16)}$$

and

$$p(h) = \frac{1}{\sqrt{2\pi}\,\sigma_h} e^{-\frac{h^2}{2\sigma_h^2}} , \qquad \text{(A-17)}$$

where $s^2 = \langle\zeta_x^2\rangle + \langle\zeta_y^2\rangle$ and $\sigma_h^2 = \langle h^2\rangle$.

Later, when relating these quantities to wind-developed waves, we shall use the relationships

$$s^2 = 5.5 \times 10^{-3}\, v \quad \text{and} \quad \sigma_h^2 = 2.55 \times 10^{-4}\, v^4 , \qquad \text{(A-18)}$$

where v is wind velocity in meters per second. The first of these relationships is inferred empirically from slope data versus wind speed presented in Phillips[5], and the second is obtained from integrating the Phillips wind-wave height spectrum.

Thus, the observed average radar cross section as a function of time will be

$$\sigma(t) = 2\pi^2 a^2 \int_0^{\frac{H}{a}\psi_B} p(\tan\theta)\sec^4\theta \sin\varphi \left\{ \int_{h-\frac{\Delta h}{2}}^{h+\frac{\Delta h}{2}} p(h)dh \right\} d\varphi , \qquad \text{(A-19)}$$

*Other, possibly more realistic, pulse and beam shapes can be readily inserted into the integral if desired.

where θ and h were related to φ previously.

For a pulse width sufficiently short that $\Delta h \approx (c\tau/2) < 2\sigma_h$, we can approximate the second integral and obtain a closed-form answer for the remaining integral. Physically, this requires that the spatial pulse width be less than the rms ocean waveheight (peak-to-trough). This is realized on the open ocean with compressed pulse widths less than about 10 ns for waves excited by winds greater than about 10 knots. For simplicity we shall make this assumption here, analyzing the more general case at a later date. The result is then

$$\sigma(t) = \frac{\pi c \tau}{2s^2[(1/a) + (1/H)]} \left\{ \operatorname{erf}\left(\frac{ct}{\sqrt{8}\,\sigma_h}\right) + \operatorname{erf}\left(\frac{H'\psi_B^2 - ct}{\sqrt{8}\,\sigma_h}\right) \right\} \quad , \qquad \text{(A-20)}$$

where $H' = H[1 + (H/a)]$. The quantities in the braces are the error functions; the first one is responsible for the rising leading edge of the radar return, while the second produces the fall-off of the trailing edge.

2. Pulse-Limited Altimeter ($\psi_B \gg \sqrt{c\tau/H'}$)

When the radar is sufficiently high, the beamwidth sufficiently wide, and the pulse length sufficiently short, the response of the altimeter is said to be pulse-limited. This means in effect that the earth area illuminated most of the time lies in a "range ring" of constant surface area, as shown in Fig. (A-3a). Such a situation will always exist for a short-pulse satellite altimeter, will nearly always exist for aircraft altimeters, but may not exist for tower-based altimeters looking at the sea (an example of the latter will be discussed subsequently). The general form of Eq. (A-20) is valid for either pulse- or beam-limited operation, under the simplifying assumptions made previously (flat pulse and antenna pattern, short-pulse operation).

In this mode of operation, the mean surface at the suborbital point lies somewhere in the leading, rising edge of the echo. The essence of the problem, however, is that the rise time of the leading edge is not only inversely proportional to the transmitted signal bandwidth (or shape)--a factor which could easily be removed for high signal-to-noise ratios because the signal shape is known a priori--but the rise time varies also with sea state because of temporal dispersion caused by the spatial distribution of specular points.

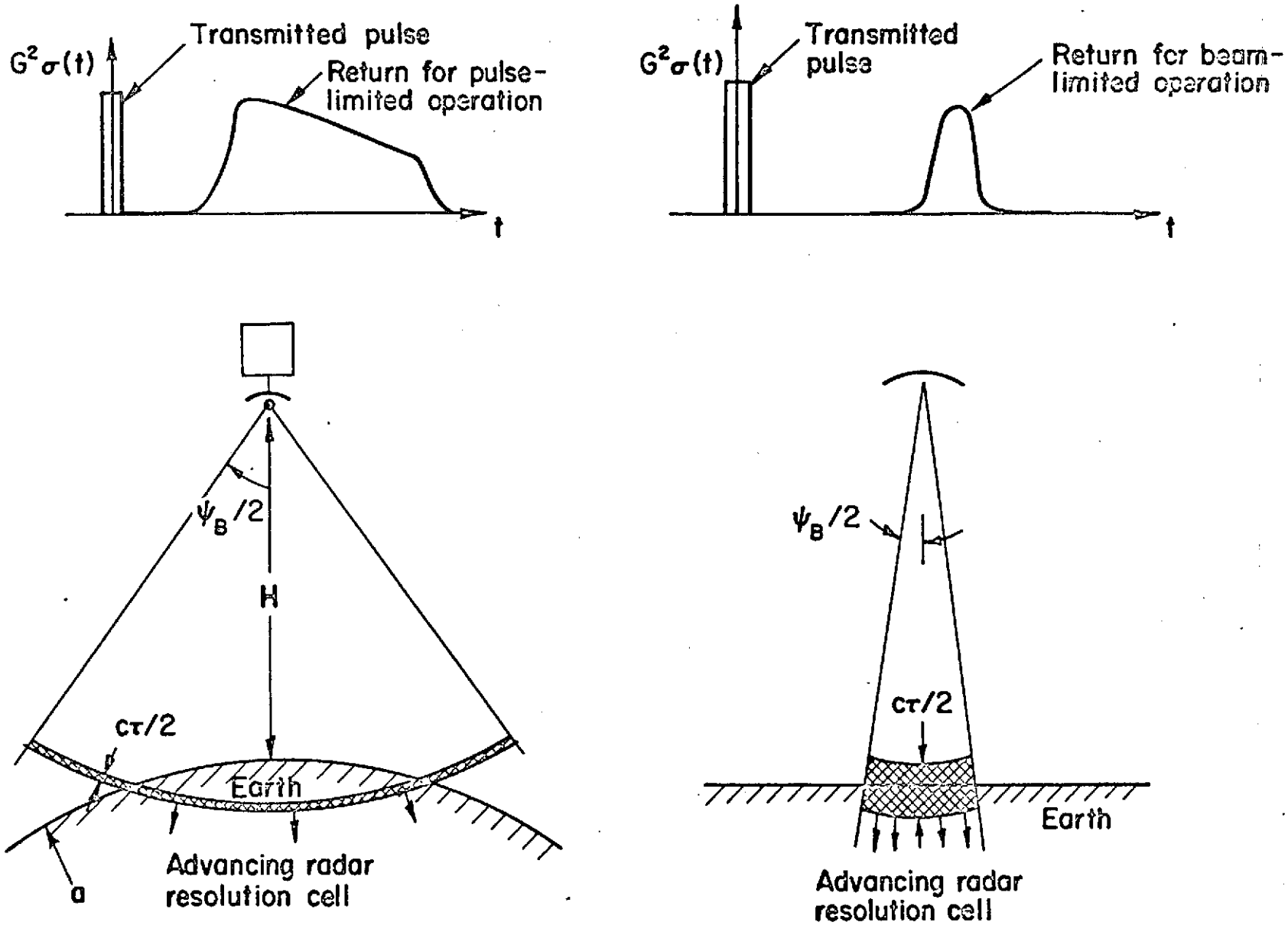

FIGURE A-3. TWO MODES OF ALTIMETER OPERATION AND THE RESULTING SIGNALS

To study the theoretical shape of the leading edge of the return for the pulse-limited case, we examine Eq. (A-20). First of all, we note that the return rises rapidly to a maximum, has a flat shape in the middle of duration $t_D = (H'/c)\ \psi_B^2$, and falls off to zero as rapidly as it rose. The shape of the pulse is symmetric about $t_D/2$. In practice, such a flat, symmetric return will not be observed, primarily because the antenna pattern falls off with increasing ψ, rather than remaining constant out to ψ_B and then dropping suddenly to zero, as we assumed here. The shape shown in Fig. A-3a is more typical of the overall echo shape. The shape of this latter portion of the signal need not concern us here, however, because it contains no information about the mean surface position and little information about sea state. The maximum value of $\sigma(t)$ is of concern, however; it is readily found from Eq. (A-20) by noting that the maximum value of the quantity in braces is 2. Hence, $\sigma_{MAX} = \pi\, c\tau/[s^2(1/a + 1/H)]$.

To study the leading edge versus sea state, we use parameters typical of a Skylab satellite altimeter: $H = 435$ km, $\psi_B = 1.5°$, and $\tau < 15$ nsec. In addition, we use Eq. (A-18) to relate the statistics of the wind-excited surface to wind speed. The result is the family of normalized curves shown in Fig. A-4, showing the leading edge of the return. The mean surface, of course, is located at $t = 0$, which appears at precisely one-half the maximum value. The effect of sea state is as expected; higher wind speeds and hence greater rms roughness heights tend to stretch (i.e., disperse) the leading edge, giving a greater rise time.

3. Beam-Limited Altimeter ($\psi_B \ll \sqrt{c\tau/H'}$)

In less frequent altimeter applications, the configuration may be beam-limited, as shown in Fig. A-3b. In this case, the interaction at the surface directly beneath the altimeter appears planar, i.e., the effects of the spherical earth and spherical pulse front are negligible. This could occur for a low-flying, narrow-beam aircraft altimeter, but would not exist for a satellite altimeter. When this extreme is achieved, the return can best be analyzed by expanding the second term in Eq. (A-20) in a Taylor series, expanded about argument $ct/\sqrt{8}\ \sigma_h$). This gives

$$\sigma(t) \simeq \frac{c\tau H^2 \psi_B^2}{2\sqrt{2\pi}\, s^2 \sigma_h} \left[e^{-\left(\frac{ct}{\sqrt{8}\ \sigma_h}\right)^2} + \cdots \right], \qquad \text{(A-21)}$$

where the higher-order terms omitted here are of the order of $H'\psi_B^2/\sqrt{8}\ \sigma_h$, which is assumed to be small since we have taken $c\tau/2 < 2\sigma_h$.

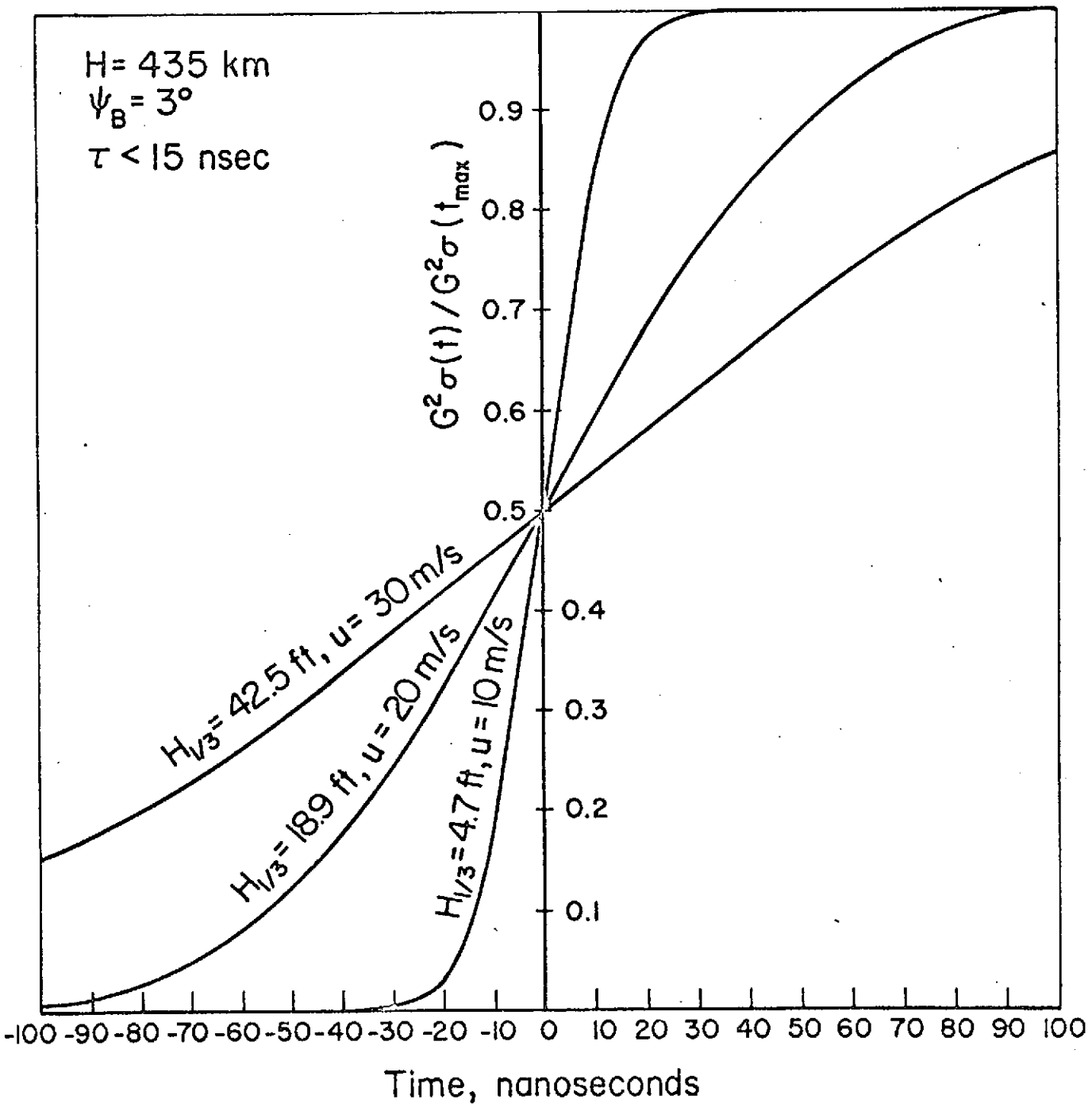

FIGURE A-4. LEADING EDGE OF AVERAGED ALTIMETER OUTPUT VERSUS TIME FOR PULSE-LIMITED OPERATION

The maximum and the Gaussian nature of this return are easily seen from the above equation. The width of the pulse is directly related to the rms surface height, and the mean position of the surface occurs precisely at the pulse peak.

DEDUCTION OF MEAN SURFACE POSITION AND SEA STATE FROM ALTIMETER RETURN

If we can employ a beam-limited short-pulse altimeter, we will have no trouble deducing either the mean surface position or the rms surface height of the ocean. The former is found from the pulse peak position and the latter from its width, as readily observed from Eq. (A-21). Unfortunately, the parameter requirements for this limiting configuration are such as to preclude its implementation on a satellite.

Restricted, then, to pulse-limited altimeter operation from a satellite, the question remains as to how to find the mean surface position in the leading edge of the extended echo. From Eq. (A-20) and the curves plotted in Fig. A-4, the answer is obvious--in the absence of noise. Merely find the half-power point on the rising edge; this time corresponds to the distance to the mean surface. However, in the presence of additive, independent noise, and with the often-jagged appearance of the echo near its maximum (see measured returns in Fig. A-6), finding this half-way point becomes more difficult.

A signal processing technique to be suggested here makes use of the fact that this half-power point defining the mean surface position is also the point of maximum slope. Hence, we suggest that the processor form the time derivative of the altimeter output power--after incoherent averaging (or summing) and band-pass filtering of several pulse returns. Thus, the incoherent averaging and filtering will remove much of the jagged noise, while providing a smooth, clearly recognizable leading edge. The derivative of this signal is easy to form from Eq. (A-20). It is

$$\sigma'(t) = \sqrt{\frac{\pi}{2}}\,\frac{c\tau}{2s^2}\cdot\frac{c}{\sigma_h\left(\frac{1}{a}+\frac{1}{H}\right)}\,e^{-\left(\frac{ct}{\sqrt{8}\,\sigma_h}\right)^2}. \qquad \text{(A-22)}$$

Figure A-5 shows a family of normalized curves of this average altimeter leading-edge output differentiated versus time. The pulse center is the mean surface position, and its width is clearly proportional to rms surface height (or the square

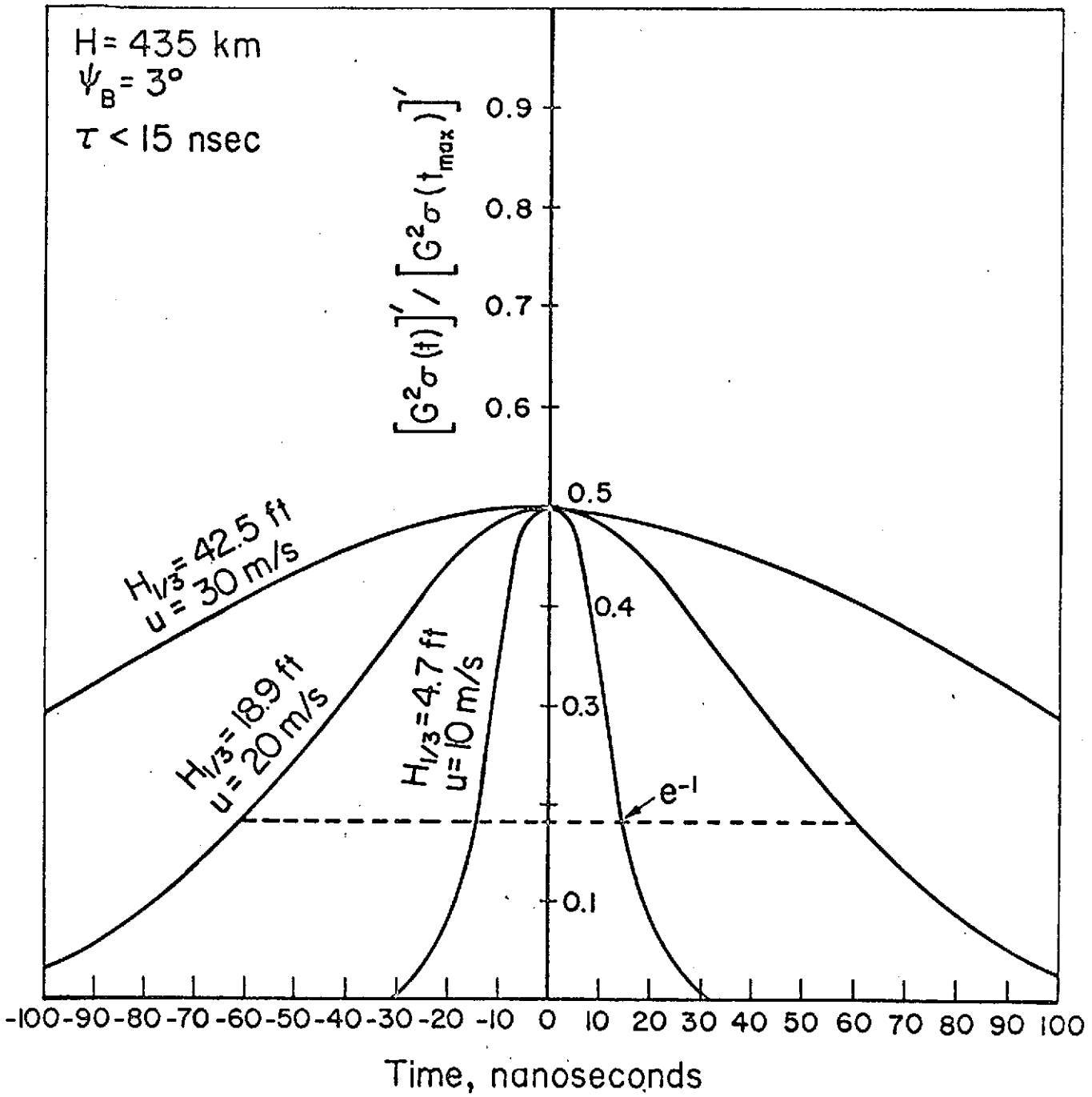

FIGURE A-5. DERIVATIVE OF LEADING EDGE OF AVERAGED ALTIMETER OUTPUT VERSUS TIME FOR PULSE-LIMITED OPERATION

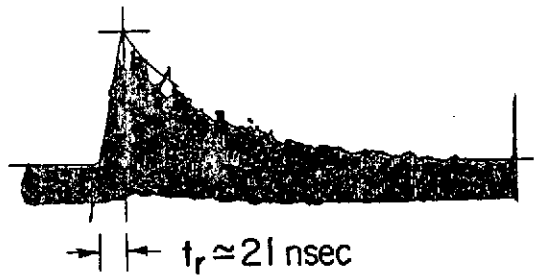

Flight #14
Run #12
H = 10 kft
τ = 20 nsec
$t_r \simeq 21$ nsec
Measured wind = 12 knots
Calculated wind = 14.1 knots

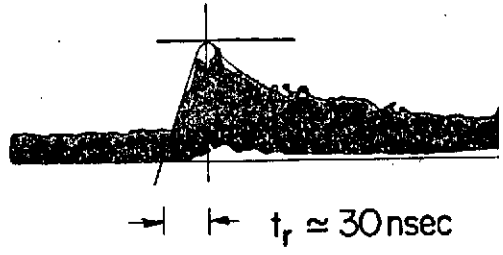

Flight #16
Run #9
H = 10 kft
τ = 20 nsec
$t_r \simeq 30$ nsec
Measured wind = 22 knots
Calculated wind = 21.2 knots

FIGURE A-6. MEASURED [RAYTHEON COMPANY, WAYLAND LABORATORIES, 1970] AIRCRAFT ALTIMETER RESPONSES. WIND SPEEDS INFERRED FROM RISE TIME AND PULSE-LIMITED MODEL ARE COMPARED TO OBSERVED WIND SPEEDS.

of wind velocity, for wind-driven waves). There is no need for absolute measures of signal level, either for mean surface position or for sea state determination; hence, atmospheric attenuation and system power drifts are not critical.

A large amount of noise can, of course, degrade the pulse positioning accuracy of this system, as in any system. However, so long as σ_{MAX} is several decibels above the noise level, the position of the pulse center in the signal derivative should be relatively insensitive to noise. The degradation of altimeter accuracy with sea state and noise level has the desirable attributes of pulse-position modulation (PPM) systems of digital communication theory, but should be the subject of further study.

COMPARISON OF THEORETICAL MODEL WITH GROUND-TRUTH DATA

For verification of the theory and the various assumptions that have gone into it, we choose measured data from two separate altimeter experiments: one pulse-limited and the other beam-limited. The pulse-limited data chosen was measured and reported by Raytheon[6] for aircraft flights at 10,000 ft with a pulse width of 20 ns. The half-beamwidth, ψ_B, is 2.5°, and the surface winds reported during Flights 14 and 16 were 12 and 22 knots, respectively. Their averaged altimeter outputs are shown in Fig. A-6. Since there is no precise way of comparing measured surface position with that calculated, we intend to compare the actual sea state effects, as contained in the leading-edge rise time, t_r, with those calculated. We roughly measure rise times of 21 and 30 ns for the two records displayed, and use Eqs. (A-18) and (A-20) to calculate the wind speeds required to cause seas producing this rise time. The calculated winds are 14.1 and 21.2 knots, comparing reasonably well with the measured winds. Good comparison on Flight 14 was not expected, because the condition $c\tau/2 > 2\sigma_h$ is barely satisfied for this mild sea condition. When this inequality is not satisfied, Eq. (A-20) is not applicable, and one must instead go back to Eq. (A-19). Practically, this means that with a 20 ns pulse, one cannot hope to meaningfully measure sea states which will produce a rise-time stretching of less than 20 ns.

As an example of the comparison of Eq. (A-21) for beam-limited operation with measurements, we selected data recently reported by Yaplee et al[7]. His measurements were taken from a tower at H = 70 ft above the water and $\psi_B \simeq 1°$. His pulse width τ = 1 ns was long enough to assure beam-limited operation, but short enough to allow

the condition $c\tau/2 < 2\sigma_h$ to be satisfied for the two sets of data reported. We compare the shapes of the curve given by our Eq. (21) with what he has called the impulse response* shown in his Figs. 11 and 12. He plots the responses measured both by radar and by a wavestaff, for two different days on which the significant waveheights (measured by the wavestaff) were 3.1 and 5.2 ft. Since his response heights were relative, we compare the shape of his curves in Fig. A-7 with that of our Eq. A-21, using rms waveheight, σ_h, corresponding to 3.1 and 5.2 ft. The agreement in width is quite good. The comparison also points out where the Gaussian assumption for the sea height is weak: in the echo tails and in the symmetry about the center. The Gaussian surface has some (small) probability of very large heights, and is always symmetric, whereas the height of real ocean waves can never be infinite, and the surface is not exactly symmetric for positive and negative heights. These differences, while interesting, should not detract from the fact that the simple Gaussian model can be applied adequately well to predict mean surface position and rms waveheight.

CONCLUSIONS

The principal conclusions to be made from this analysis are that a short pulse altimeter can be used--even in the presence of high seas--to measure accurately the mean surface level and also to deduce the sea state. The simple interaction of the microwave altimeter pulse with the sea at near-vertical incidence is separable from the more complex interaction mechanism at larger incidence angles; It follows the straightforward specular point theory derivable from either geometrical or physical optics.

In satellite applications, the altimeter return will be pulse-limited in its nature. For reasonably meaningful measurements of the geoid, the pulse width must be kept small, i.e., less than 20 ns. It is precisely for these short pulses that ocean waveheights can temporally disperse the signal leading edge. We have shown by the specular point theory, however, that this interaction is known and its results are predictable. We have suggested and discussed a signal processing scheme employing the signal derivative, which can locate the mean surface position from the pulse position and the rms surface height from the pulse width.

*The impulse response essentially has the effect "deconvolving" the pulse shape and size from the return to give a result with the same meaning as our Eq. (A-21).

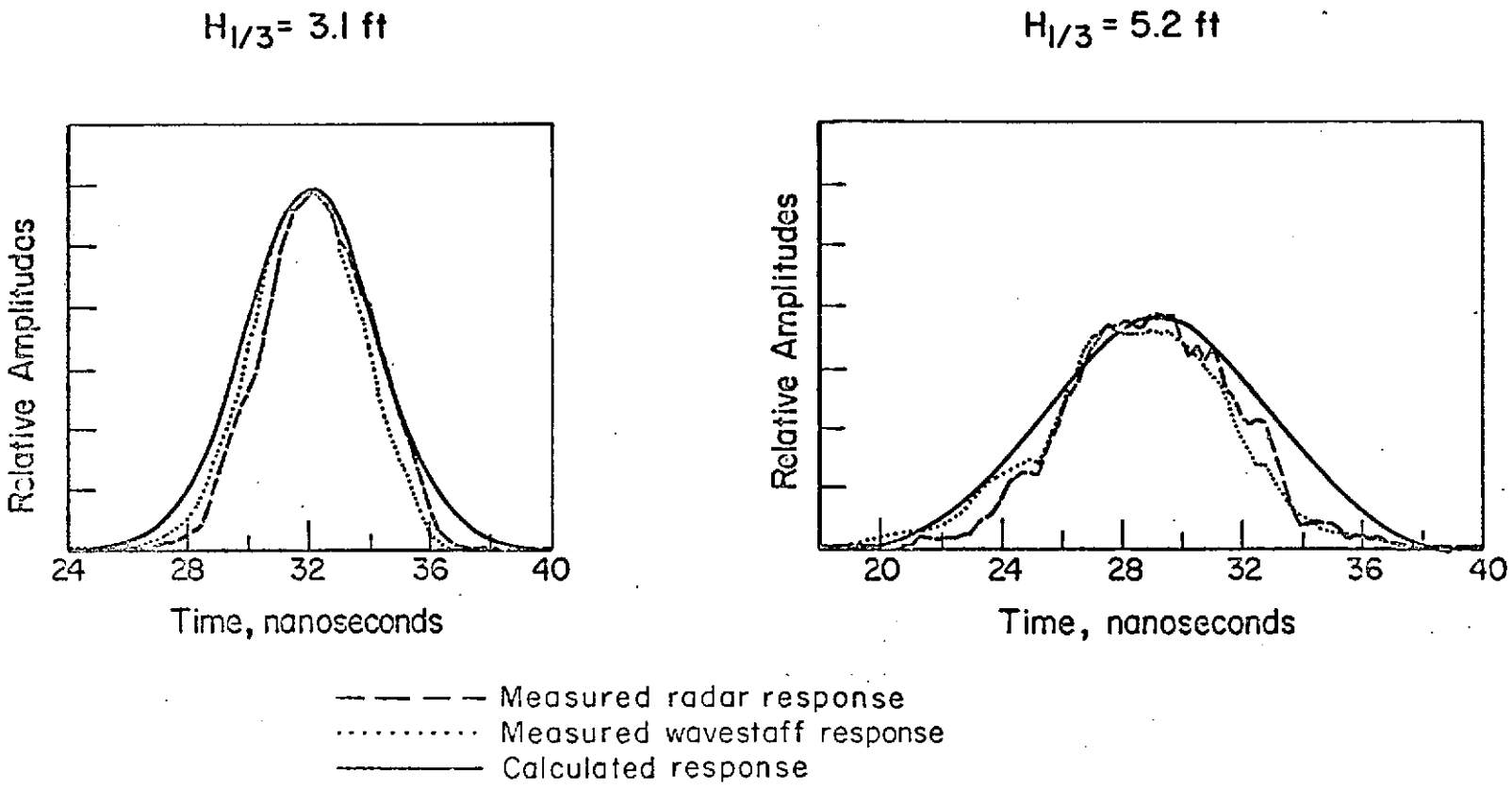

FIGURE A-7. MEASURED [AFTER YAPLEE et al., 1971] ALTIMETER (IMPULSE) RESPONSES VERSUS CALCULATED USING BEAM-LIMITED MODEL

Comparison of the theory with measurements and ground-truth data for two different altimeter modes (pulse- and beam-limited operation) lend credence to the theory. System noise can and will limit altimeter accuracy, but this can be reckoned with in a systematic manner using principles of PPM communication theory. Other practical effects such as nonrectangular pulse shapes can be accounted for in any further system analysis by including an additional pulse-shape factor in the integrand of Equation (A-19).

In short, the pulse-sea interaction is at present sufficiently well understood and verified that a short-pulse altimeter could be built which will provide: (1) accurate determination of mean sea level to a precision much greater than ocean waveheights, and (2) as a by-product, can provide rms ocean wave height (or wind speed) as well.

REFERENCES

1. J. A. Greenwood, A. Nathan, G. Neumann, W. J. Pierson, F. C. Jackson, and T. E. Pease, "Radar altimetry from a spacecraft and its potential applications to geodesy", Remote Sensing of the Environment, vol. 1. New York: American Elsevier Publishing Co., Inc., 1969, pp. 59-80.

2. T. W. Godbey, "Oceanographic satellite radar altimeter and wind sea sensor", from Oceanography in Space, Proc. of Conference, Woods Hole Oceanographic Institution, Ref. No. 65-10, G. C. Ewing, Ed., Aug. 24, 1964, pp. 21-26.

3. D. E. Barrick, "Rough surface scattering based on the specular point theory", IEEE Trans. Antennas Propagat., vol. AP-16, 1968, pp. 449-454.

4. R. D. Kodis, "A note on the theory of scattering from an irregular surface", IEEE Trans. Antennas Propagat., vol. AP-14, 1966, pp 77-82.

5. O. M. Phillips, Dynamics of the Upper Ocean. London: Cambridge at the University Press, 1966, pp. 109-139.

6. ———, "Space geodesy aircraft experiment", Raytheon Co., Wayland Laboratories, Sudbury, Massachusetts, Final Rept., Contract No. NASW 1932, May 1970.

7. B. S. Yaplee, A. Shapiro, D. L. Hammond, B. D. Au, and E. A. Uliana, "Nanosecond radar observations of the ocean surface from a stable platform", IEEE Trans. Geoscience Electronics, vol. GE-9, 1971, pp. 170-174.